Ultrafast photoinduced phase transitions in complex materials probed by time-resolved resonant soft x-ray diffraction

Dissertation zur Erlangung des akademischen Grades

Dr. rer. nat.
in der Wissenschaftsdisziplin 'Experimentalphysik'

eingereicht an der
Mathematisch-Naturwissenschaftlichen Fakultät
der Universität Potsdam
von
Dipl.-Phys. Christoph Trabant

Potsdam, den 04.02.2014

Tag der Disputation: 02. July 2014
1. Gutachter: Prof. Dr. A. Föhlisch
2. Gutachter: Prof. Dr. M. Bargheer
3. Gutachter: Prof. Dr. P. v. Loosdrecht

Contents

Chapter 1.

Abstract

In processing and data storage mainly ferromagnetic (FM) materials are being used. Approaching physical limits, new concepts have to be found for faster, smaller switches, for higher data densities and more energy efficiency. Some of the discussed new concepts involve the material classes of correlated oxides and materials with antiferromagnetic coupling. Their applicability depends critically on their switching behavior, i.e., how fast and how energy efficient material properties can be manipulated. This thesis presents investigations of ultrafast non-equilibrium phase transitions on such new materials.

In transition metal oxides (TMOs) the coupling of different degrees of freedom and resulting low energy excitation spectrum often result in spectacular changes of macroscopic properties (colossal magneto resistance, superconductivity, metal-to-insulator transitions) often accompanied by nanoscale order of spins, charges, orbital occupation and by lattice distortions, which make these material attractive. Magnetite served as a prototype for functional TMOs showing a metal-to-insulator-transition (MIT) at $T = 123$ K. By probing the charge and orbital order as well as the structure after an optical excitation we found that the electronic order and the structural distortion, characteristics of the insulating phase in thermal equilibrium, are destroyed within the experimental resolution of 300 fs. The MIT itself occurs on a 1.5 ps timescale. It shows that MITs in functional materials are several thousand times faster than switching processes in semiconductors.

Recently ferrimagnetic and antiferromagnetic (AFM) materials have become interesting. It was shown in ferrimagnetic GdFeCo, that the transfer of angular momentum between two opposed FM subsystems with different time constants leads to a switching of the magnetization after laser pulse excitation. In addition it was theoretically predicted that demagnetization dynamics in AFM should occur faster than in FM materials as no net angular momentum has to be transferred out of the spin system. We investigated two different AFM materials in order to learn more about their ultrafast dynamics. In Ho, a metallic AFM below $T \approx 130$ K, we found that the AFM Ho can not only be faster but also ten times more energy efficiently destroyed as order in FM comparable metals. In EuTe, an AFM semiconductor below $T \approx 10$ K, we compared the loss of magnetization and laser-induced structural distortion in one and the same experiment. Our experiment shows that they are effectively disentangled. An exception is an ultrafast release of lattice dynamics, which we assign to the release of magnetostriction.

The results presented here were obtained with time-resolved resonant soft x-ray diffraction at the Femtoslicing source of the Helmholtz-Zentrum Berlin and at the free-electron laser in Stanford (LCLS). In addition the development and setup of a new UHV-diffractometer for these experiments will be reported.

Kapitel 2.

Kurzfassung

In der Datenspeichertechnologie werden bisher hauptsächlich ferromagnetische Materialien eingesetzt. Da mit diesen aber physikalische Grenzen erreicht werden, werden neue Konzepte gesucht, um schnellere und kleinere Schalter, größere Datendichten und eine höherere Energieeffizienz zu erzeugen. Unter den diskutierten Materialklassen finden sich komplexen Übergangsmetalloxide und Materialien mit antiferromagnetischer Kopplung. Die Anwendbarkeit solcher Materialien hängt stark davon ab, wie schnell sich deren Eigenschaften verändern lassen und wieviel Energie dafür eingesetzt werden muss. Die vorliegende Arbeit beschäftigt sich mit ultraschnellen, Nicht-Gleichgewicht-Phasenübergängen genau in solchen Materialien.

In Übergangsmetalloxiden führt die enge Kopplung zwischen den unterschiedlichen Freiheitsgraden zu einem effektiven niederenergetischen Anregungsspektrum. Diese Anregungen sind oft verknüpft mit spektakulären makroskopischen Eigenschaften, wie z.B. dem kolossalen Magnetowiderstand, Hochtemperatur-Supraleitung, Metall-Isolator-Übergang, die oft von nanoskaliger Ordnung von Spins, Ladungen, orbitaler Besetzung sowie Gitterverzerrungen begleitet sind. Dadurch werden diese Materialien interessant für Anwendbarkeit. Magnetit, ein Prototyp eines solchen funktionalen Materials zeigt einen Metall-Isolator-Übergang bei $T = 123$ K. Untersucht man die Ladungs- und orbitale Ordnung sowie die Struktur nach einer optischen Anregung, so findet man, dass die elektronische Struktur und Gitterverzerrung, die kennzeichnend für die Tieftemperaturphase sind, innerhalb der Zeitauflösung des Experiments von 300 fs zerstört wird. Der eigentliche Metall-Isolator-Übergang zeigt sich erst nach 1.5 ps. Die Ergebnisse zeigen, dass MITs in funktionalen Materialien bis zu tausend Mal schneller geschaltet werden können als in vorhandenen Halbleiter-Schaltern.

Seit kurzem rücken auch ferrimagnetische und antiferromagnetische Materialen in den Fokus des Interesses. Es wurde im Ferrimagnet GdFeCo gezeigt, dass der Transfer von Drehimpuls zwischen zwei entgegengesetzten Subsystemen mit unterschiedlichen Zeitkonstanten zu einem Umschalten der Magnetisierung führt. Zudem wurde vorhergesagt, dass Demagnetisierungsdynamiken in antiferromagnetischen Materialien schneller ablaufen soll als in ferromagnetischen, da kein Drehimpuls aus dem Spinsystem abgeführt werden muss. Damit wir mehr über antiferromagnetische Dynamik erfahren haben wir zwei unterschiedliche Antiferromagneten untersucht, um sie mit den bekannten FM zu vergleichen. Im metallischen AFM Holmium fanden wir, dass die magnetische Ordnung schneller und zehnmal energieeffizienter zerstört werden kann als in vergleichbaren FM Metallen. In Europium-Tellurid, einem antiferromagnetischem Halbleiter, haben wir den Zerfall der magnetischen Ordnung im Hinblick auf Wechselwirkungen mit der Struktur untersucht. Wir fanden auf kurzen Zeitskalen eine eher entkoppelte Dynamik. Eine Ausnahme ist ein schneller Beitrag zur Gitterdynamik, den wir mit dem Wegfall von Magnetostriktion erklären.

Die hier gezeigten Ergebnisse wurden mit Hilfe zeitaufgelöster resonanter weicher Röntgenbeugung an der Femtoslicing Strahlungsquelle des Helmholtz-Zentrums Berlin und am freien Elektronenlaser LCLS gemessen. Zusätzlich wird über die Entwicklung und den Bau eines UHV-Diffraktometers für diese Experimente berichtet.

Chapter 3.

Introduction

Information processing and storage technology aims for faster switching, higher data densities, higher read-write-speeds and more energy efficient processes. In order to reach these goals, new concepts of material design and functionality are being discussed. Promising concepts for new applicability involve the use of correlated oxides and materials with antiferromagnetic coupling.

Many of the correlated oxides show a close coupling between spin, orbital, charges, and structural degrees of freedom. These correlations lead to a number of highly interesting phenomena like high-temperature superconductivity (highTc's), metal-to-insulator transitions (MIT), colossal magneto resistance (CMR) and multiferroicity, often accompanied by nanoscale charge order (CO), magnetic order (SO), or orbital order (OO). In order to turn these effects into functionality knowledge about non-equilibrium behavior is needed. Consequently, recent research studies deal with the question, how the interplay between different degrees of freedom affects ultrafast dynamics, in particular the speed of loss of order. For example time resolved measurements done in doped layered nickelates and manganates (LSNO and LSMO) [1–7] found ultrafast loss of order upon photo-excitation on time scale around one picosecond. Caviglia et al. [8] showed in $NdNiO_3$, that during ultrafast excitations the originally magnetic ordering becomes decoupled and mobile on a 2 ps timescale. These examples show, that in such materials the strongly coupled degrees of freedom can indeed be modified on ultrafast timescales.

Magnetite (Fe_3O_4) is a prototype material showing a metal-to-insulator-transition (MIT), where charge and orbital order play a role as well as structural distortions. Since materials showing MIT are particularly interesting for future technology, we investigated this prototype switchable material in a time-resolved pump probe experiment. The degrees of freedom are strongly correlated in thermal equilibrium, but also in our time resolved experiments we find these correlations to be strong. We found an ultrafast loss of charge/orbital order accompanied with a loss of structural distortion to occur within our experimental temporal resolution of 300 fs. Interestingly the phase-transition itself takes place on a delayed timescale of more than one picosecond. The resulting speed for metal-to-insulator transition in a correlated oxide is at least thousands times higher than the speed of conventional semiconductor switches.

The other class of interesting materials are materials with non-parallel magnetic order. Ultrafast magnetic dynamics started with the results found by Beaurepaire et al. [9] presenting the possibility to reduce magnetization of a thin Ni-film within a few hundreds of femtoseconds upon laser excitation. Since then, various ultrafast studies investigated the manipulation of spin systems mainly in FM materials like Ni, Fe, Gd, and Tb or Alloys [10–16]. Associated with the experiments, theoretic models [9, 13, 17] were developed but details of ultrafast spin manipulation are still being debated. What is mostly agreed on, is that spin manipulation in ultrafast FMs is limited by how fast how fast angular momentum can be transferred out of the spin system. Since in systems with non-parallel spins like ferri- and antiferromagnets, spin order can be manipulated by angular momentum transfer within the spin system, their dynamics should be different. Indeed, it has been predicted, that antiferromagnetic should be much faster than ferromagnetic dynamics [18, 19]. Experimentally, however, only a few AFM oxides have been studied [20–23] which are not easy to compare to the wealth of experimental results available for FM metals.

In this thesis first results from the prototype antiferromagnetic metal Holmium are reported, which can be directly compared to dynamic studies from ferromagnetic metals. In a resonant diffraction experiment, which probes directly the AFM order parameter, Ho shows indeed faster dynamics than the comparable FM metal Tb. Remarkably, AFM order in Ho can be ten times more efficiently pumped compare to FM metals. This finding may open up the route towards more energy efficient switching, in, e.g., an all optical pumping scheme as demonstrated for the $4f-3d$ hybrid system GdFeCo [24].

As a non-metallic antiferromagnet the semiconductor Europium-Telluride (EuTe) was studied. The focus was here on the relation between spin and lattice dynamics. Both degrees of freedom were studied in one and the same time-resolved experiment. Looking on the nature of the AFM in EuTe, one expects a strong coupling between lattice and antiferromagnetism. It turned out during the time resolved experiments, however, that their dynamics are essentially decoupled on short timescales. Simulations of the structural disorder [25–27] showed that they are mainly shock wave dominated. In one of the experiments we also investigated the aspect of indirect pumping and spin current as found by Battiato et al. [28, 29] and Eschenlohr et al. [16]. Having pumped only indirectly, we found also indications of an additional magnetically induced lattice dynamics (ultrafast release of magnetostriction).

3.1. Outline

In the next chapter 4, I will describe the technique resonant soft x-ray diffraction and why this method is the perfect tool to investigate dynamics in AFMs and correlated oxides. I will further summarize the optical aspects relevant in laser pump - soft x-ray probe measurements. In the subsequent chapter 5, I will describe the experimental setup starting with the used ultrashort pulse soft x-ray sources FEMTOSPEX at BESSY II and the free electron lasers (FLASH, LCLS). I will continue with a description of the experimental chamber that was setup in the framework of this thesis. The following chapters present the results of our studies in magnetite in chapter 6, and 7, in Holmium in chapter 8 and in EuTe in chapter 9. I will then discuss/summarize the experimental part and scientific findings in the chapter 10. Chapter 11 contains a list of all publication I was involved in. In the appendix you will finally find more experimental details of the UHV-diffractometer in Sec. A.1.1 plus additional information about the data acquisition in Sec. A.1.2.

Chapter 4.

Method

Magnetic x-ray diffraction is an experimental method that not only provides quantitative information about the degree of AFM order, but also gives insight into spatial correlations. Depth profiling is also possible within the absorption length of x-rays. Though, in general, magnetic x-ray diffraction has been known for long, but rarely used due to the small scattering cross sections. This changes, however, in proximity to electronic resonances. Thus Resonant Soft X-ray Diffraction (RSXD) experienced a considerable upturn during the last two decades [30–32]. It is ideally suited to investigate electronic order in general and magnetic ordering phenomena in particular (here it is called Resonant Magnetic X-ray Scattering (RMXS)). Moreover, by using ultrashort x-ray pulses it can be combined with femtosecond temporal resolution and is therefore the technique of choice to study ultrafast phase transitions.

In the ultrafast demagnetization business, Magneto-Optical Kerr Effect (MOKE) [33] and X-ray Magnetic Circular Dichroism (XMCD) [34] are well established methods. However, since those techniques measure the magnetization, they can not be applied to AFMs where no net magnetic moment is present. RMXS is exactly filling this gap by being sensitive to the order parameter and is therefore an ideal tool to study AFMs and other electronically ordered systems.

The following sections introduce x-ray diffraction and provide the main formalism of that technique. Furthermore, the strength of resonant soft x-ray diffraction will be highlighted. Finally, the most important aspects for optical and x-ray experiments are discussed.

4.1. X-ray Diffraction

When x-rays interact with matter, they are scattered by electrons. Bragg's law describes the condition for constructive interference when plane waves e.g. of electromagnetic radiation are scattered from a 3d crystal in a specular geometry.

In Fig. 4.1 a schematic scattering experiment from a single crystal is shown. Scattered plane waves with wavelength λ interfere constructively into a specific direction, when the Bragg condition is fulfilled. In the shown case the scatterers for this particular outgoing direction are spaced by distance d_{hkl}. Constructive interference can be observed, if the following equation is fulfilled [35]:

$$m\lambda = 2d_{hkl}\sin\left(\frac{\Omega}{2}\right); m \in \mathbb{Z}. \tag{4.1}$$

More generally, constructive interference follows the Laue condition in reciprocal space. The Laue-condition is fulfilled when the scattering vector $\vec{q}$ is equal to a reciprocal lattice vector $\vec{G}$:

$$\vec{q} = \vec{k}' - \vec{k} \overset{!}{=} \vec{G}, \tag{4.2}$$

where $\vec{k}$ and $\vec{k}'$ are the wave vectors of the incident and scattered radiation respectively. We only consider elastic scattering, such that $\vec{k}$ and $\vec{k}'$ have the length $k = \frac{2\pi}{\lambda}$. λ is

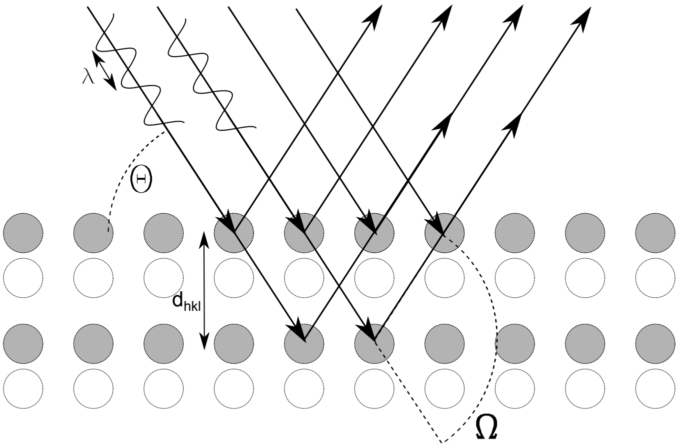

Figure 4.1.: Illustration of the Bragg's Law: Incoming light waves with wavelength λ will scatter only from the gray shaded atoms. Here, atoms shown with open circles do not contribute to the scattering.

associated with the photon energy E by the Planck relation:

$$\begin{aligned} & E = h\nu = h\tfrac{c}{\lambda} \\ \Leftrightarrow \quad & \lambda[\text{Å}] \cdot E[\text{eV}] \approx 12398, \end{aligned} \tag{4.3}$$

with ν the frequency of the light, c the speed of light and h ($\hbar$) the Planck constant (reduced Planck constant).

A periodic structure in real space is associated with a periodic pattern in the reciprocal space. A family of scattering planes associated with constructive interference is referred to the Miller indices (HKL). Each index denotes a plane orthogonal to a direction (HKL) in the basis of the reciprocal lattice vectors.

The scattering amplitude is given by the elastic scattering cross section (see [36–38]):

$$\frac{d\sigma_{\text{scat}}}{d\Omega} = r_0^2 \cdot |\mathcal{F}|^2, \tag{4.4}$$

with r_0 the Thomson scattering length or the classical electron radius $r_0 = \frac{\mu_0 e^2}{4\pi m_\text{e}} = 2.82 \cdot 10^{-5}$ Å , with m_e the electron mass, μ_0 the vacuum permeability, e the electric charge and $d\Omega$ the solid angle. $\mathcal{F}$ describes the relation between the electric fields of the incident and diffracted beam: $E_{out} = \mathcal{F} \cdot E_{in}$. $\mathcal{F}$ is a superposition of atomic form factors, f_S, weighted with appropriate phase factors times the number of coherently scattering unit cells N. Equation 4.5 shows the exact relation:

$$\mathcal{F} = N \sum_l f_l e^{i\vec{q}\vec{r}_l} = N f_\text{S}. \tag{4.5}$$

The vectors $\vec{r}_l$ in the sum represent the positions of the atoms with respect to an origin in the crystal. The Laue-condition is fulfilled when $e^{i\vec{q}\vec{R}_n} = e^{i2\pi\cdot m} = 1$ with $m = 1, 2, \ldots$ or $\vec{q} \cdot \vec{R}_n = 2\pi \cdot m \Leftrightarrow \vec{q} = \vec{G}$.

4.2. Magnetic X-Ray Diffraction

Non-Resonant Magnetic X-Ray Scattering

The previous section introduced only the scattering from the total charge distribution mainly probing the crystal structure, i.e. non-resonant scattering (charge scattering or Thomson scattering). For the experiments reported here we want x-rays to be sensitive to the spins. Generally there is an interaction of x-rays with the spin of the electrons that yields a non-resonant magnetic scattering contribution [39, 40]. This magnetic scattering amplitude f_{mag} is described as [41, 42]:

$$f_{\mathrm{mag}} = i r_0 \frac{\hbar\omega}{m_e c^2} \left[\frac{1}{2} A \; L(Q) + B \; S(Q) \right], \tag{4.6}$$

where L and S denote the Fourier transforms of the atomic orbital and spin moment densities, respectively, and A and B describe the polarization dependencies. Due to the prefactor $\frac{\hbar\omega}{mc^2}$, however, the magnetic scattering amplitude is very weak. For typical x-ray energies, the non-resonant magnetic scattering signal is about six orders of magnitude smaller than the charge scattering intensity.

Resonant Soft X-Ray Diffraction

When tuning the x-ray energy to element specific resonances, additional contributions to the scattering amplitudes become relevant. Close to electronic resonances, there is an enhanced contribution to the scattering amplitude caused by a virtual excitation of a core-level electron into an unoccupied intermediate state and the subsequent decay with emission of a photon. The cross section for the whole elastic scattering process is in second order perturbation theory given by [38, 43]:

$$\sigma = \frac{2\pi}{\hbar} \left| \langle f | H_{\mathrm{int}} | i \rangle + \sum_n \frac{\langle f | H_{\mathrm{int}} | n \rangle \; \langle n | H_{\mathrm{int}} | i \rangle}{E_{\mathrm{i}} - E_{\mathrm{n}} + \hbar\omega + i^{\Gamma}/2} \right|^2, \tag{4.7}$$

where the Hamiltonian H_{int} describes the interaction of the electromagnetic wave with the bound electrons. The first term represents the non-resonant Thomson scattering, while the second term, involving the coupling of an initial state $|i\rangle$ to the intermediate state $|n\rangle$ with lifetime broadening Γ, quantifies the additional resonant contribution. Because of the energy difference in the denominator $E_{\mathrm{i}} - E_{\mathrm{n}}$, this part of the scattering cross section can become huge when the photon energy is tuned to electronic resonances. This leads to a resonant enhancement by several orders of magnitude [31, 38, 44]. The magnetic and spectroscopic sensitivity of resonant scattering results from a high sensitivity to the intermediate state $|n\rangle$ which turns the scattering experiment effectively into an selective probe of valence electronic structure. Different charge states and orbital occupations are reflected in a different energy dependent scattering amplitude. Therefore the RSXD-technique is sensitive not only to the lattice structure, but also to spatial modulations of the orbital and charge state.

Including the resonant interaction between photons and electrons, the atomic form factor can be written as:

$$\hat{f} = \hat{f}^0 + \hat{f}' + i\hat{f}''. \tag{4.8}$$

$\hat{f}^0$ is the essentially isotropic, non-resonant term. The energy dependent (resonant) contributions are $\hat{f}'$ and $\hat{f}''$ and describe the real and imaginary part of the dispersion corrections.

Resonant scattering provides also magnetic sensitivity: For a magnetic ion, the scattering probabilities of left and right circularly polarized photons (LCP, RCP) are different when the dipole excitation creates a core hole in a state carrying angular momentum. For transition metals and lanthanides this is the case for the $2p \rightarrow 3d$ ($L_{2,3}$) or $3d \rightarrow 4f$ ($M_{4,5}$) transitions, respectively, which are located in the soft x-ray region between 450 and 1580 eV. For ferromagnets, this leads to an asymmetry in the absorption of photons of different helicities, depending on the direction of the local magnetization, known as x-ray magnetic circular dichroism (XMCD) in absorption. Because of the close relation between absorption and scattering magnetic phenomena can also be probed with resonant soft x-ray diffraction experiments.

The total scattering amplitude of a resonant $E1$ (dipole) process is proportional to [31]:

$$\begin{aligned} f^{res}(\nu, \vec{\varepsilon}, \vec{\varepsilon'}) \propto \Big(& (\vec{\varepsilon'}^{\dagger} \cdot \vec{\varepsilon}) \, [F_{11} - F_{1-1}] \\ & - i(\vec{\varepsilon'}^{\dagger} \times \vec{\varepsilon}) \cdot \vec{\mu} \, [F_{11} - F_{1-1}] \\ & + (\vec{\varepsilon'}^{\dagger} \cdot \vec{\mu})(\vec{\varepsilon} \cdot \vec{\mu}) \, [2F_{10} - F_{11} - F_{1-1}] \Big), \end{aligned} \tag{4.9}$$

with $\vec{\varepsilon}, \vec{\varepsilon'}$ being polarization vectors of the incoming and outgoing light and $\vec{\mu}$ the unit vector pointing in the direction of the local magnetic moment. $F_{1\mathrm{n}}$where $n = -1, 0, 1$ represents the polarization dependent dimensionless resonant oscillator strengths for $\Delta M_{\mathrm{J}} = 0, \pm 1$ dipole transitions. The first term is independent on the magnetization direction in the sample. The second term is linearly dependent on $\vec{\mu}$ and corresponds to the local circular dichroism. The third term in Eq. (4.9) is proportional to the square of the moment and corresponds to the linear dichroism part in the resonant scattering process. In a RSXD-experiment we are therefore able to detect and distinguish element specific periodic order of all electronic degrees of freedom and therefore charge-, spin- or orbital ordering phenomena.

4.3. Optics

In many non-resonant cases, the contribution of $\hat{f}'$ can be neglected. For soft x-rays near electronic resonances, this approximation breaks down and the real part of the scattering amplitude, $\hat{f}'$, can no longer be approximated as zero such that a full x-ray optical description of the scattering process may be needed [45, 46]. For optical photons that we used for exciting the system the contribution of $\hat{f}'$ is always considerable. In the following section I briefly introduce some optics aspects that are important for experiments with electromagnetic radiation (both in the visible or x-ray range) at any interface. These considerations are relevant to estimate the excitation and probing conditions for any laser-pump - x-ray-probe scenario and for the corresponding data evaluation and interpretation.

When electromagnetic radiation is incident on an interface it is partially reflected and partially transmitted. For the transmitted fraction refraction occurs. Propagation of electromagnetic radiation within a material is furthermore accompanied by absorption. All the above phenomena are a consequence of the material's response to the perturbation by the electromagnetic wave. This response can be described by the energy, dependent complex refraction index, $\kappa^*(E)$, which is directly associated with the dielectric function, $\varepsilon^*(E)$ [47]:

$$n^*(E) = n(E) + i\kappa(E) \tag{4.10}$$

$$\varepsilon^*(E) = \varepsilon_1(E) + i\varepsilon_2(E). \tag{4.11}$$

Here n, the real part, is the refractive index which describes the dispersion, κ, the imaginary part, is the extinction coefficient, also called the attenuation index. ε_1 describes the polarizability and ε_2 the absorption. As n^* is equal to $\sqrt{\varepsilon^*}$, this leads to the relations [47]:

$$n = \left(\frac{(\varepsilon_1^2 + \varepsilon_2^2)^{1/2} + \varepsilon_1}{2}\right)^{1/2} \tag{4.12}$$

$$\kappa = \left(\frac{(\varepsilon_1^2 + \varepsilon_2^2)^{1/2} - \varepsilon_1}{2}\right)^{1/2} \tag{4.13}$$

$$\varepsilon_1 = n^2 - \kappa^2 \tag{4.14}$$

$$\varepsilon_2 = 2n\kappa. \tag{4.15}$$

Refraction at an interface is described by Snell's law which is a consequence of the requirement of continuity of the electromagnetic field and its derivative at the interface (see Fig. 4.2):

$$\frac{n_1}{n_2} = \frac{\cos\alpha_2}{\cos\alpha_1}. \tag{4.16}$$

Here α_1 and α_2 refer to the angles between the propagation directions of the waves and the interface of the media (see Fig. 4.2(a)). The same argument yields the Fresnel equations quantifying the electromagnetic field amplitudes of the reflected (r_p) and

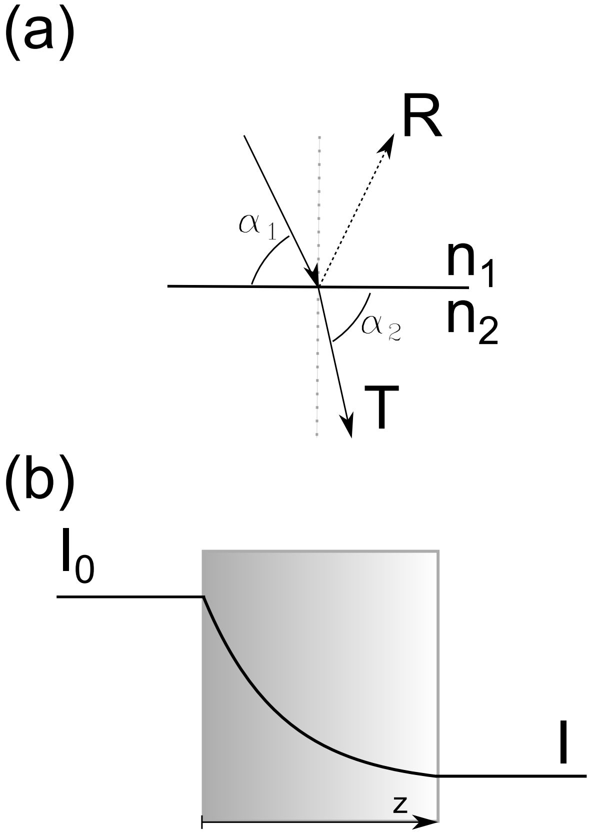

Figure 4.2.: Visualization of (a) Snell's-Law and (b) Lambert-Beer-Law. (a) The incoming beam hits the interface of two media with refraction indices n_1, n_2. The incidence angle with respect to the surface is α_1, the refracted light propagates into the medium with n_2 under an angle α_2. (b) A part of the incoming intensity I_0 is absorbed in the material dependent on the penetration depth z, resulting in an intensity I.

the transmitted (t_p) beam.

$$r_\mathrm{p} = \frac{n_2 \sin\alpha - n_1 \left(1 - \left(\frac{n_1 \cos\alpha}{n_2}\right)^2\right)^{1/2}}{n_2 \sin\alpha + n_1 \left(1 - \left(\frac{n_1 \cos\alpha}{n_2}\right)^2\right)^{1/2}} \tag{4.17}$$

$$t_\mathrm{p} = \frac{2 n_1 \sin\alpha}{n_2 \sin\alpha + n_1 \left(1 - \left(\frac{n_1 \cos\alpha}{n_2}\right)^2\right)^{1/2}}. \tag{4.18}$$

The reflected part of an incoming beam intensity is then $R = r^2$, whereby $1 = R + T$ with T being the transmission.

The intensity of a photon beam transmitting a material decreases due to absorption. The intensity then depends on the traveled pathway and is quantified by the Lambert-Beer-Law (see Fig. 4.2(b)) [48]:

$$I(z) = I_0 e^{-\mu z}. \tag{4.19}$$

Here $\mu(E)$ is the absorption coefficient, I_0 the initial intensity at the surface ($z = 0$) and $I(z)$ the intensity at a distance z from the surface measured along the beam direction. The absorption coefficient μ itself is proportional to the imaginary part of the refractive index by:

$$\mu = \frac{2\pi}{\lambda}\kappa. \tag{4.20}$$

The design of a laser pump - x-ray probe experiment has to consider these points. Ideally one would like to probe a homogeneously pumped sample volume, which means that the penetration depths of the optical pulses should be larger than that of the x-rays (see illustrated in Fig. 4.3). Sometimes via a clever choice of sample orientation, photon energies (to tune the penetration depths) and sample thickness the conditions can be optimized. Generally, in a diffraction experiment, both light pulses do not hit the surface normally but under an angle α_1. Therefore refraction matters and the spot sizes on the sample surface are larger as compare to normal incidence (see illustrated in Fig. 4.3). To calculate the correct pump fluence in such a time resolved measurement, we further need the energy-dependent x-ray penetration depth $\lambda_\text{x-ray}$, the energy-dependent optical penetration depth λ_opt, the transmission of the optical light trough the surface layer T (calculated by Fresnels formalism in formula (4.18)), the sample thickness, the incoming laser fluence F_0 for normal incidence, and the incoming angle of the light rays on the sample α_1. We assume here a collinear pumping geometry such that α_1 is the same for x-rays and optical photons, which was the case for all experiments in this study. The absorbed laser fluence weighted with the x-ray probing volume[1] for a bulk crystal can be calculated from the fluence

---

[1] Refraction of x-rays can be neglected for our type of experiments.

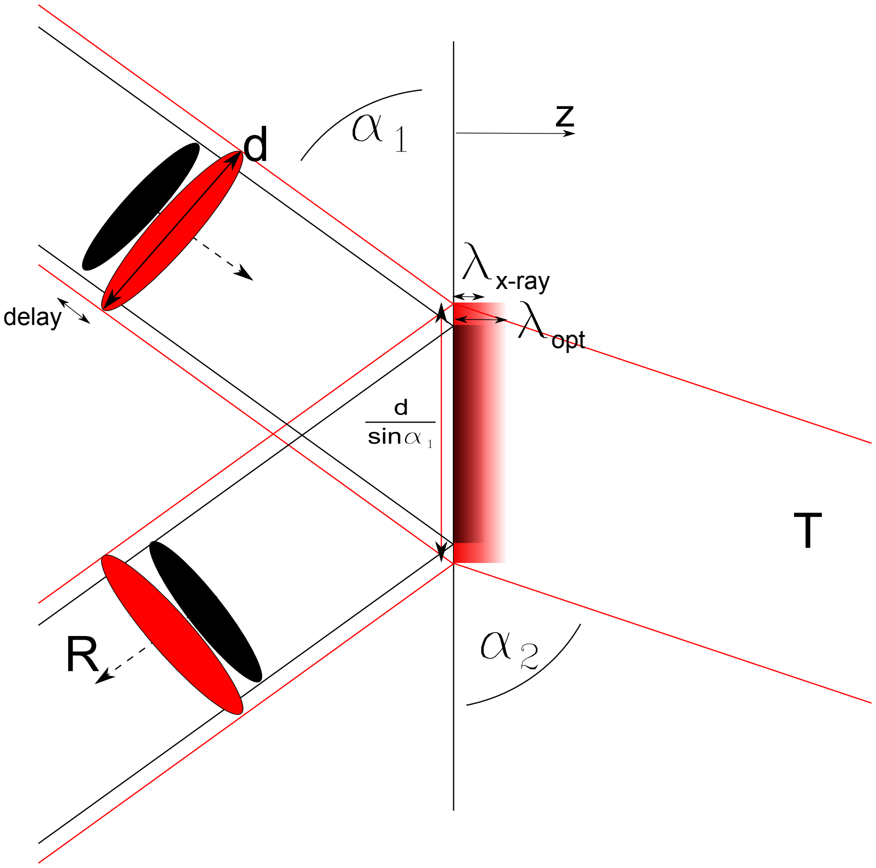

Figure 4.3.: Visualization of a pump-probe setup. The red pulse of diameter d is hitting the surface at $z = 0$. Due to the incident angle α_1, the laser spot footprint is enlarged by a factor of $^1/_{\sin\alpha_1}$. A part of the optical laser pulse is reflected (R), the other part is transmitted and partially absorbed (absorption length λ_{opt}) under a different angle α_2. The sketch shows the optimal case: The x-ray spot (symbolized by black) is smaller than the optical laser pulse, and the respective penetration depth is shorter ($\lambda_{\text{x-ray}}$).

averaged over z, weighted by the x-ray probe damping at the same z:

$$
\begin{aligned}
F &= \frac{\int\limits_0^\infty F_{opt}(z) e^{-\mu z} \mathrm{d}z}{\int\limits_0^\infty e^{-\mu z} \mathrm{d}z} && (4.21)\\
F_{\mathrm{opt}}(z) &= F_0 T e^{-z/\lambda_{\mathrm{opt}}} \frac{1}{\sin \alpha_1}, && (4.22)
\end{aligned}
$$

with $1/\sin\alpha_1$ correcting for the footprint. These equations together with Lambert-Beer-Law (4.19), whereby $\lambda_{x-ray} = 1/\mu_{x-ray}$ lead to:

$$
F = F_0 T \cos\alpha_1 \frac{\lambda_{\mathrm{opt}} + \lambda_{x-ray}}{\lambda_{x-ray}}. \tag{4.23}
$$

The absorption coefficients/penetration depths in the optical and/or x-ray regime can be calculated from the real and imaginary part of the refractive index. For energies far from electronic resonances these values can be taken e.g. from the 'Henke tables' [49] for x-ray energies. In case of magnetite we determined the x-ray penetration depth experimentally in a transmission experiment. For Ho, the data were taken from Refs. [44, 50], for EuTe from Refs. [51–53], for PbTe from Refs. [53–55] and for BaF_2 from Refs. [53, 56].

Chapter 5.

Experiments

The central experimental technique applied in this thesis is time-resolved resonant soft x-ray diffraction in a pump-probe scheme. The study of ultrafast photon induced processes with x-rays requires sources of ultrashort photon pulses. In pump-probe experiments the high temporal resolution is achieved by a combination of ultrashort laser pulses with lengths on the order of tens of femtoseconds and x-ray pulses of similar duration. While the optical laser pulses can be generated by commercially available systems, the generation of ultrashort x-ray pulses is more difficult. In particular when a variable photon energy is required as in resonant scattering experiments.

In this chapter I will first present the experimental and technical details of the used light sources which were the slicing source at BESSY II and LCLS. During my research, I also carried out experiments at the FLASH, which led, e.g. to the publication [57]. These are, however, not part of this thesis. Subsequently a rather detailed description of the UHV-diffractometer used at BESSY II and FLASH follows, which was developed and built within the framework of this thesis. Further details are given in the Appendix.

5.1. Sources of ultrashort x-ray pulses

Intense ultrashort photon pulses in the IR or visible range have been available since the early 1990's with the advent of the ultrafast laser technique. For photon energies in the UV, soft, and hard x-ray range, however laser technology fails and other techniques like higher harmonic generation (HHG) [58–60], plasma sources [61–63] and accelerator based photon sources were developed. Among those the accelerator based photon sources have the great advantage of tunable photon wavelength in a wider energy range, and a generally higher photon flux. The first accelerator based femtosecond x-ray sources became operational a few years after the turn of the millennium [64]. Today two types of accelerator based photon sources are routinely available for ultrafast x-ray experiments. There are synchrotron based [65–69] and free electron laser (FEL) based sources [70–72]. While current x-ray FELs have the great advantage of high flux, short pulses, a high degree of transversal coherence, there are strong limitations to the stability of the beam conditions since the radiation is essentially produced through the amplification of radiation that is subject to shot noise. Current x-ray FELs are also limited to producing linear polarized light beams. In contrast slicing sources have the great advantage of more stable beam conditions due to the storage ring stability, good overall time resolutions due to the intrinsic synchronization of the probing x-rays with a pump lasers and the production of circular polarized x-ray light in the soft x-ray region. Nevertheless, a big disadvantage is the low photon flux due to the slicing process.

5.1.1. Storage ring based 'slicing' sources: FEMTOSPEX

Generally storage ring based x-ray sources provide x-rays with a pulsed time structure [73–75], determined by the filling pattern. In regular operation modes the typical pulse length is of the order of 100 ps. With optimized electron optics settings which allow for longitudinal compression and transverse expansion of the electron bunches (low-alpha mode), the pulse length of all stored electron bunches can be reduced down to around 30 ps FWHM. To generate even shorter pulses of femtosecond duration the so-called slicing technique is used.

Zholents and Zolotorev [65] developed the principle ideas in 1996, which was first implemented at the ALS in Berkeley, USA, using a bending magnet as a radiator [64]. The first undulator source for the soft x-ray range was commissioned at BESSY II in 2004 [66–68], followed in 2006 by a hard x-ray undulator source at the SLS in Villigen, Switzerland [69].

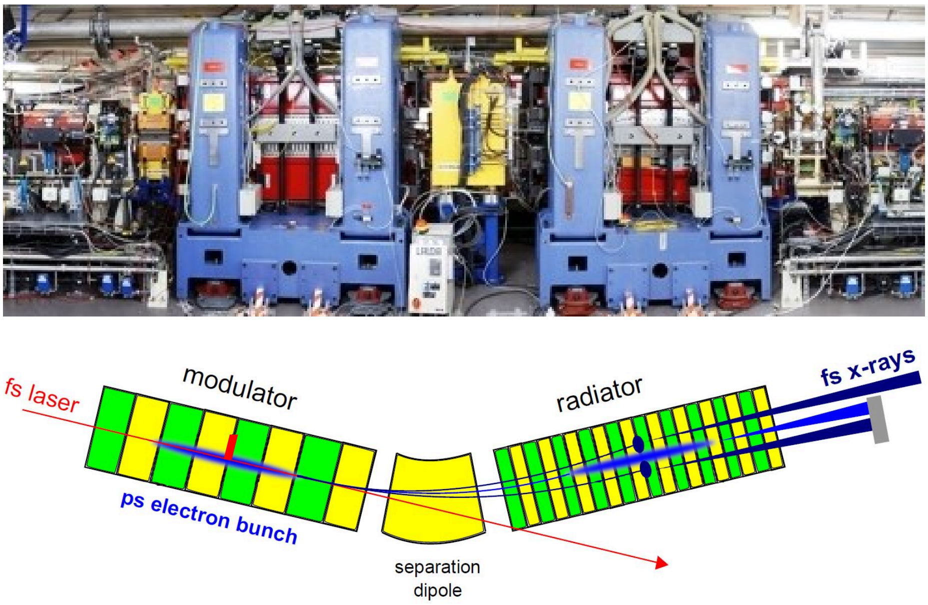

Figure 5.1.: Picture and schematic of the U139 planar undulator, called modulator (left), followed by a dipole magnet and the UE56/1 elliptical undulator, called radiator. All electrons (the small fs part (dark blue) and the big ps part (lighter blue) in the sketch) produce photons in the radiator but the fs photons are spatially separated from the big ps bunch and can be therefore blocked with apertures (gray block) [76].

A synchronized laser pulse (red), with a pulse duration of around 50 fs co-propagates with the electrons in a long-period undulator, the so-called modulator as illustrated in Fig. 5.1. The modulator gap is tuned such, that a resonance condition with the laser field is fulfilled in order to modulate the energy of a part of the electrons in the bunch [68]. The part of the electron bunch that temporally overlaps with the much shorter laser pulse interacts coherently with the electric field of the laser pulse during the co-propagation such that one part gains kinetic energy while the other part loses energy, respectively (about ± 1 % of 1.7 GeV). All other electrons (99.99 %) remain unaffected at their initial kinetic energy. In the subsequent dipole magnet the electrons are deflected by an angle that depends on their individual kinetic energy (see Fig. 5.1). In this way an angular separation (up to 1 mrad) of the electrons with modulated energy from the regular bunch is achieved (Fig. 5.1). At BESSY II, the electron orbit in that section can be tuned such that the trajectory of those electrons with reduced kinetic energy lies on the undulator axes of the radiator. Those electrons emit their radiation into the beamline whereas the radiation of the electrons from the unmodulated part of the bunch and the part of the electron bunch with increased energy is blocked by the beamline apertures. The pulse length of the radiation emitted by the energy modulated electrons is basically retained from the fs-laser pulse. The radiator is an APPLE-II type undulator which allows to choose between either vertical linear or elliptically polarized fs x-ray pulses in the photon energy range from 400 to 1500 eV. The slicing source produces between 10^6 to 10^7 photons per second per 0.1 % bandwidth and 100 fs (FWHM) [68] pulses. At the moment the slicing source at BESSY II is the only place in the world where femtosecond soft x-ray pulses with variable polarization are available.

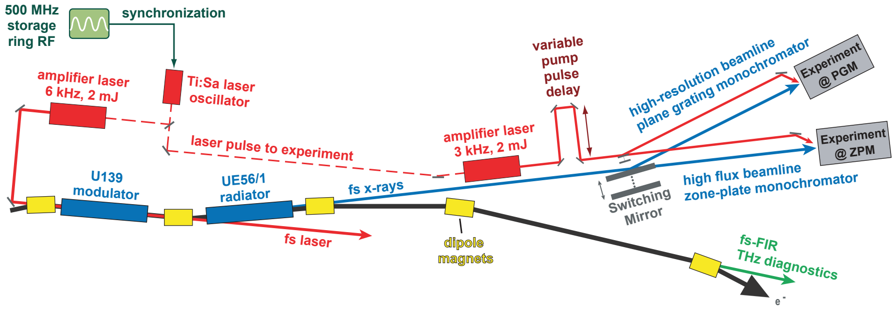

Figure 5.2.: Schematic of the whole FEMTOSPEX facility.

The intrinsic synchronization between pump pulse and x-ray probe pulse comes from the fact that both the fs amplifiers used for generating the slice in the storage ring and the one used to photo-excite the sample are seeded by one single oscillator, as can be seen in Fig. 5.2 (top left corner). All components are synchronized to the BESSY II master clock (500 MHz). The fs x-rays are symbolized in Fig. 5.2 with blue arrows. The optical laser paths are indicated as red arrows. The main limitation of a slicing source is the low photon flux, while linear accelerator based sources produce as many photons per shot as produced at a typical storage ring beamline per second, as described in the following section.

5.1.2. Free electron lasers: FLASH and LCLS

Linear accelerator based x-ray sources (or free electron lasers (FELs)) were designed to investigate processes which are extreme photon hungry, and need ultrashort x-ray pulses and a high coherent photon flux. The two FELs which were used for the here described experiments are the Free electron LASer Hamburg (FLASH) for VUV / soft x-rays and the Linac Coherent Light Source (LCLS), Stanford, USA, for hard and soft x-rays.

The work principle of a SASE-FEL is the following (SASE stands for the self-amplified spontaneous emission): Electron bunches are generated, accelerated and compressed to lengths as short as a couple of femtoseconds. The compressed bunches enter a long undulator where they start to emit spontaneous undulator radiation. Along the length of the undulator the intensity of the spontaneous radiation eventually grows to such a high level that its electric field begins to interact with the electrons: The electrons are forced into a sliced spatial structure of so-called microbunches (compare Fig. 5.3). Eventually the individual microbunches wiggle in phase in the undulator magnetic field which leads to the emission of coherent light waves and hence to an exponential growth of intensity [77–79]. Saturation occurs when kinetic energy losses due to photon emission starts to destroy the microbunch structure. The peak brilliance can amount up to 10^{32} photons / (s·mrad^2·mm^2·0.1% BW) compared to 10^{22} photons / (s·mrad^2·mm^2·0.1% BW) at a BESSY II undulator [80].

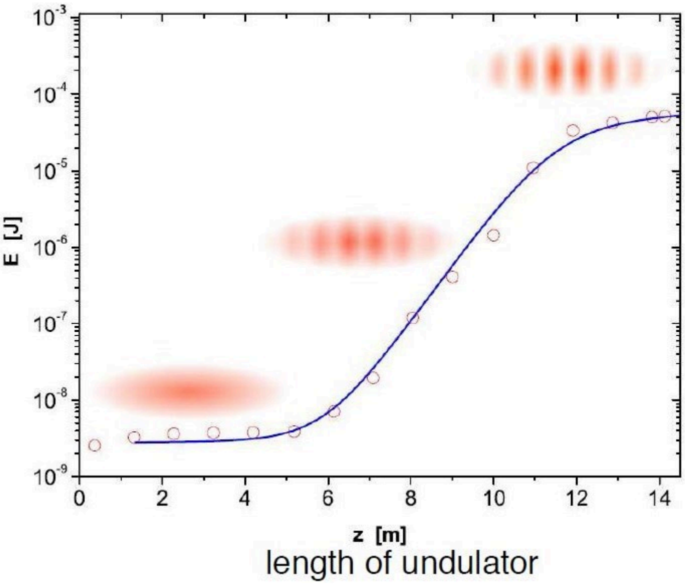

Figure 5.3.: Measured pulse energy of the FEL as a function of the length of undulators depicted with the respective schematic picture of the energy modulation. Picture taken from [81].

The SASE principle has a major disadvantage: For every single electron pulse the SASE process occurs for a randomly set of discrete wavelengths (so called longitudinal modes of the FEL) within a bandwidth of the order of one percent. This results in photon pulses with a random energy spectrum and spiky temporal structure which are far from being bandwidth-limited. In Fig. 5.4 five spectra of five different pulses are shown (black curves). The averaged spectrum (red dashed curve) considerably differs in shape from the single-shot spectra. This randomness of the energy spectrum combined with monochromatization, which e.g. is essential for spectroscopic measurements, translates into severe shot-to-shot intensity fluctuations [79, 82] which require shot-to-shot intensity normalization or averaging over larger numbers of shots. Another problem for ultrafast experiments at a SASE-FEL is the lack of natural synchronization between the x-ray pulses and the fs laser pulses used to pump the sample because of the temporal jitter of the electron acceleration and the randomness of the SASE processes. High temporal resolution requires complex and shot-to-shot arrival time measurements [83, 84] of the x-ray pulse which only recently have routinely become available (e.g. at LCLS). In typical time-resolved experiments a temporal resolution in the sub 100 fs range can be achieved. Some of the SASE related issues can be avoided by using laser seeded FELs (like FERMI@Elettra[1], an UV/VUV-FEL in Trieste) but so far laser seeding is not available for higher photon energies.

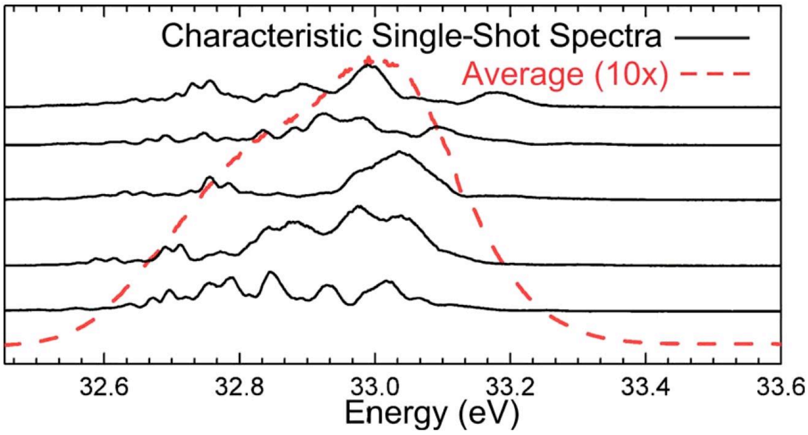

Figure 5.4.: Spectra of five single shots measured at FLASH recorded at 33.2 *nm* wavelength. The red line is the average over 2600 single shots. Picture taken from [82].

5.2. Beamlines

After generation of the ultrashort x-ray pulses the properties of the x-ray beam usually have to be refined for the use with time resolved measurements to match the

---

[1] Free Electron Laser for Multidisciplinary Investigations)

experimental requirements. This includes forming of the beam shape (e.g. focusing onto the sample), monochromatization and possibly attenuation. A slicing source and an FEL lead to different requirements for a beamline. While a slicing source typically needs maximal transmission at the expense of energy resolution, an FEL allows for beamline instrumentation that achieves higher spectral resolution. On the other hand the photon energy tunability of an FEL is presently still limited since existing FELs only use fixed gap undulators which only provide a fixed photon energy range for fixed accelerator settings. An overview on parameters for the used beamlines is given in Table 5.1.

	BESSY UE56/1		FLASH	LCLS
	PGM	ZPM[2]	PG2	SXR
Photon Flux (per s/0.1% BW)	10^5	10^7	10^9	up to 10^{12}
Total time resolution including pump laser (FWHM in fs)	down to 130	130	300	300
Energy range (eV)	400-1500		20-600	480-2000
Bandwidth ($^E/_{\Delta E}$)	1000-20000[3]	$\sim$ 500	500	2000-3500
Focus size (vert x hor)(μm^2)	85 x 15	300 x 100	down to 50 x 50	down to 13.2 x 13.2
Repetition rate	6 kHz		typ. 100 bunches per train à 10 Hz	up to 120 Hz

Table 5.1.: List of source parameters and the properties of the particular beamlines used for present pump - probe experiments.

5.3. Scattering endstations

As all experiments in this work use soft x-rays as a probe, the experimental setups are comparably complex. Soft x-rays are quickly absorbed (small free mean path) in air and the whole experiment has to be in vacuum. Figure 5.5 represents a typical scattering geometry. The incoming beam hits a sample in the center of the scattering chamber. The sample can typically be translated into three different directions (x, y, z),

---

[2] The ZPM at BESSY II has been re-build after the experiments reported here were carried out, leading to improved performance with , e.g, a smaller beam focus

[3] Exact number depends on the used grating. 1000 for high time resolution (150 lines/mm), 20000 for high energy resolution (1200 lines/mm)

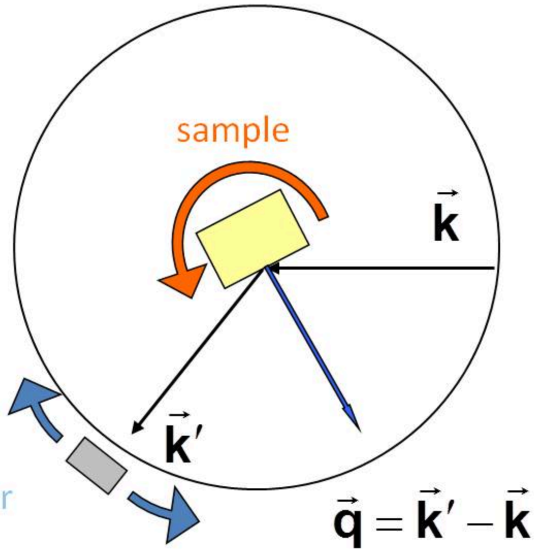

Figure 5.5.: Schematic of a two-circle diffractometer.

and be rotated about its azimuth. The angle of incidence of the x-rays is varied with a rotational stage. With a second rotational stage the detection angle is changed (0° refers to the detector in the direct beam, 180° to back-scattering geometry). The details of implementation of such an UHV-diffractometer differs from one experiment to the other as every end station is optimized for different requirements, in terms of the degree of accuracy of the rotational stages, the UHV-conditions, the size of the chamber or all the inserts (sample environment, detectors, slits). In many setups the motor management and control of all motorized devices and of the beamline is done via the commercial software SPEC [85], which is described in more detail in the Appendix (A.1.2).

5.3.1. Diffraction chamber

For the experiments at the LCLS we used the RSXS (Resonant Soft X-ray Scattering station) chamber of our collaborators for which we designed a low temperature sample stage (see Sec. 5.3.3). Details of the instrument can be found in Ref. [86]. For the experiments at BESSY/FLASH we used our own UHV-chamber which was built and commissioned by Marcel Buchholz and myself.

The instrument (see Fig. 5.6) is built for ultra high vacuum conditions ($\leq 10^{-9}$ mbar), contains a (4+1)-circle diffractometer (rotating 'lid' as main detector circle (CF 500) and a CF160 2nd circle for the sample rotation), multiple detectors (in-vacuum CCD, polarization analyzer, fluorescence detector, Si-diodes or fast APDs, a cryostat ($\leq$5 - 450 K), a small preparation chamber and a sample transfer. It consists of a stainless steel vacuum tank with an inner diameter of 500 mm and an inner height of about 600 mm. Two times eight CF160 flanges radially mounted in two levels allow flexible access from all sides. The bottom and the top flange contain a central CF160 port surrounded by CF100 flanges. The bottom CF500 is fixed whereas the top flange is rotatable. In the lower flange plane equipment is mounted that is needed to create and analyze the vacuum (turbo pumps, cooling trap with a Ti sublimation unit, pressure gauges, and mass spectrometer). The upper level is at the beam height and contains the beam port, a window flange with a fluorescence screen opposite to the beam port and windows for external cameras, external light, sample transfer, tools for azimuthal rotation, and flange mounted CCD cameras. Figure 5.6 shows the instrument during its first commissioning at DESY at the BW3 beamline of the former storage ring DORIS III .

5.3.2. Sample Transfer System

Among various other parts of this instrument, I developed a sample transfer system, that matches the requirements of this experimental station, and can be applied elsewhere. In the mean time it has been installed in several different experimental stations like in the FEMTOSPEX-diffraction chamber ([87, 88]), in the new RIXS-endstation [89] at BESSY II and in three different coherent diffraction setups. Figure 5.7 shows the system. The samples are mounted on circular sample disks. These disks are fitted into copper shuttles, that fit in a sample garage (see Fig. 5.7b). This garage is mounted to a long magnetic driven linear and rotational feedthrough, which can translate the sample from the differential pumped load lock (a separate pumped section consisting of a valve, a turbo pump, a magnet arm and a pressure gauge) (see Fig. 5.6 middle-left) into the main chamber. It allows for changing samples without breaking the main vacuum making it much faster to change samples during a beamtime.

Inside the main chamber a second magnetic linear-rotational feedthrough with a specially designed screwdriver head (see Fig. 5.7a) is used to fix the shuttle on the sample holder in the following way. The shuttle is taken out of the garage using the M3 thread on the side of the shuttle and slid sideways into the sample holder (the right part of Fig. 5.7c). The shuttle is locked in place with four screws from the back side (see Fig. 5.7d). With a fifth screw in the center of the sample holder one is able to rotate the sample in the sample mount by 360° about its azimuth without the need to break the vacuum. The exact azimuthal angle can be read from a Vernier scale on the sample mount and sample copper disk with an accuracy of 0.5°.

5.3.3. Sample cooling

The sample holder is thermally attached to a LHe flow cryostat (type ST-400 manufactured by Janis/Cryophysics) allowing temperatures in the range of 16-320 K without an extra cold shield. Typically a sapphire plate is placed between the cold

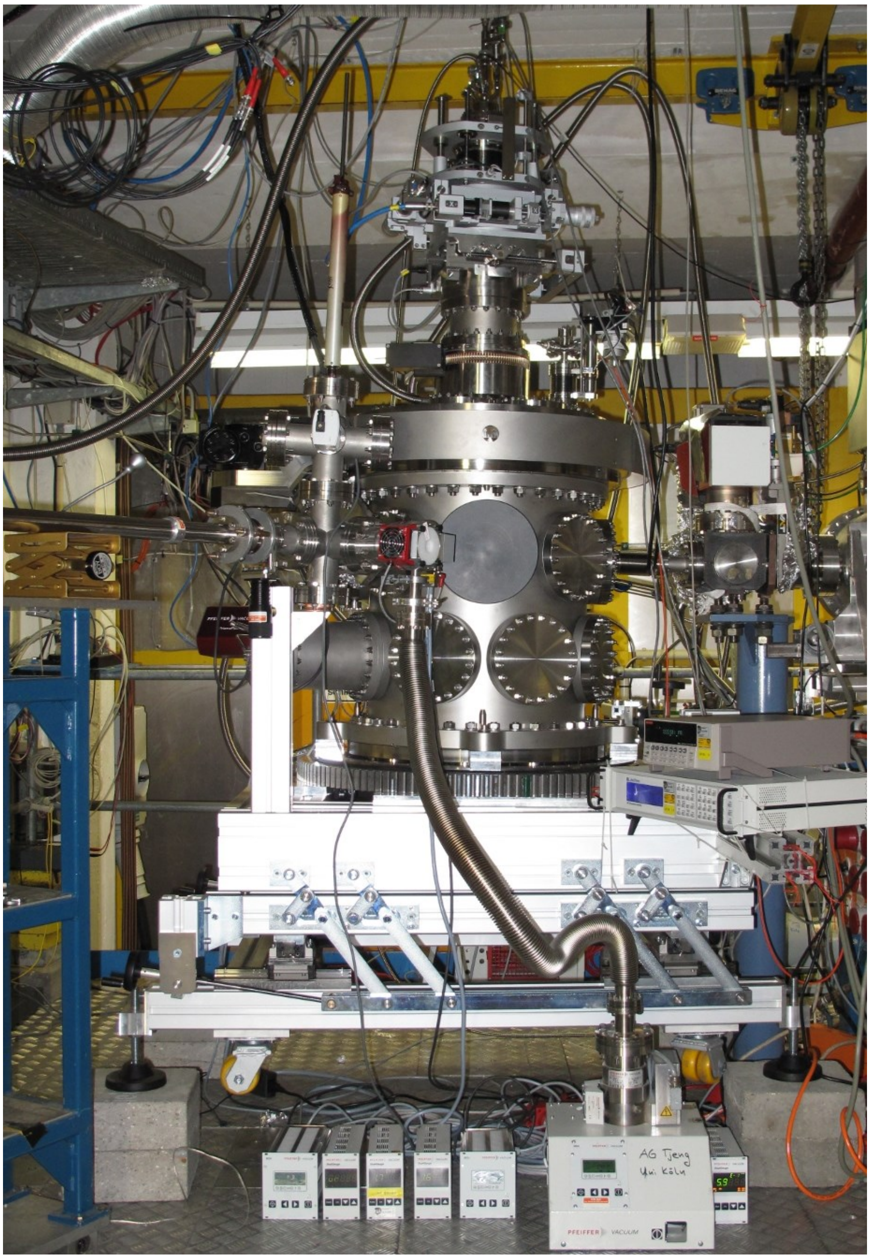

Figure 5.6.: Experimental chamber during its first operation at the DORIS III storage ring at DESY, Hamburg. Photo: M. Buchholz.

(a) Screwdriver

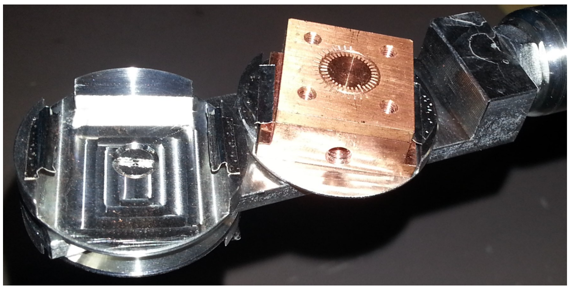

(b) Sample garage

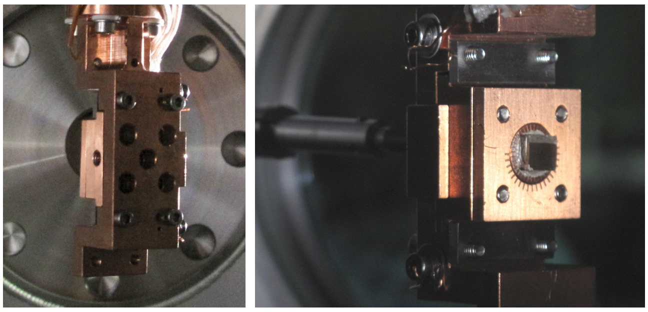

(c) Sampleholder side view.

(d) Sampleholder front view.

Figure 5.7.: Transfersystem in the new diffraction chamber. Panel (a) shows the special screw driver head. Panel (b) shows the sample garage. It consists of two (three) rotatable slides. Panel (c) shows a side view on the sample holder. Panel (d) shows the final step of a sample transfer. The screw driver tightens the sample mount to the sample holder from the back side.

head of the cryostat and the copper sample holder to provide thermal conductivity but electrical insulation. The latter is important to measure the drain current in absorption measurements. The temperatures at and in the cryostat are measured with silicon DT-670 diodes which are mounted inside the cold head and close to the sample.

For the measurements on EuTe, where temperatures < 6 K had to be achieved, the usually used transfer sample holder was replaced by a special version (see Fig. 5.8) with an extra cold shield and without sample transfer. In this setup the sample holder is directly mounted to the cold head of the cryostat and the samples are glued with silver paint directly on the sample holder. With the use of a cooling shield (see Fig. 5.8b) temperatures down to 4 K can be realized. The cooling shield which screens the cryo-cooled sample from thermal radiation is connected to a second cooling stage on the cryostat. Only slits are left for the laser and x-ray beams. The analysis tools mounted at the bottom of the cooling shield (Fig. 5.8c) are essential for time-resolved experiments. With the help of two knife-edges the sizes of the laser and x-ray beams can be determined and adjusted if needed. The YAG/phosphor is used for alignments of the spatial overlap of the two beams. The SiN-membran is used for cross-correlation measurements at the FEL between optical laser and x-ray pulses for determination of time zero and the temporal resolution as a reference. Here the effect that x-rays change the optical reflectivity of a semiconducting membrane is detected with the pump laser beam (see, e.g., Ref. [90]).

5.3.4. Coherent assembly

In Fig. 5.9 an alternative sample stage of the new chamber is shown. It shares the same sample holder design with the one described before, but employs a different type of manipulation. This ultra stiff sample support was designed and built in collaboration with the University of Amsterdam in order to minimize sample vibration and thermal drift of the sample position. The x-y manipulation is done with in-vacuum piezo actuators (PP30) with a repeatability in the low μm range. Connected to it is a pinhole tube mounted on two additional piezo stages. This setup was developed for coherent diffraction experiments in the soft and hard x-ray regime at BESSY II, PETRA III (P10) and LCLS (CXS), which are, however, not reported in this thesis.

5.3.5. Detection

Each of the detectors in the scattering instrument are mounted on variable height linear stages on one of the six CF100 flanges on the rotatable CF500 top flange in the described vacuum vessel. For time integrating (non time-resolved) diffraction experiments Si-diodes are used, for ultrafast measurements we use avalanche photo diodes (APD's). Furthermore the instrument allows for mounting an in-vacuum rotatable CCD camera (mounting designed by M. Buchholz) and a polarization

(a) Samples on Cu-holder

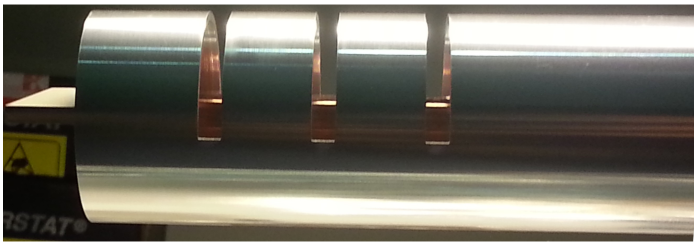

(b) Sample holder covered by the cooling shield

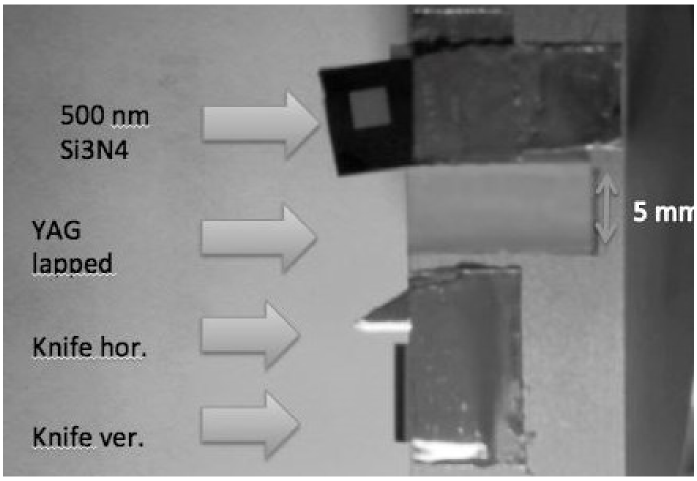

(c) Analysis tools

Figure 5.8.: Low temperature sample holder with cooling shield for temperatures down to 4 K. The cryostat is on the right hand side. The sample holder is made of copper with the samples glued in three levels (a). The cooling shield has slits for the incident and diffracted x-ray and optical laser beam (b). At the bottom of the cooling shield is additional space for diagnostic tools like SiN-membran/YAG/phosphor/knife-edges (c).

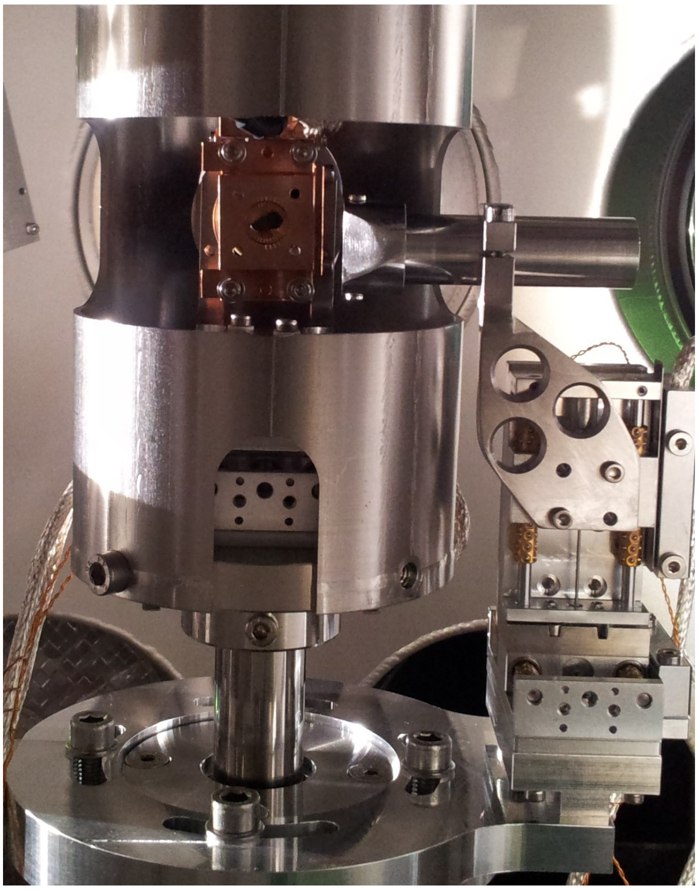

Figure 5.9.: Sample environment for coherent scattering experiments. The sample is mounted on the copper sample holder in the center of a support tube. The sample holder is mounted on a special holder which minimizes vibration and thermal drift. Thermal contact to the cryostat is achieved indirectly through a copper braid. The support tube from the top is kept centered and guided by a rod in an additional support tube on the bottom. The structure at the right carries a pinhole.

analysis detector (my design described in the Appendix A.1.1). In Fig. 5.10 our APD's and Si diodes are shown as used in an experiment carried out in October 2012 at FLASH. In principle all of the mentioned detectors can be mounted at the same time. Whenever they are needed, they are vertically moved into the diffraction plane from their parking position above beam level.

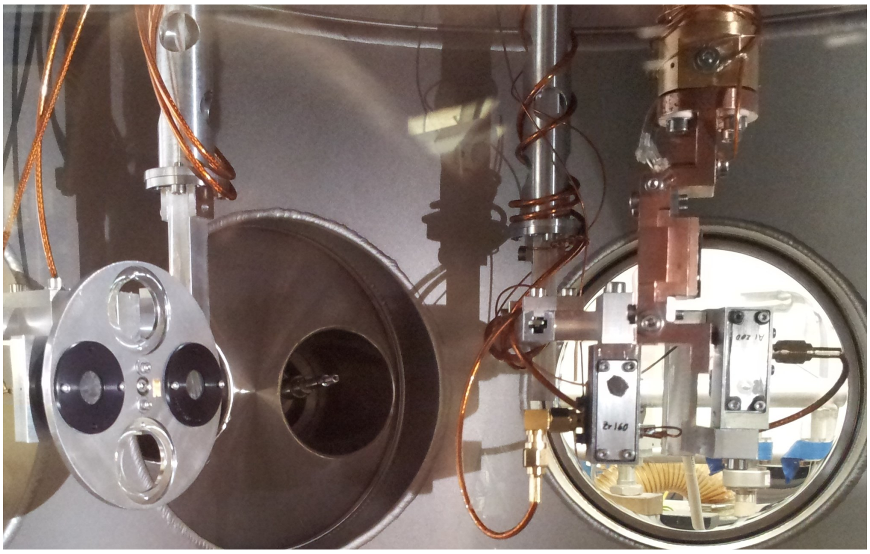

Figure 5.10.: Our detectors used during a FLASH beamtime. The two on the right side are APD detectors. The two on the left are fast SI-diodes sitting behind a filter wheel. On the filter wheel as well as in front of the APD thin metal films (Al and Zr) are mounted to protect the detector from unwanted light and as energy filters.

5.3.6. Magnet

For XMCD measurements in reflection geometry a simple and flexible electromagnet was built for switching the sample magnetization. Figure 5.11 shows this magnet during one of the slicing beamtimes. It is a yoke made of soft-iron with a coil of a long capton isolated copper wire. The yoke guides the magnetic field through the sample. The poles have an opening slit in the scattering plane towards the scattering direction allowing for all scattering angles from 0 - 90°. The maximum magnetic field is about 120 mT at a current of about 3 A. The magnet was powered by a Kepco voltage source and software controlled via SPEC. The magnet is mounted on a rotary and x-y-z translation feedthrough in the center of the bottom flange.

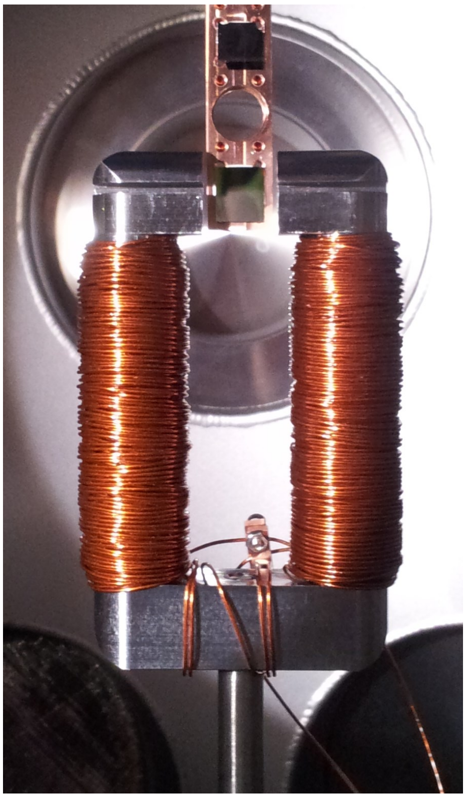

Figure 5.11.: Magnet yoke for measurements of the reflectivity depending on a variable magnetization. The width between the pole-shoes matches to the copper sample holder attached to the cryostat.

Chapter 6.

Speed limit of the insulator-to-metal transition in magnetite

The oldest known magnetic material is magnetite (Fe_3O_4). It has been fascinating mankind for millennia. As the first transition metal oxide in which a relationship between electrical conductivity and localized electronic order was shown [91], magnetite represents a model system for understanding correlated oxides in general. Nevertheless, the exact mechanism of the insulator-metal, or Verwey-, transition has long remained inaccessible [92–99].

At room temperature magnetite crystallizes in the cubic inverse spinel structure with $1/3$ of the Fe-sites on the tetrahedrally coordinated, so-called A-sites, and $2/3$ on octahedrally coordinated B-sites. Upon cooling below $T_V = 123$ K, magnetite undergoes a structural 1st order phase transition into a monoclinic phase whereupon the resistivity increases by almost two orders of magnitude [91]. The formal valence on the B-sites is 2.5+. Already Verwey suggested that localization of charge on the B-sites into an ordered pattern of 2+ and 3+ ions causes this resistivity rise. Attempts to determine the detailed character of the low-temperature phase have been ongoing since then. Recently, three-Fe-site lattice distortions called trimerons were identified as the characteristic building blocks of the low-temperature insulating electronically ordered phase [100, 101]. That means that a shortening of some distances between iron atoms leads to the distribution of localized electrons over three iron sites. Furthermore orbital order was identified as a feature of the low-temperature phase [102], the character of which, however, has remained a matter of debate [103–105].

We were interested in finding out, how fast magnetite can be driven through the Verwey transition with an external stimulus like a laser pulse in particular in hindsight of future applications of metal-insulator transitions for oxide electronics. Since both, electronic and structural degrees of freedom, are involved in the transition, it is of general interest, whether their dynamics can be separated in a non-equilibrium transition. We therefore investigated the Verwey transition with pump-probe x-ray diffraction [87] and optical reflectivity techniques [106, 107]. We found the insulator-metal transition to be a two-step process. After an initial 300 femtosecond destruction of local order, i.e., of individual trimerons, phase separation occurs on a (1.5 ± 0.2) picosecond timescale to yield residual insulating and metallic regions. This work establishes the speed limit for switching in future oxide electronics in the ps range [108]. In many oxide materials [109, 110] the insulator-metal transition has been discussed in terms of freezing fluctuating lattice and electronic (charge, spin and orbital) order, sometimes in combination with the occurrence of phase separation [111, 112]. However, due to the many competing degrees of freedom, the close energetic proximity of the different phases often obscures the exact nature of these phase transitions [113]. In magnetite, the Verwey transition does not involve changes in the spin ordering, allowing a focus purely on the role of the lattice and electronic ordering. As such magnetite serves as a model system to understand the mechanism behind the insulator-metal transition for a large group of materials.

The primary order parameters of the magnetite cubic-to-monoclinic lattice distortion are the cubic X and Δ phonon modes. These modes are strongly coupled with (001) and (110) lattice reflections[1] (see Fig. 6.3). We used single crystalline magnetite samples whose resistivity displayed the typical 100-fold change upon crossing the Verwey transition (T_V) at 123 K. The single crystals were grown using a cold crucible Bridgman technique [114]. The oxygen partial pressure was controlled to achieve the desired iron/oxide ratio. The narrow width of the Verwey transition temperature indicates that the samples are homogeneous, with few metallic impurities and nearly ideal oxygen stoichiometry [115]. The samples were first characterized at beam line UE52-SGM of BESSY II.

The samples were cleaved in air with a knife edge prior to insertion into the diffractometer vacuum. This resulted in identical resonant scattering patterns as the ones observed from in-vacuum cleaved samples [116]. The lattice transformation from the high-temperature conducting phase to the low-temperature insulating gives rise to Bragg peaks that are forbidden above T_V. In particular, we probed the low-temperature lattice order via the (001) and (110) Bragg reflections non-resonantly at x-ray photon energies of 800 eV and 1200 eV, respectively, and the electronic order via the ($00{}^1\!/\!_2$) superstructure Bragg peak. The latter is visible only with the photon energy tuned to the optical $2p$-$3d$ transition of Fe ions [102] and the $1s$-$2p$ transition of O ions [87, 117]. At the Fe resonance, we are directly sensitive to the orbital order of the Fe sites [102, 104, 105, 117] while at the O-K resonance we are probing the spatial modulation of the hybridization between O-$2p$ and Fe-$3d$ states, which is affected by orbital and charge order [87]. Equilibrium soft x-ray diffraction data showed the Verwey temperature to be 123.3 K with a hysteresis of 0.4 K and a width of the transition of less than 20 mK.

Time-resolved resonant soft x-ray diffraction measurements were carried out at the SXR beamline [118] of the Linac Coherent Light Source (LCLS), using monochromatized x-rays of 10 fs pulse duration with a repetition rate of 60 Hz and a bandwidth of 400 meV at the Fe L_3 edge (707 eV photon energy). A pump-laser with photon energy $h\nu = 1.55$ eV and 70 fs pulse duration was synchronized to the x-ray pulses. The scattering data were normalized to the pulse intensity on a shot-by-shot basis and corrected for jitter by the arrival time of the electron bunch of the free electron laser. The shortest measured timescale of < 300 fs is dominated by the remaining x-ray to optical pulse arrival time jitter. The x-ray and pump laser foci on the sample had diameters of 200 and 500 μm, respectively. Pump fluence values given here are depth-corrected, taking the penetration depth of the x-ray probe and the pump pulses into account, thus making diffraction data measured at different x-ray energies directly comparable. The correction factors are summarized in Table 6.1. Diffraction data were acquired using the RSXS endstation [86], equipped with a fast avalanche photodiode (integrating over the entire diffraction peak) and a two dimensional fast CCD camera both shielded from the optical pump laser by an Al window. Fig. 6.4 shows a sketch of the experimental setup. The CCD detector was used to record the data for the

---

[1] Note: cubic notation is used throughout this chapter

x-ray energy	Bragg reflection	Incidence angle θ in °	Penetration depth $\lambda_{\text{x-ray}}$ in nm	Correction factor f
Fe-L_3 (708 eV)	(00½)	31.5	9	0.92
Fe-L_3 (707 eV)	(00½)	31.5	18	0.86
O-K (529 eV)	(00½)	44.2	43	0.72
800 eV	(001)	66.0	50	0.71
1200 eV	(001)	60.5	105	0.53

Table 6.1.: Effective laser fluence calculation for measured Bragg reflections. Reported here are the scattering angle θ, the effective x-ray penetration depth $\lambda_{\text{x-ray}}$ and the total pump fluence correction factor, f (see text), for a given Bragg reflection and x-ray energy.

(00½) reflection at the Fe L_3-edge presented in Figs. 6.4 and 6.5. All other data presented were recorded using the photodiode detector. Complementary time-resolved optical reflectivity was measured by the group of F. Parmigiani in Trieste as described in Ref. [107] using an amplified Ti:sapphire laser system with ~80 fs pulse duration operating at 250 kHz. 800 nm pump and 500-800 nm probe beams were focused to spot diameters of ~110 and 90 μm, respectively. The sample was identical to the single crystal we used for the experiments at the LCLS. The optical signature of conductivity was probed in a 700 to 750 nm wavelength interval following Ref. [106].

Figure 6.1 displays the time resolved diffraction signal traces for the (00½) electronic order peak intensity as recorded at different resonances energies and those for the two structural reflections. Displayed here is the diffraction intensity spatially integrated over the entire Bragg peak by the photodiode detector. All signals show a rapid decay upon impact of the pump laser pulse. The time-derivative of the traces in the vicinity of time zero (in panel (f)) show that this fast decay (highlighted in panels (a)-(e) by the orange box) has a characteristic timescale of ~ 300 fs. This is the same for all reflections regardless whether they probe the lattice (at x-ray photon energy of 800 eV and 1200 eV) or the charge/orbital order response (x-ray photon energies in resonance with the Fe and O absorption edges). This timescale is limited by the time resolution of the experiment [83].

For low fluences the intensity recovers on a longer time scale while for higher fluences the intensity keeps decreasing. We model the observed dynamics by three terms: The Heavyside-function, Θ, represents the initial fast drop at time, $t_0 = 0$ ps, with the amplitude A. As it will turn out to be useful below, B and C are treated as follows. Parameter C scales the slow ps recovery. It is uniquely determined by only fitting the low fluence traces and such serves as a low fluence reference. For all other fits related to higher fluences C is kept fixed at this value. Parameter B accounts for

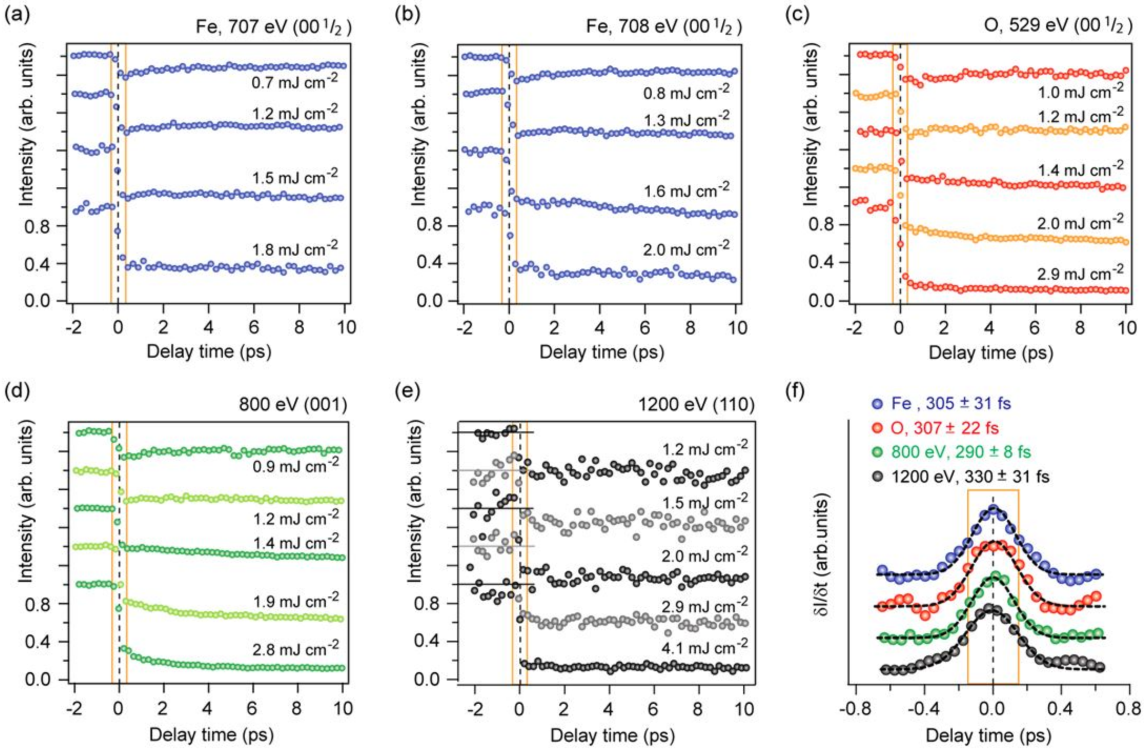

Figure 6.1.: Delay traces taken at the different Bragg reflection of magnetite. (a)-(e) The traces were taken at different fluences indicated in the plots (data were recorded at $T = 80$ K well below $T_V = 123$ K). Use of alternating colors for 529, 800 and 1200 eV photon energies are to aid visual clarity, particularly in the region of the initial ultrafast intensity quench (orange outline). (f) Representative time-derivative spectra around time zero for each of the reflections in panels (a)-(e). For these curves, a finer time-binning of the raw LCLS data of 50 fs per data point has been used, rather than the 200 fs per point binning used for Fig. 6.1 (a)-(e). Due to very small intensity of the signal in (e) the derivative in (f) is shown for the average of the curves displayed in panel (e). For all time-derivatives the initial, ultrafast quench of the low-temperature order is equally fast and occurs on a timescale faster than the experimental time-resolution of 300 fs (marked as an orange box).

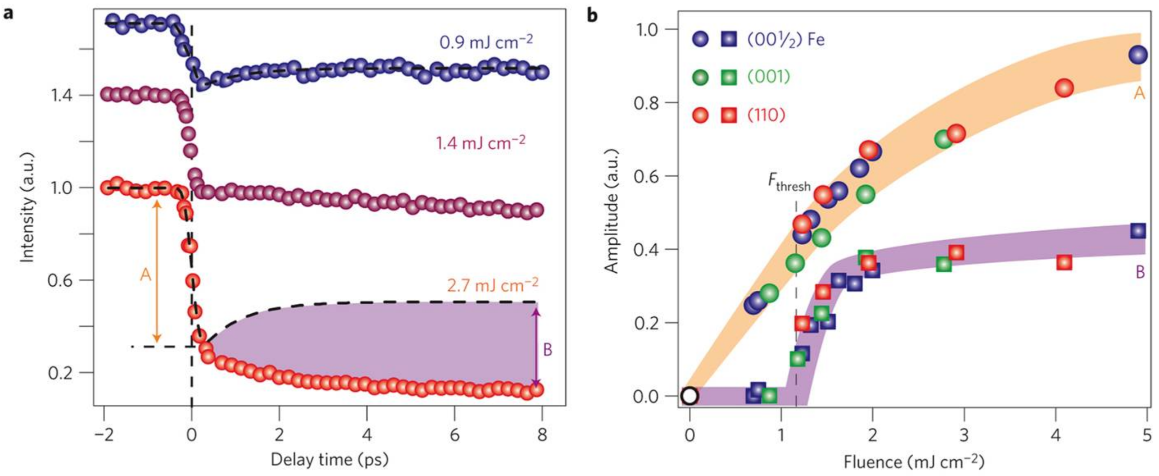

Figure 6.2.: Femtosecond and picosecond responses for a series of fluences at two different sample base temperatures (30 K and 80 K) (a) Normalized (001) diffraction intensity versus time delay for pump fluence values as indicated (traces are offset). The dashed line fits represents the characteristic timescales for pump fluences below (1.3 ± 0.1) mJ cm^{-2}. The orange arrow indicates the amplitude (A) of the diffraction from the ordered lattice in the first 300 fs. For longer delays and pump fluences above (1.3 ± 0.1) mJ cm^{-2} the signal decays monotonically (purple shading). (b) Pump fluence dependence of the fast ($t < 300$ fs) intensity drop amplitude A and the slower intensity decay amplitude B of the diffraction intensity fitted at all usable traces as those shown in (a). The fast quench (A) is present for all fluences. The slower B decay appears only above a threshold of $F_{\mathrm{thresh}} = (1.3 \pm 0.1)$ mJ cm^{-2}.

the slow picosecond decay and is determined individually for each fluence. With C fixed by the low fluence traces, B directly indicates the changes of the ps dynamics with respect to the low fluence dynamics. The final fitting function is obtained by convolving equation 6.1 by a Gaussian function, representing the experimental time resolution. The treatment of the fitting parameters A, B, and C is illustrated in Fig. 6.2.

$$I(t) = I_0 \cdot \left(1 - \left[A \cdot \Theta - C \cdot \left(1 - e^{(t_0 - t)/\tau_{\text{ref}}}\right) + B \cdot \left(1 - e^{(t_0 - t)/\tau}\right)\right]\right). \tag{6.1}$$

Figure 6.1 shows a rather unique dynamics for all Bragg reflections: The fast step (A) is present for all fluences. The slower B decay appears only above a threshold pump fluence $F_{\text{thresh}} = (1.3 \pm 0.1)$ mJ cm^{-2} for $T = 80$ K (see Fig. 6.2b). Moreover the threshold value depends on the base temperature. This can be seen in Fig. 6.3a) which shows time traces of the (001) reflection at a sample base temperature of 30 K and the fitting results of A and B. Compared to the 80 K data, the A amplitude is reduced and the B process threshold is shifted to higher fluences with $F_{\text{thresh}} = (2.0 \pm 0.1)$ mJ cm^{-2} (see Fig. 6.3 (c)).

We can compare this value to the energy required to drive magnetite across the Verwey transition in thermodynamic equilibrium. This energy, Q, can be calculated using the thermodynamic relation

$$Q = \int_{T_{\text{i}}}^{123\text{K}} C_{\text{p}}(T) dT, \tag{6.2}$$

where C_{p} is the temperature dependent heat capacity. The calculated energy also takes into account the latent heat of the Verwey transition at $T_{\text{V}} = 123$ K, $Q_{\text{L}} = 14.1$ J cm^{-3}. The heat capacity data as well as latent heat value were taken from Ref. [119]. The corresponding laser fluence value to deposit that energy in magnetite by the pump laser is then calculated to be 0.8 mJ cm^{-2} for $T_{\text{i}} = 80$ K and 1.7 mJ cm^{-2} for $T_{\text{i}} = 30$ K. The good agreement between this estimates and the experimental data suggest that the B threshold is defined by the energy needed to heat the system above T_{V}. We note that for simplicity we assume constant laser intensity in the sample (or equivalently a sample that is much thinner than the effective penetration depth of the optical laser, $\lambda \propto 110$ nm [120, 121]). This calculated value is a lower bound estimate since it does not consider heat transport and the temperature gradient present inside the sample due to the continuous cryogenic cooling.

We note that close to the threshold the data in Figs. 6.1 and 6.3 display a superposition of both, the ps recovery dynamics, leading to an initial increase of diffraction intensity, and a proceeding quenching of the signal at longer delay times. The most striking result revealed by Figs. 6.2b) and 6.3b) and c) is that all data from the different reflections can be merged into one universal plot showing clearly

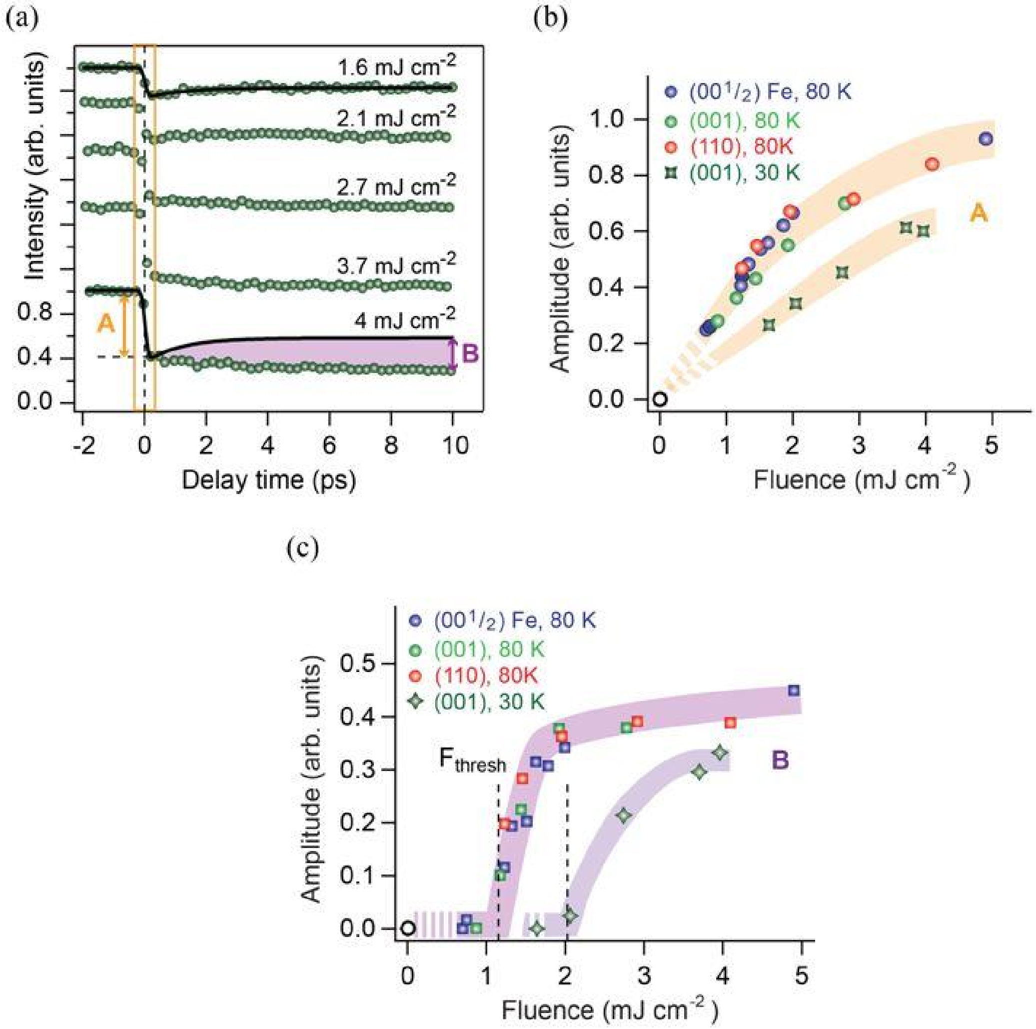

Figure 6.3.: Femtosecond and picosecond responses for a series of fluences at two different sample base temperatures (30 K and 80 K) (a) Resonant x-ray scattering intensity versus delay time for the (001) Bragg reflection at 800 eV at $T = 30$ K at effective pump laser fluence values as indicated. The black line fit extracts the timescale for the pump fluence of 1.6 mJ cm^{-2}. The amplitude A quantifies the signal drop of the diffraction intensity within first 300 fs. For longer delays and above the (1.3 ± 0.1) mJ cm^{-2} threshold fluence the signal decays monotonically, which is characterized by the amplitude B , with respect to the low fluence behavior (purple shading). (b) and (c) reveal different characteristics of A and B, respectively, for the two base temperatures. The fast quench (A) is present for all fluences. The slower B decay appears only above a threshold pump fluence $F_{\mathrm{thresh}} = 1.3 \pm 0.1$ mJ cm^{-2} for $T = 80$ K, and $F_{\mathrm{thresh}} = (2.0 \pm 0.1)$ mJ cm^{-2} for $T = 30$ K.

the intimate coupling of electronic and structural degrees of freedom in this material. This evidence suggests one of the central results of this study that within the first ~ 100 fs the optical excitation locally destroys the low temperature order launching a strongly coupled charge lattice motion.

Now we address the question what happens on longer length scales. Beyond the integrated intensity of the individual reflection further experimental evidence can be derived from the momentum resolved dynamics of the (00½) reflection (see Fig. 6.4). In Fig. 6.5 we show the evolution of the coherence length, λ_{coh}, extracted from the diffraction peak width ($\lambda_{\text{coh}} = 2\pi/w$ with w being the FWHM of the diffraction data shown in Fig. 6.4b.) and the change in the monoclinic tilt angle, $\Delta\beta$ extracted from the peak position. A comparison with the relative diffraction intensity dynamics in Fig 6.5(a) (dashed brown line) reveals that shift and broadening of the (00½) occur both equally with a significant relative delay: λ_{coh} and $\Delta\beta$ remain unchanged until ~ 200 fs after time zero. We interpret these dynamics by the initiated structural modifications of the lattice towards the cubic symmetry (Fig. 6.4 c) where metallic charge fluctuations reduce the coherence of the remnant patches of electronic order. The coherence length is reduced by up to 40%.

For the pump fluence that induces the $\Delta\beta$ change resulting in a shift of the diffraction peak as shown in Fig. 6.4 a), b), the relative diffraction intensity (dashed brown line in Fig. 6.5) is strongly suppressed within 300 fs of the optical excitation pulse. In contrast to the fast intensity quench, the changes of $\Delta\beta$ and λ_{coh} display a different characteristic timescale of (1.5 ± 0.2) ps for this pump fluence. Since changes of $\Delta\beta$ and λ_{coh} set in only for delays larger than 200 fs (the earliest data point following optical excitation included in Fig. 6.5), on the timescale of the ultrafast intensity quench, the low-temperature monoclinic lattice tilt angle and the coherence length remain unchanged. This means obviously, generating holes in the trimeron lattice weakens the network, but does not destroy its long-range order. This behavior of negligible change in correlation length despite a strong reduction of diffraction intensity has also been observed in nickelates [2], where it has been associated with small fluctuations in amplitude and phase of charge order, as well as in ruthenates [122] with a static random pattern of magnetically ordered regions.

With delays around 1 ps a transformational regime is entered that is marked by a break-up of the trimeron lattice into patches separated by a coexisting metallic phase which scrambles the phase coherence of the surviving trimerons islands (see Fig. 6.8). This is accompanied by a relaxation of the monoclinic lattice tilt $\Delta\beta$ in the trimeron islands towards the right-angle cubic value (see schematics in Fig. 6.4). After 5 ps (compare Fig. 6.5), the deviation from the cubic lattice angle is 0.11° compared to 0.23° for the static low-temperature case. One of the most remarkable aspects of the data of Fig. 6.5 is that the lattice transformation towards the cubic ideal does not happen synchronously with the ultrafast trimeron annihilation process. The transformational regime is entered only at pump fluences above the threshold value, since both λ_{coh} and the monoclinic tilt change only above (1.3 ± 0.1) mJ cm^{-2} (left

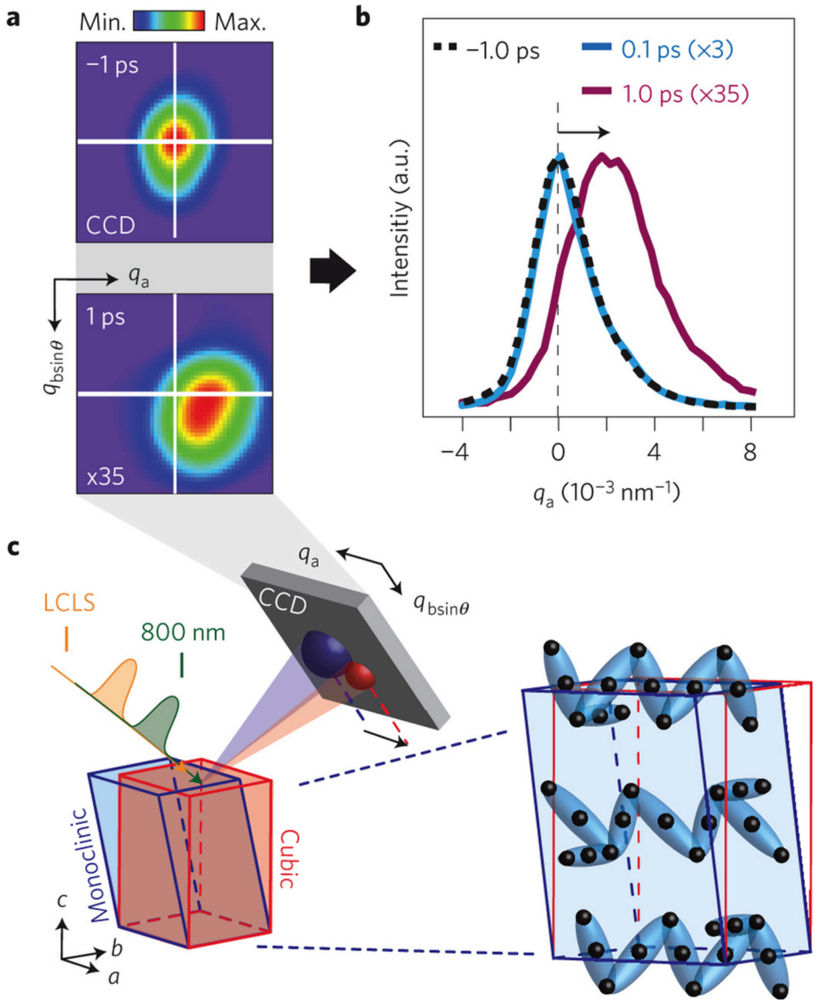

Figure 6.4.: Response of the soft x-ray diffraction intensity from the monoclinic reflections of the low temperature phase of Fe_3O_4 upon optical pumping. (a) CCD detector images of the ($00^1/_2$) electronic order recorded at the Fe L_3-edge before and after pumping with 4.9 mJ cm^{-2}. The pump-induced shift of the diffraction peak shows a clear in-plane component along q_a while the orthogonal direction is a superposition of in-plane (q_a) and out-of-plane (q_c) directions. (b) Horizontal line-scans of the ($00^1/_2$) peak at q_b = 0 before 0 fs, at 0.1 ps and at 1 ps pump-probe delay time. (c) Sketch of the experimental setup. The magnetite crystal is shown as the blue (red) block in the monoclinic (cubic) structure. Inset: Low temperature unit cell with the electronically ordered trimeron lattice represented using blue ellipsoids after Ref. [100].

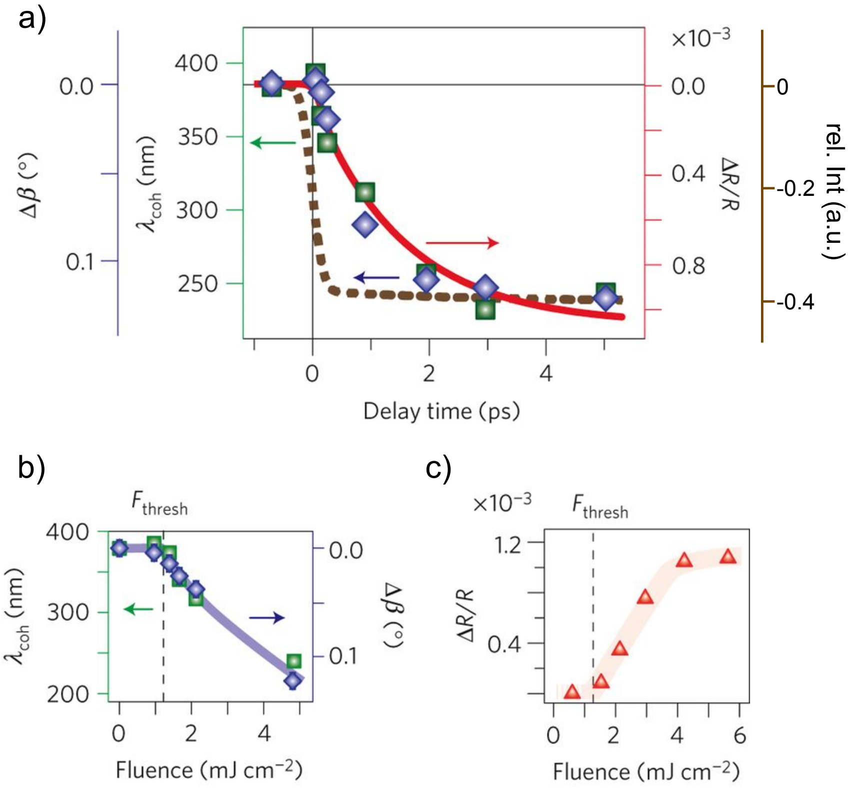

Figure 6.5.: Comparison of optical data with the data from the RSXD: a) Fast trimeron lattice quench followed by a ps transformational process. The figure compares x-ray data (blue/green symbols and dashed brown line) taken at the $(00{}^{1}/_{2})$ reflection (Fe L_3-edge) and optical reflectivity (red line, representing an exponential fit to the data). Statistical errors in determining λ_{coh} and the change in monoclinic tilt angle, $\Delta\beta$, are given by the respective symbol sizes. As a comparison from Fig. 6.1: diffraction intensity versus time (dashed brown solid line in arbitrary units). b) Fluence dependent λ_{coh} and $\Delta\beta$ data taken at a fixed delay time of 5 ps. The data show a threshold fluence, $F_{\mathrm{thres}} = (1.3 \pm 0.1)$ mJ cm^{-2}, above which the diffraction peaks display a change of the monoclinic angle $\Delta\beta$ (0.23° would correspond to the cubic case). c): Fluence dependent $\Delta R/R$ data taken at a fixed delay time of 5 ps, probing the onset of the metallic phase which sets in for fluences above (1.3 ± 0.1) mJ cm^{-2}.

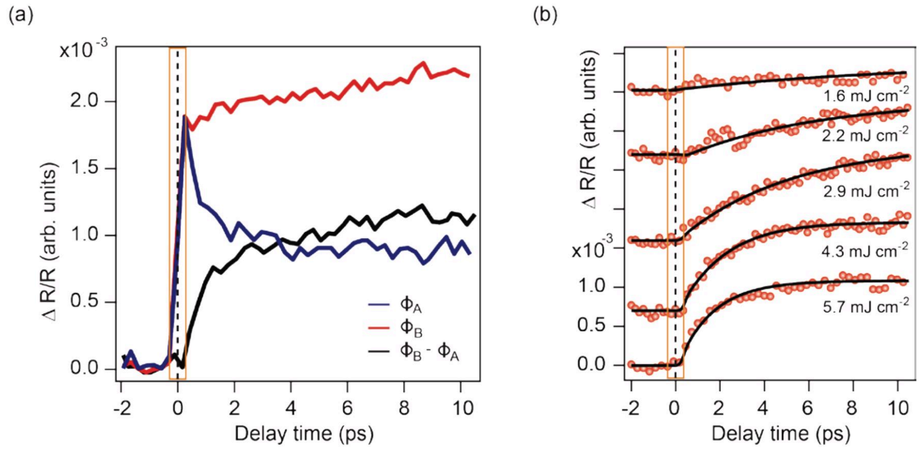

Figure 6.6.: Reflectivity measurements at 80 K with optical pump and probe, $\Delta R/R$ versus delay time data normalized to the probe fluence, ϕ, for magnetite, Fe_3O_4. The data were obtained by integrating the optical reflectivity probe between 700 and 750 nm wavelength. (a) Comparison of delay traces obtained at fluences of $\phi_A = 0.6$ mJ cm^{-2} (blue line) and $\phi_B = 5.7$ mJ cm^{-2} (red line). The difference (black line) shows the ps evolution of sample conductivity related to the insulator-metal transition. (b) Fluence dependence of the ps evolution of the sample conductivity (symbols). The solid lines are fits of equation 6.3 to the data.

inset to Fig. 6.5), in agreement with the minimal fluence for metallic character seen in the optical reflectivity (right inset to Fig. 6.5).

The observed reduced correlation length of the insulating trimeron lattice indicates phase separation into coexisting metallic and insulating regions. In order to characterize this process further, we used optical reflectivity. In thermal equilibrium, optical conductivity measurements on magnetite have identified certain spectral regions which can be taken as a fingerprint for the insulator-metal transition [123] between 700 - 750 nm wavelength Park et al. [106] observed an increase in optical reflectivity above the Verwey temperature. Time-resolved optical reflectivity was measured in this region as described in Refs. [99, 107]. Figure 6.6 shows the optical reflectivity (ΔR/R) measurements as a function of delay time using a broadband pump pulse (central wavelength of 795 nm), probing reflected intensity between 700 and 750 nm wavelength. In order to extract relevant timescales the data measured at different fluence values are normalized by the respective laser probe fluence as shown in Fig. 6.6(a). The observed fast rise in reflectivity within first 300 fs is identical for all measured fluence values. Therefore the data in Fig. 6.6(b) represent the difference of the fluence dependent delay traces and the low-fluence delay trace (demonstrated in Fig. 6.6(a)) to extract the monotonic increase of the reflectivity on the picosecond timescale. Figure 6.5(b) shows the fluence dependence of the obtained change in ps optical reflectivity for an 80 K sample temperature. The data are fitted using an exponential of the form:

$$\Delta R/R = S(1 - e^{(t_0 - t)/\tau}). \tag{6.3}$$

The parameters for the amplitude, S, of the observed conductivity increase as well as the time constant, τ, and delayed onset, t_0, are given in Table 6.2. The fluence dependence of the amplitude, S, is shown in Fig. 6.5. The curves show a delayed onset similar to that of the changes in the coherence length and monoclinic tilt angle as determined with x-rays. The time constant fitted to the highest fluence of (1.5 ± 0.2) ps is in excellent agreement with that for λ_{coh} and $\Delta\beta$ values and shown in red in Fig. 6.5.

Fluence (mJ cm^{-2})	S (10^{-3})	τ (ps)	t_0 (ps)
1.6	0.117 ± 0.046	10 ± 2	0.24 ± 0.03
2.2	0.713 ± 0.039	5.9 ± 0.5	0.25 ± 0.03
2.9	0.976 ± 0.027	4.8 ± 0.2	0.24 ± 0.03
4.3	1.082 ± 0.022	1.6 ± 0.2	0.27 ± 0.03
5.7	1.113 ± 0.021	1.5 ± 0.2	0.26 ± 0.03

Table 6.2.: Pump fluence dependence of the fitting parameters, amplitude, S, time scale, τ, and delayed onset, t_0, for the optical reflectivity data shown in Fig. 6.6.

From the RSXD and the optical data we derive the following scenario where dynamics occur in two different regimes:
(i) The fast process A, with a characteristic time scale $\tau < 300$ fs. Individual trimeron sites are 'knocked-out' through optically induced electronic transitions, followed by a rapid equilibration of the electronic channel. During this process, the diffraction intensity is lowered because the number of scatterers in the pump-probe volume is reduced. However, the long range order of the Verwey phase is retained as shown by the fact that the observed coherence length does not change, see Fig. 6.5. In a diffraction experiment, the diffraction peak height is proportional to the squared number of contributing scatterers or the ordered volume fraction, V, squared, while the integrated peak intensity is directly proportional to that number. In our case of a finite detector acceptance we are somewhere in between these extrema. For simplicity we assume the quadratic relationship $I \sim V^2$. This enables us to roughly estimate the volume fraction of the residual low-temperature phase within 300 fs after the excitation. The analysis is presented in Fig. 6.7 (gray symbols and shading), where the measured amplitude of the A process (Fig. 6.2b) is used to calculate this volume fraction as a function of pump laser fluence. The extent to which order is annihilated by the pump photons can be estimated from the slope of the residual volume fraction versus laser fluence, yielding ∼ 20% per photon per unit cell, corresponding to 6 of the 30 trimerons in one single monoclinic cell. This value is in close correspondence with

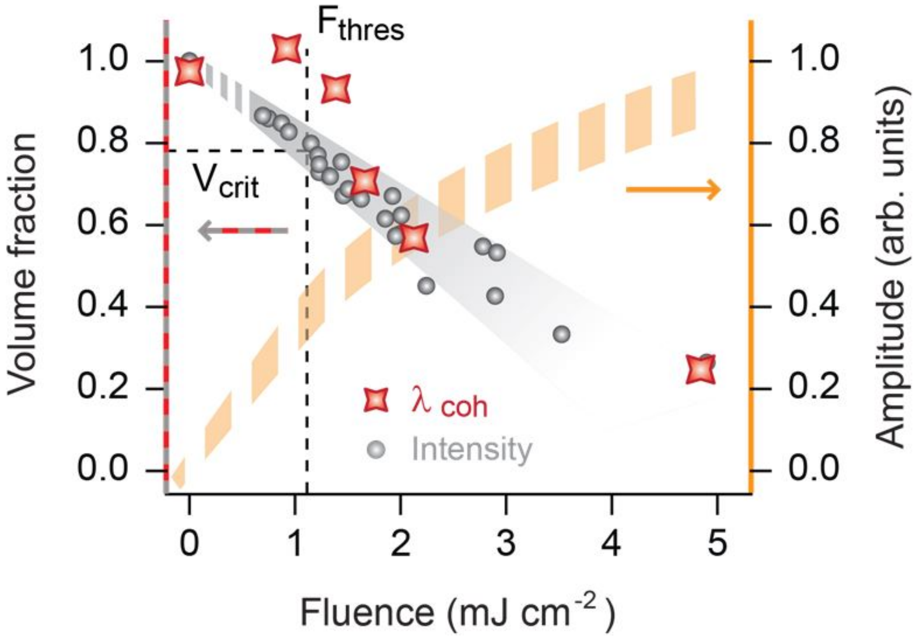

Figure 6.7.: Grey symbols and left axis: Relative low-temperature phase volume fraction, V, after 300 fs as a function of pump laser fluence for 80 K obtained form the amplitude, I_A, of the A process (Fig. 6.5) via $I_A \sim V^2$ as described in the text. The fluence dependence of I_A is shown as orange shading and right axis as reference. Red symbols and left axis: Relative trimeron volume fraction after 5 ps calculated from the relative decrease in coherence length (inset of Fig. 6.5). The laser fluence threshold value, $F_{\text{thresh}} = (1.0 \pm 0.15)$ mJ cm^{-2}, and the associated critical volume fraction ($V_{\text{crit}} = 0.78 \ \pm \ 0.05$) are indicated.

the 5-10 excitations possible above the band gap (reported to be between 150 meV [99] and 300 meV [110]) per 1.55 eV photon.

(ii) The slower process B, with a characteristic time scale $\tau \sim 1.5$ ps. Further heat dissipation from the electronic channel and hot phonon bath to other modes causes the lattice to heatup. Below the threshold fluence of 1.3 mJ cm^{-2} (for 80 K), the Verwey temperature is not reached, and the trimeron lattice reasserts itself, albeit at slightly elevated temperature with respect to the state before the pump pulse. Upon exceeding the critical fluence value of 1.3 mJ cm^{-2} (for T = 80 K) driving the system across T_V. The monoclinic structure can relax toward the cubic structure and promoting charge carrier hopping. As a result, the damaged trimeron lattice rearranges into smaller ordered patches that are surrounded by regions with a dominating metallic phase. This loss of coherence of the trimeron order is observed through an increase of the diffraction peak width above threshold fluence, see Fig. 6.5.

To estimate the volume fraction of the low temperature trimeron order after the rearrangement of trimerons, the measured coherence length of the surviving ordered trimeron domains after optical pumping is compared with that in the static case. A decrease in coherence length by a factor f, leads to an estimated low temperature phase volume fraction f^{-3}. We note that this method can only be applied for pump fluence values above the critical value, since the coherence length is constant for values below 1.3 mJ cm^{-2}. The estimated volume fraction obtained, using the data from the inset of Fig. 6.5, is also displayed in Fig. 6.7 (red symbols). Figure 6.7 demonstrates that this estimate of the remaining trimeron volume fraction is in good correspondence with that derived for delays < 300 fs. The critical trimeron volume fraction, V_{crit}, associated with the threshold fluence value, can now be estimated to be 0.78 ± 0.05. Thus, 0.22 ± 0.05 of the sample volume would support the charge fluctuating, metallic phase at the point where the system can no longer recover to the low temperature trimeron lattice after the optical excitation within the time window of the experiment.

Bringing together all pieces of the puzzle, as shown in the cartoon in Fig. 6.8, we can now describe, step-by-step, the energy dissipation processes following fs optical excitation of the electronically ordered Fe B-sites in magnetite:

(1) On a fs timescale, the optical pump pulse induces transitions in the electronic system (red arrows in panel a) of Fig. 6.8), leading to the creation of holes in the trimeron lattice.

(2) This process, which represents trimeron annihilation (overlap area in panel a) of Fig. 6.8), triggers relaxation of the monoclinic distortions related to a subset of the frozen phonon modes, namely the ones with the largest amplitude situated on the end points of the trimerons [100, 101]. It is the frozen $X1$ and $\Delta 5$ modes that dominate the monitored diffraction peaks. The energy of these $X1$ and $\Delta 5$ modes is between 10 to 30 meV [124], yielding characteristic vibrational timescales between 400 and 150 fs. We note that possible coherent oscillations of these modes would be smeared out due to the time resolution (~ 300 fs) of our experiment.

(3) After 300 fs, the residual trimeron lattice retains the long-range order of the insulating phase (panel b) of Fig. 6.8), albeit possessing excess energy that is dissipated on a longer (ps) timescale.
(4) If the pump fluence is low, the trimeron lattice then recovers and the system simply returns to a warmer version of the electronically ordered insulating state, by equilibration of the hot phonon modes. Yet the long range coherence of all the other frozen displacement modes of the monoclinic structure is still preserved.
(5) For a pump fluence above threshold, the excess energy is sufficient to drive the system through a point of no return. The dynamics of this unfreezing depends on the starting temperature before the pump: lower temperatures requiring larger pump fluences (see Fig. 6.3) Thus, for 80 K starting temperature, the transformational regime (panel c) of Fig. 6.8 is entered on a characteristic timescale of (1.5 ± 0.2) ps. The observed relaxation of the monoclinic tilt indicates the melting of the Γ-mode distortions on this time scale. The 80 K threshold fluence of (1.3 ± 0.1) mJ cm^{-2} corresponds to the absorption of about one photon per monoclinic unit cell, containing 30 trimeron sites. A single 1.5 eV photon can create about 5-10 electron-hole pairs above the band gap [96, 106], thus the threshold fluence corresponds to the destruction of about 1 in 4 trimerons.
(6) This transformational process switches the system from being a long-range ordered trimeron lattice (blue in Fig. 6.8) with holes in it (dashed), into a patchwork of modified but still electronically ordered remnants (purple in panel c) of Fig. 6.8), with structural parameters leaning towards those of the charge fluctuating, conducting cubic matrix in which they reside (red, seen in reflectivity). This transition from the residual coherent trimeron network to a phase segregated state has to proceed via coalescence of 'trimeron-holes' and thus involves the hopping of charges together with their associated lattice distortions between trimeron lattice sites. The electronic order observed after 1.5 ps could - in principle - be a different one to that in the ground-state. However, the optical data as well as the observed reduction of the monoclinic tilt angle indicates that the 800 nm pump drives the system (partially) into the high-temperature phase. The fact that electronic order is still observed at such ps timescales clearly indicates the existence of insulating regions in the sample. Hence, the observed B process is the signature of polaronic transport, further eroding the ordered regions on a ps timescale after the optical excitation. This polaronic hopping timescale matches well with the charge density relaxation time seen in inelastic neutron scattering associated with fluctuating trimeron order above T_V [125]. These observations all point to the fact that the threshold fluence, translating to trimeron lattice collapse for a volume fraction below ~ 75 %, is that required to create a percolative network of charge-fluctuating, metallic, sites in the trimeron matrix.

This pump-induced transformation can thus be regarded as a non-equilibrium version of the thermodynamic Verwey transition. Consequently, the data show how magnetite dynamically evolves towards its energy minimum during the Verwey transition: initially holes in the long-range ordered trimeron lattice allow the trimerons to become

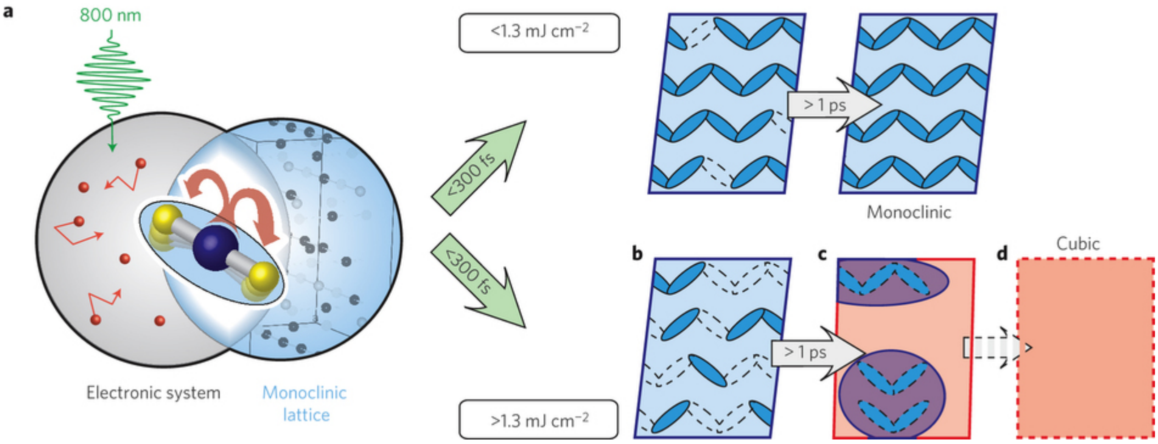

Figure 6.8.: Summary of the workings of the Verwey transition in non-equilibrium pump-probe form. (a) ultrafast trimeron annihilation due to laser excited Fe^{2+}-Fe^{3+} charge transfer launches strongly coupled electronic and lattice dynamics. For a pump fluence above (1.3 ± 0.1) mJ cm^{-2} trimeron holes (b) transform with a time constant of (1.5 ± 0.2) ps to a state with shrinking patches of remnant phase-scrambled electronic order as shown in (c). Its structure is approaching that of the cubic case, embedded in a network supporting mobile charge fluctuations (red) derived from the aggregation of the trimeron vacancies in (b). The end of the line would be the fully metallic, cubic phase (d).

mobile and form shorter-range ordered domains surrounded by charge fluctuating regions. The coalescence of the remaining trimerons, most likely driven by local strain, is connected to the organization of hundred thousands of atoms involved in the frozen displacement modes of the monoclinic structure. The bulk metallic phase is reached as soon as the charge-fluctuating regions form a percolation pathway through the magnetite crystal.

In conclusion, our experiments show that insulating, electronically ordered, low-temperature magnetite displays phase segregation on a (1.5 ± 0.2) ps timescale following ultrafast laser induced trimeron hole creation. We identify a residual low-temperature, insulating phase embedded in a phase resembling the high-temperature metallic lattice, the latter forming percolative charge-fluctuating regions throughout the sample. The switching of conductivity in such an archetypal complex oxide at the picosecond timescale clocks these systems faster than the best graphene transistors [126] developed to date. The understanding speed we have gained here as to how the transformation between the two states straddling the Verwey transition actually takes place could aid in the choice and design of oxide materials aiming at harnessing the enormous differences in electrical conductivity available in these systems.

Chapter 7.

Spectroscopic signature of pump gradients in pump-probe resonant diffraction

A strength of resonant soft x-ray diffraction beyond providing a quantitative probe of the degree of electronic or magnetic order is that it allows to do spectroscopy on the electronic states involved in the electronic (or magnetic) ordering. In a real RSXD experiment x-ray radiation propagates through a certain amount of material before and after it is diffracted at atoms close to the sample surface. Propagation through material is accompanied by absorption which in particular in the vicinity of resonances can be strongly energy dependent. Altogether this can cause absorption to considerably affect the natural shape of RSXD spectra by imposing an energy dependent intensity modulation. Understanding and separating these absorption effects from the natural shape of the RSXD spectra is essential for a correct data interpretation.

How much the contribution of an individual scatterer or a scattering plane is affected by absorption depends on how deep it is located beyond the surface: The deeper the stronger the absorption effects. Since a RSXD spectrum results from the coherent superposition of all contributing scatterers the impact of absorption effects depends on whether diffraction planes in different depths scatter equally strongly or whether there is a depth dependent scattering strength. Recent studies have demonstrated that such effects become particularly significant when a sample has a so called dead layer (i.e. a layer of non ordered material that rather contribute to absorption than to the scattering) [116].

Similar effects as a static dead layer can occur in a dynamic RSXD experiment when the sample is excited by an ultrafast laser pulse. Optical absorption leads to a depth dependent gradient of absorbed excitation energy. Supposed the quenching of electronic order directly depends on the amount of absorbed laser energy a depth dependent scattering strength according to the laser absorption profile results.

An observation made during the magnetite experiment described in the previous chapter is that the RSXD resonance spectra change upon pumping. In particular at the oxygen-K edge an apparent energy shift of the resonance towards lower energies occurred (see Fig. 7.1). This, however, is not caused by any intrinsic change of the electronic structure, e.g. a closing of the energy gap, but is a direct result of a purely optical effect due to the formation of a long-lived gradient in the density of ordered sites as will be discussed in this chapter.

The reason for this effect is the combination of a strongly energy dependent absorption across the oxygen resonance (compare Fig. 7.2a) and the laser induced depth profile of the scattering strength (quenching of electronic order). All oxygen sites absorb x-ray photons no matter if they contribute to the scattering signal or not.

A scenario with less ordered sites in the near surface region effectively reduces the relative fraction of the scatterers with small absorption effects compared to high absorption effects. The amount of this reduction is energy dependent. For a peak in the resonance of the diffraction signal that is located on an increasing slope of the absorption spectrum (as the magnetite $(00\frac{1}{2})$ peak at the oxygen-K resonance) (see Fig. 7.2a) the high-energy part of the resonance spectrum is suppressed to a larger

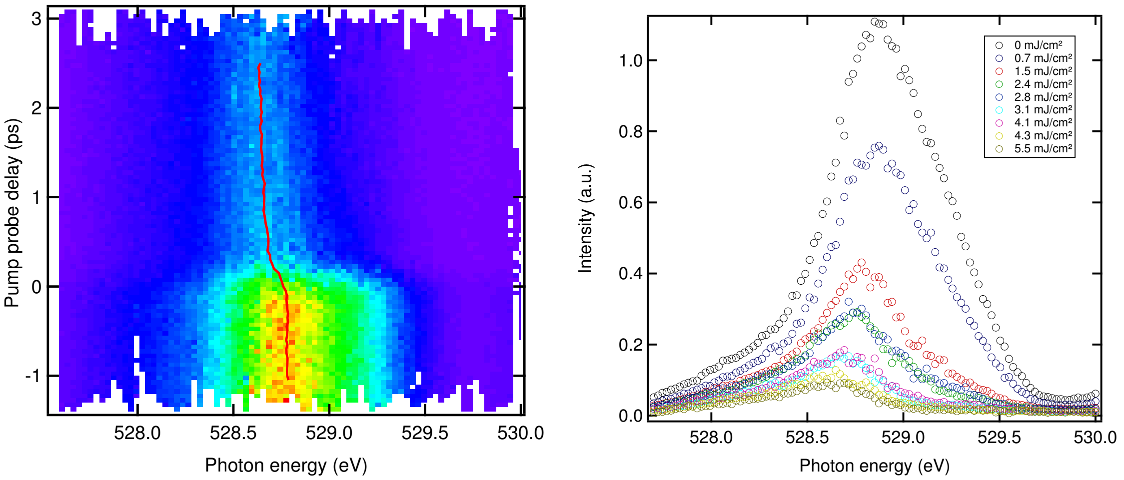

Figure 7.1.: Experimental RSXD [$(00\,^1\!/_2)$ reflection] oxygen-K spectra recorded for different delays in the left panel and for different pump fluences at a fixed delay of 1 ps in the right panel measured at the LCLS.

extent than the low-energy part leading to an apparent energy shift. Such a gradient of scatterers is built through the excitation of an optical laser on the length scales of the absorption lengths. The present experiments have shown that this gradient occurs on ultrashort timescales and can remain up to rather long timescales (ns).

Since an apparent peak shift is caused by a suppression of a part of the resonance spectrum there is a relation between peak shift and intensity loss. The fulfillment of this relation is a strong indication to interpret a peak shift rather as an absorption effect than as a pump-induced change in the electronic structure.

In order to model the pump-laser gradient induced modulation of the RSXD spectra the scattering density ρ as a function of depth z is assumed to look like

$$\rho(z) = \max(1 - \alpha\ e^{-\mu_\mathrm{l}\ ^{z}\!/_{\sin(\theta)}}, 0). \tag{7.1}$$

α is a measure for the pump fluence and μ_l the absorption length for the pump laser photons. $^{z}\!/_{\sin(\theta)}$ describes the effective photon path at an outgoing angle θ after refraction at the surface. The pump effect saturates when all scatterers have been pumped away. Refraction effects are ignored and will mostly affect the $^{z}\!/_{\sin(\theta)}$ term. For the values $\mu_\mathrm{l} = {}^{1}\!/_{1050}$ Å (calculated with values from [121]), and $\theta = 45°$ and for different values of α, profiles as in Fig. 7.3 occur. For low fluences an exponential gradient throughout the whole sample forms while for higher fluences no scatterers are left over in the top most layers.

The momentum space integrated diffracted intensity is proportional to the number of scatterers in the probed volume, n. In a perfect crystal with a photon coherence length and width comparable to the x-ray penetration depth and the transversal beam size, respectively, the diffraction peak height is proportional to the squared number

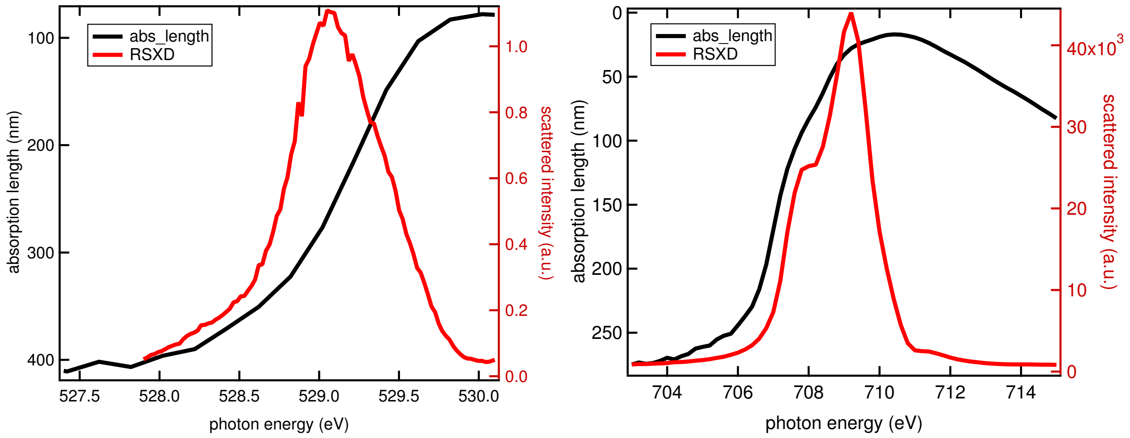

Figure 7.2.: Absorption length (black, left axis) and scattering strength (red, right axis) in the photon energy range around the oxygen-K (left panel) and around the Fe-L_3 absorption edge (right panel)

of scatterers, n^2 (and the width proportional to $1/n$ such that the integral is again proportional to n). In a realistic experiment one is not probing the whole integrated intensity and the peak height is limited by crystalline domains such that the true probed signal is somewhere in between n and n^2.
For the pumped case the effective number of scatterers in the probed volume is given by the density of scatterers $\rho(z)$ times the primary x-ray photon flux that reaches the layer z and can escape from there and both integrated over z.

$$n(h\nu) \propto \int_0^\infty \rho(z)\; e^{-2\mu_x(h\nu)\;{}^{z}\!/\!{}_{\sin(\theta)}} dz \tag{7.2}$$

$\mu_x(h\nu)$ is the x-ray absorption coefficient, $h\nu$ the x-ray photon energy. The experimental spectrum is then the 'true' resonance spectrum $I(h\nu)$ multiplied by the energy dependent $n(h\nu)$ to some power between one and two. We determine $\mu_x(h\nu)$ from an experimental absorption spectrum recorded from a transmission sample (of 42 nm thickness) of magnetite and matched to tabulated values [49] far away from resonance.

The results can be found in Fig. 7.4. Both lower panels show the magnified region of the oxygen and iron resonances. We see that the absorption length varies drastically, e.g. at the oxygen edge from 80 to about 400 nm. Since the x-ray probing depth is of the same order of magnitude as the pump laser penetration depth, it is important which photon energy is used in diffraction experiments (see Fig. 7.2). Tuned to the resonance maximum, only a few tens of nm are probed, whereas off-resonance, one probes much deeper layers. Figure 7.5 schematically shows three scenarios with dead layers of different thickness. Panel a) contains no dead layer at the surface. All incoming wavelengths are going in and leaving the sample. Going from a thin dead layer (panel b) to a thicker dead layer (panel c), the absorption of more and more

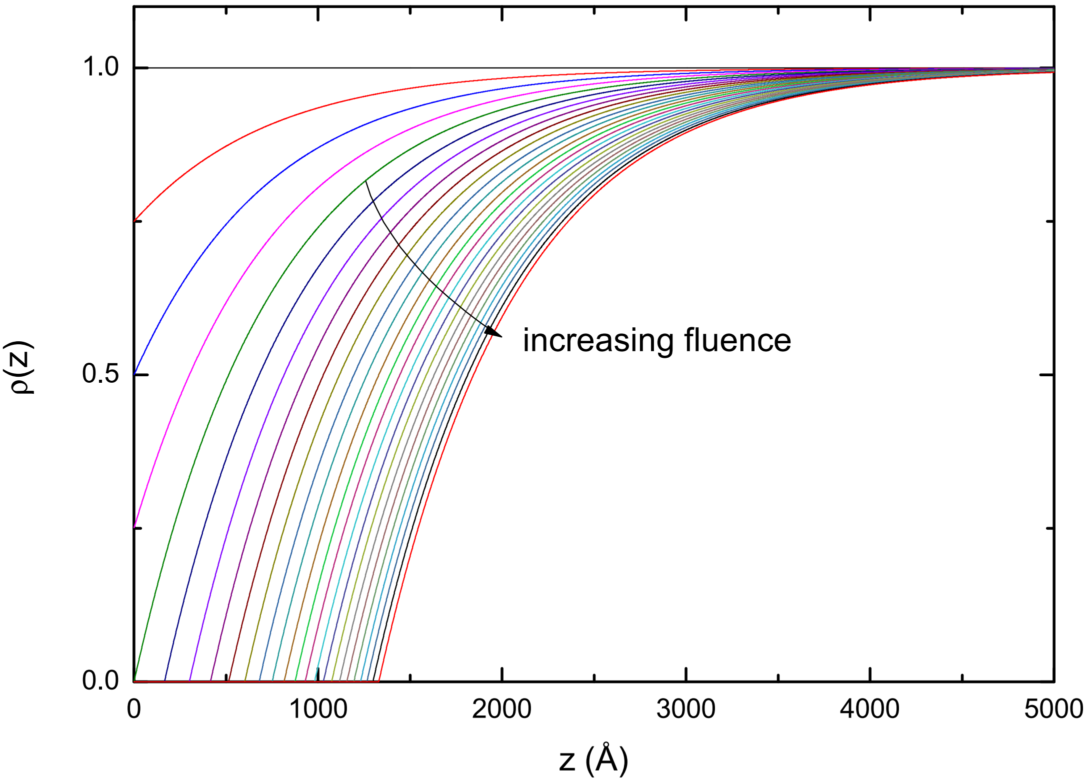

Figure 7.3.: Scattering densities $\rho(z)$ induced by the pump laser for different fluences. Parameters refer to 800 nm pump photons and the geometry for probing the $(00{}^{1}\!/\!{}_{2})$ peak at the oxygen-K resonance. The used absorption length is $\mu_{\mathrm{l}} = {}^{1}\!/\!{}_{1050}$ Å .

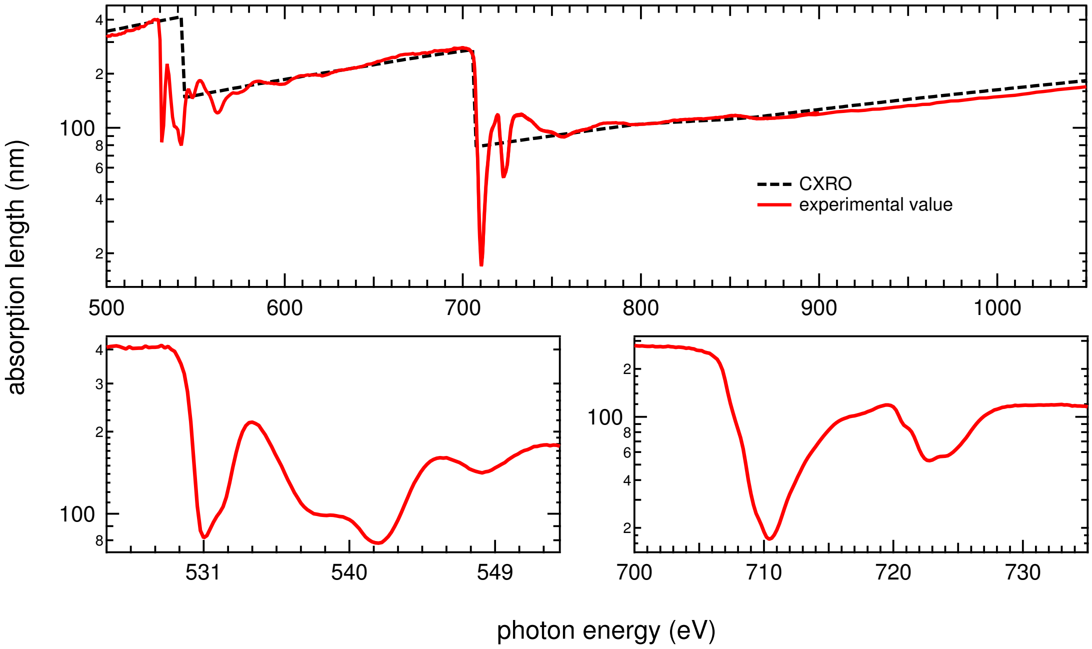

Figure 7.4.: Absorption length in the photon energy range from 500 to 1050 eV determined by XAS on a 42 nm magnetite transmission sample. The bottom left and right panels are zoomed into the regions around the Oxygen K- and Iron $L_{2/3}$ -edges, respectively.

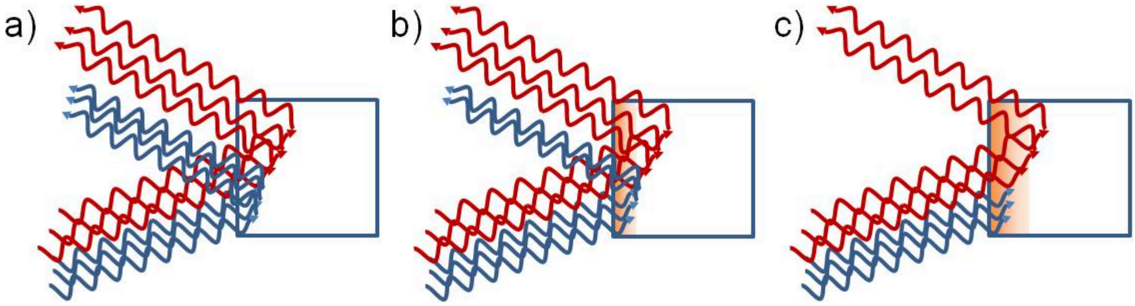

Figure 7.5.: Scheme of the absorption of different wave lengths in different probing depths. a) No dead layer, short and long wave length can penetrate in the material and can come out again. b) Small dead layer, beginning of the absorption of shorter wave length. c) thicker dead layer, mostly long wavelength are probed.

short wavelengths (higher energies) leads to a higher fraction of long wavelengths (lower energies) in the scattering signal. This results in the following findings:

Figure 7.6a) shows simulated spectra at the oxygen edge for different fluences. Based on the experimental spectrum without laser pump as the 'natural' shape of the RSXD spectrum (black) the effect of the pump gradient presented in Fig. 7.3 is simulated (lines) using the x-ray penetration depth of Fig. 7.4 and compared with the experimental data (markers). With increasing pump fluence the peak loses intensity and shifts to lower energies as seen in the experimental data. In Fig. 7.6a the simulated and the experimental spectra are compared. Figure 7.6b) shows the intensity as quantified by the energy integration (black data) and the shift of the center of mass (red data).

The experimental results are very well reproduced. The only free parameter in this model is the relation between α and the pump fluence. This was adjusted to achieve best agreement with the experimental data in the figure above. The scaling results such that $\alpha = 1$ corresponds to 2.4 mJ cm^{-2}.

Similar effects occur at the Fe L_3 edge. At the iron edge two different resonance maxima (lower energy (LE) and higher energy (HE) peak) due to the CO/OO order [102] are present. Looking at the absorption length at these energies (Fig. 7.2b)), it becomes clear, that the signal measured at the LE peak comes from deeper sample regions. Therefore one gains information about two different sample depths measuring one resonance spectrum. Figure 7.7c) shows simulated spectra for this energy range. For higher fluences the high energy peak is faster suppressed than the low-energy peak, which is again explainable via the same pump induced dead layer and the different penetration depths at the LE and HE peaks. The simulated spectra matches the experimental data from LCLS and BESSY II (Fig. 7.7a) and b)) even though slightly different fluences were needed.

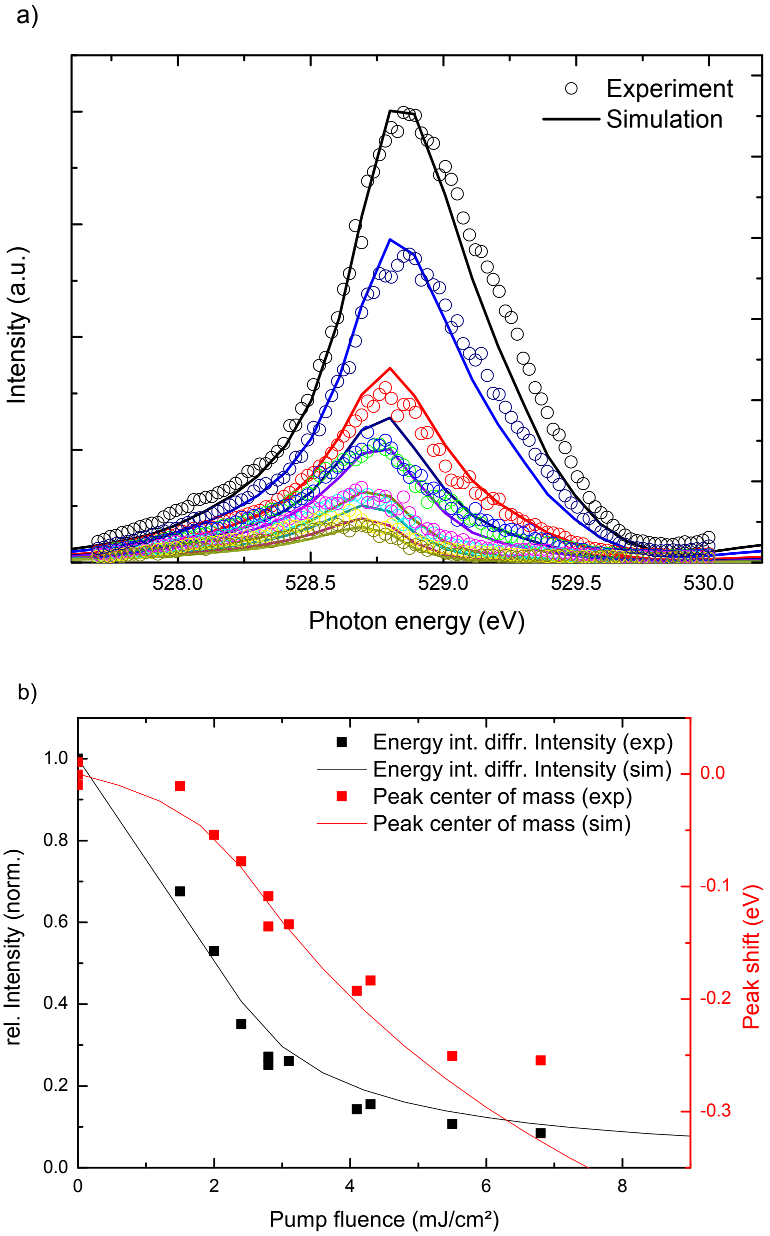

Figure 7.6.: (a) Comparison of experimental spectra recorded for different pump fluences (symbols) and the simulated spectra (lines). (b) Effect of the pump-laser induced gradient on the oxygen-K resonance spectra assuming that the experiment is probing a signal that is proportional to the number of scatterers in the probed volume.

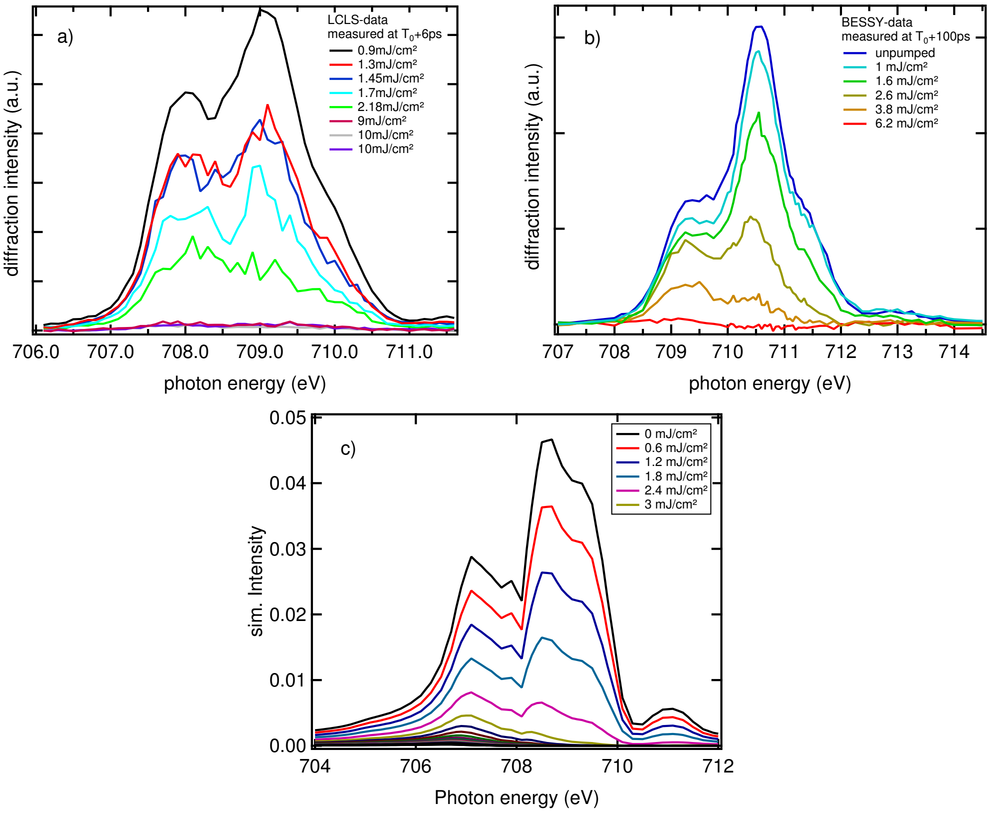

Figure 7.7.: Fe-L_3 spectra of the $(00\frac{1}{2})$ CO/OO peak. Panel a) shows the measured data at the FEL LCLS at a time delay of 6 ps. Panel b) contains the data measured at the storage ring BESSY II at a time delay of about 100 ps. In panel c) simulated Fe-L_3 spectra for different pump fluences are shown.

This very simple model describes most of the experimental observations with amazing accuracy. The fluence scales of experiment and simulation at both resonances do not match exactly, but the assumption of a pump laser induced gradient can explain all our experimental findings such that possible smaller intrinsic changes of the natural spectrum can not be reliably extracted. Our findings are of huge importance for all time-resolved pump probe resonant diffraction experiments. It shows that through the pump gradient particular energy regions of the spectrum can be reduced in measured RSXD spectra due to the absorption in the near surface layers.

On the other hand, this effect can be used to monitor the temporal evolution of the pump gradient. In this case of magnetite this pump gradient lives rather long for more than 100 ps. In Fig. 7.7a) the FEL data at a time delay of 6 ps are shown and can be compared with the storage ring data measured at a time delay of about 100 ps shown in panel 7.7b). Both data series show the same behavior as discussed before. In consequence these experimental findings demonstrate that for time-resolved RSXD consideration of pump induced laser gradient effects for interpretation of the data at all time delays is essential. Moreover, our findings give the direction to reconstruct the pump laser gradient effects of the near surface layers dependent on the time delay after laser excitation.

Chapter 8.

Ultrafast demagnetization mechanisms in antiferromagnetic Holmium

Motivated by the prospect of faster data processing and storage technology, a wealth of experimental and theoretical studies has dealt with ultrafast spin manipulation [13, 14, 16, 24]. It has turned out that the speed limit for spin manipulation is defined by the maximum rate at which angular momentum can be transferred from the spin system to other subsystems. We show that after optical excitations atomic spin angular momentum transfer in an antiferromagnetic metal holmium can be much more efficient than for ferromagnetic metals of that have a very similar structure otherwise. To achieve the same angular momentum transfer rate in the antiferromagnet, a ten times lower excitation density is needed than in the ferromagnet. We assign this ultra-efficient process to a redistribution of angular momentum within the spin system. Our finding shows a possible route towards faster and more energy-efficient spin manipulation.

Different channels for the drain of angular momentum out of the spin system have been identified and their relevance for ultrafast demagnetization processes is presently the subject of an intense debate [16, 127–129]. While for the suppression of ferromagnetic order angular momentum has to be transported out of the spin system, the suppression of antiferromagnetic order can - in principle - be achieved by the redistribution of angular momentum *within* the spin system: both the ordered and the disordered system carry no net angular momentum. Based on this argument, antiferromagnetic dynamics have been predicted to be considerably faster than ferromagnetic dynamics. Experimental evidence for antiferromagnetic dynamics is rare, though. In studies on antiferromagnetic oxides indeed dynamics on time scales of below 200 fs, but also much slower dynamics on picosecond time scales [1–4, 6, 20–22] were observed. Because of the different exchange coupling mechanisms in oxides and metals, however, a direct comparison with the most relevant ferromagnetic metals is difficult.

To connect to the understanding of ferromagnetic metals, a study of a metallic antiferromagnet is clearly better suited. We therefore chose the prototypical Heisenberg-antiferromagnet holmium for our experiment. Holmium has a magnetic moment of 10.6 μ_B per atom, which is mainly carried by the partially filled $4f$ shell. Indirect exchange interaction (RKKY) [130–132] and anisotropies lead to the formation of a helical spin structure below $\approx$ 140 K [133] (Fig. 8.1a). In terms of magnetic coupling strength and anisotropy energies, holmium is similar to the well-studied $4f$ ferromagnet terbium (9.34 μ_B per atom) such that a comparison of these two materials reveals the influence of antiferromagnetic order on the magnetic dynamics. As a probe for the antiferromagnetic order, we used resonant soft x-ray diffraction at the $3d \rightarrow 4f$ (M_5) resonance [44] from an 8 nm thick holmium layer grown by molecular-beam epitaxy between yttrium buffer layers [44]. The helical magnetic order leads to the appearance of a magnetic diffraction peak at (00τ) with $\tau \approx 0.25$. The intensity of the magnetic peak is proportional to the squared antiferromagnetic order parameter [44]. The experiments were carried out with 100 fs and 100 ps x-ray pulses at the FEMTOSPEX slicing facility at BESSY II. Upon pumping with an

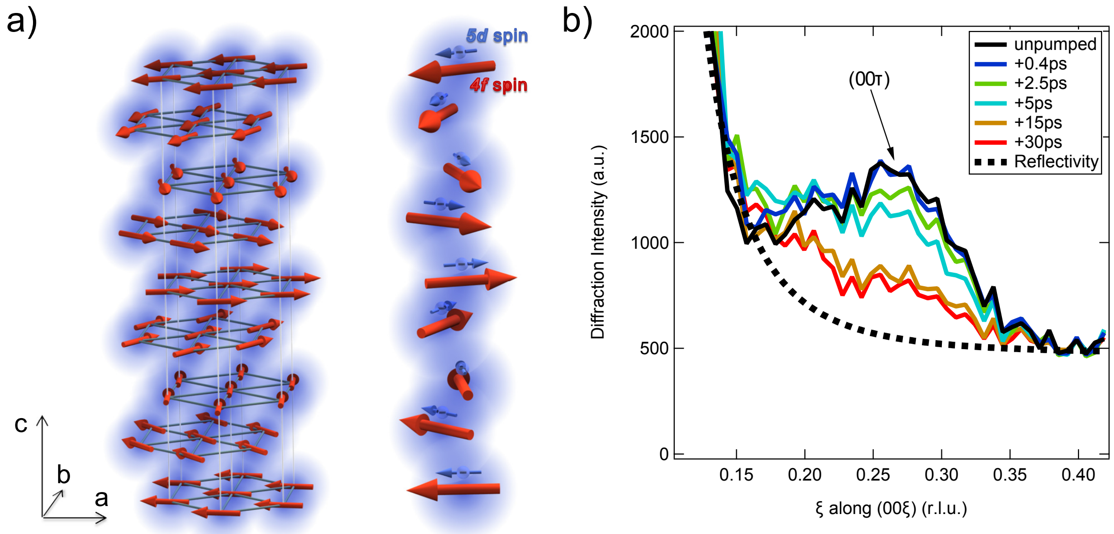

Figure 8.1.: a) Sketch of the helical magnetic structure in our holmium sample. The red arrows denote the localized $4f$ moments that are ferromagnetically aligned within the ab-planes; the helix propagates along c with a period length of about 8 ML. The blue arrows denote the delocalized $5d$ moments which are ferromagnetically coupled to the $4f$ moments by a strong intra-atomic exchange. b) Momentum scans along [001] (L) through the magnetic diffraction peak for different delays recorded with 100 fs x-ray probe pulses for a pump fluence of 0.42 mJ cm^{-2}. Upon pumping the peak intensity is reduced. The sloping background that is left after 30 ps is mostly the specular reflectivity from the film.

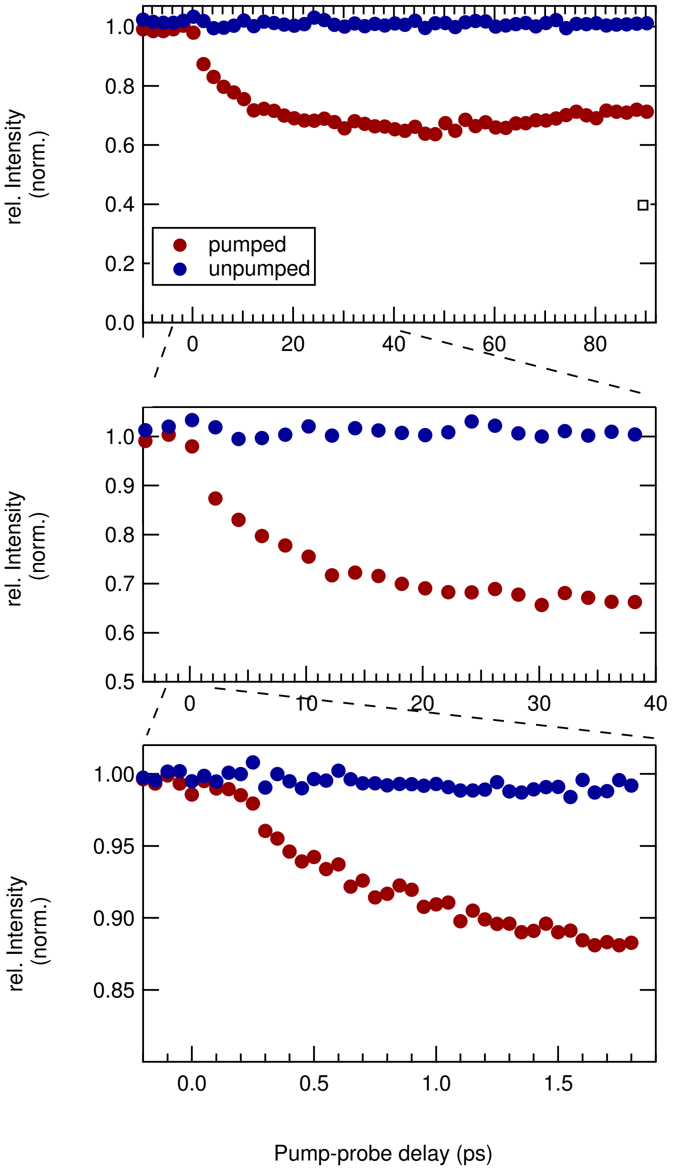

Figure 8.2.: Time dependence of the magnetic scattering signal after the pump pulse (red symbols). In the top frame showing a wide time interval the initial decay and the subsequent recovery can be seen. Zooming in to the decay region reveals two time scales. The used pump fluence on the sample was 0.28 mJ cm^{-2}. The blue symbols show the magnetic intensity in the reference data set without pump pulse recorded alternating with the pumped signal. Both intensities were normalized to their value for negative delay times.

infrared laser pulse (800 nm wavelength) the intensity of the magnetic diffraction peak is suppressed, while the peak position does not change at least within the first 40 ps (Fig. 8.1b). The intensity at the position of the peak maximum (after subtraction of the reflectivity background) is hence a well suited measure for the antiferromagnetic order. In Fig. 8.2 delay scans are presented, for which the time interval between the pump pulse and the probe pulse was varied. Upon impact of the pump pulse the intensity drops, strides through a minimum after about 40 ps (for the given pump fluence) and recovers afterwards. Zooming into the decay shows two different regimes: a fast initial decay followed by a slower decay.

The occurrence of a fast and a slow time scale for the decay of magnetic order resembles what has been found for ferromagnetic Tb and also for the ferromagnetic lanthanide material Gd [14]. Taking the temporal resolution of the experiment into account, we determine for holmium a time constant for the fast decay of (350 ± 80) fs and for the slow decay (22 ± 2) ps. The slow time constant is about twice the number found for Tb (8 ps) and half of the Gd value (40 ps). The smaller value for Tb with respect to Gd has been assigned to a direct coupling of the $4f$ magnetic moment to the lattice mediated via the orbital momentum (which vanishes for Gd) and the resulting magneto-crystalline coupling [14]. For holmium, which carries orbital moment, this channel exists as well, but appears to be less efficient than for Tb. Very remarkable is our result for the short time constant, which is about 400 fs less than what has been observed in Tb (760 fs) and Gd (740 fs) [14]. The only significant difference between Tb and Ho is the existence of non-collinear spins in the latter. We therefore suggest faster demagnetization dynamics in holmium to come from the interchange of non-collinear spins between neighboring atoms. The actual spin transfer occurs via the $5d$ electrons and is then efficiently transmitted to the $4f$ system through the strong intra-atomic exchange. This channel is not effective for demagnetization of ferromagnetic order.

The difference to the ferromagnets appears even more striking when the transferred angular momentum is quantitatively referred to the amount of deposited excitation energy. In order to do so, the reflectivity background signal caused by radiation from non-sliced electrons (halo) were determined from the fluence dependence of the diffracted intensity at the time delay of the biggest dynamic pump effect (+ 40 ps). Under the assumption that at the pump fluence of about 1.2 mJ cm^{-2} the magnetic order is entirely destroyed, we can estimate the basically fluence independent background. From a static temperature dependent measurement series we know that at 40 K 8.6 μ_B per atom effectively contribute to the AFM order. This number was assigned to the unpumped signal taking into account that the magnetic diffraction intensity is proportional to the squared order parameter. After subtraction of halo and reflectivity background from the measured traces we then normalized the delay scans to their respective signal level before time zero. Figure 8.3 shows the such derived delay scans on an normalized y-scale.

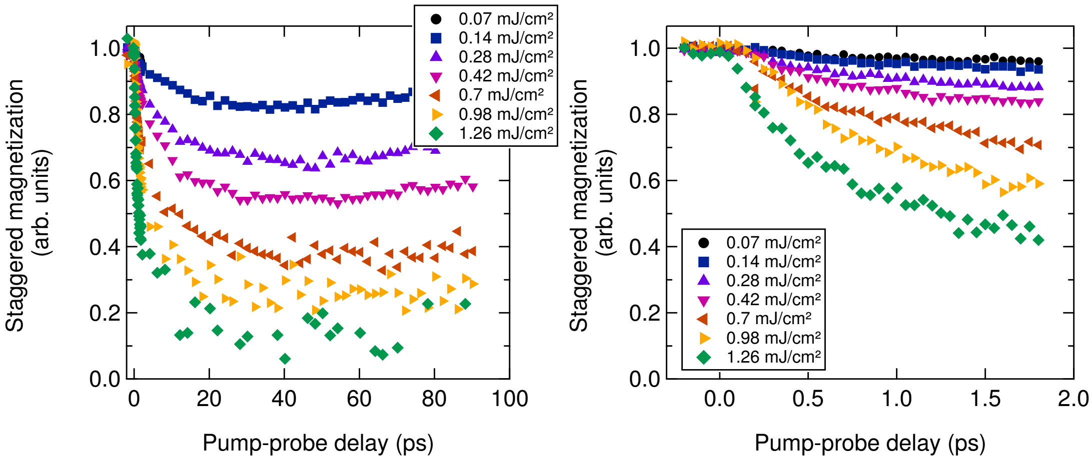

Figure 8.3.: Fluence dependent delay scans representing the AFM order. In the left panel the first 100 ps are shown, whereas the right panel displays the first 2 ps after laser excitation.

Figure 8.4 shows derived angular momentum transfer rates per effective excitation density for antiferromagnetic holmium and for different $4f$ and $3d$ metallic ferromagnets [13, 14]. The transfer rates for all ferromagnets are within a band of an average slope of 0.4 $^{\mu_B}/_{(\mathrm{ps\ mJ\ cm^{-2}})}$. For Holmium we find comparable transfer rates, however, for ten-times lower excitation densities. Obviously the transfer of angular momentum in the antiferromagnet is not only faster, it is also much more efficient.

The highly efficient interatomic transfer of angular momentum defines a route towards more energy-efficient ultrafast spin manipulation. Disorder in non-collinearly coupled magnetic moments can reduce the energy needed to manipulate spin order and/or allow for tuning time constants. The all-optical switching in, e.g., the ferrimagnetic GdFeCo occurs via an almost complete quenching of the magnetization in the material [24]. Most of the angular momentum needs to be transferred out of the Gd $4f$ system. Based on our finding, the energy needed to reach this transfer should be much lower when antiparallel $4f$ spins are available in the neighborhood of those $4f$ spins that carry the magnetization. This could be the case either within one material via alloying or possibly even in a multilayer structure via superdiffusive spin transport [16]. More energy efficient all optical switching may facilitate implementing this principle into a real device.

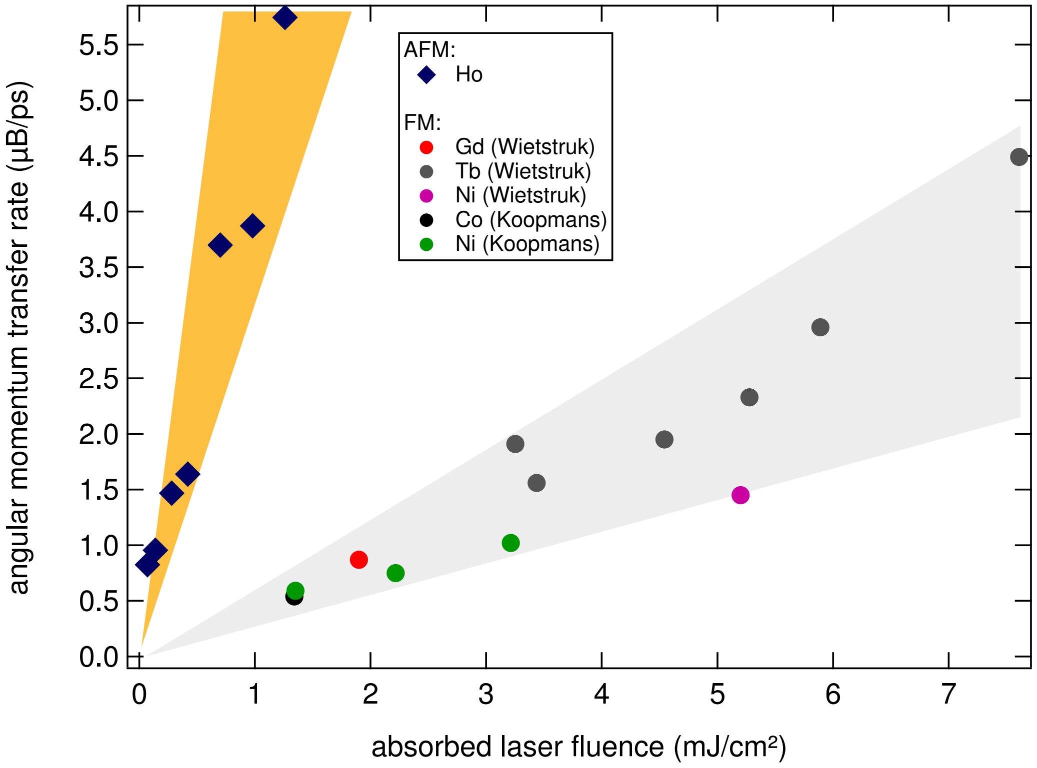

Figure 8.4.: Demagnetization rate vs. pump energy per ion for different ferromagnetic metals and for holmium. All ferromagnets can be found within a band around a demagnetization rate of 0.4 $^{\mu_B}/_{(\mathrm{ps\ mJ\ cm^{-2}})}$. This value is ten times higher for antiferromagnetic holmium. The data for the FM materials were taken or calculated from Wietstruk et al. [14] and Koopmans et al. [13].

Chapter 9.

Laser-induced magnetic and structural dynamics in EuTe

Since the discovery of ultrafast demagnetization in ferromagnetic nickel in 1996 by Beaurepaire et al. [9], scientists have been trying to understand the underlying fundamental processes [2, 10, 22, 23, 134, 135]. Still it is not yet fully clear what happens within the first picoseconds after excitation with an external laser pulse. Although most of current ideas seem to agree on the fact that after demagnetization angular momentum from the spin system is finally taken up by the lattice (an idea which is strongly supported by the famous Einstein-De Haas experiment [136]) ultrafast experiments so far have only been probing magnetic or electronic degrees of freedom alone. Experimental evidence from directly probing the lattice dynamics during demagnetization is, however, still outstanding [9, 13, 17]. Apart from that, however, the lattice dynamics is regarded as slow and irrelevant on shorter times scales. That lattice dynamics generally may be involved in demagnetization even on an ultrafast timescale could be motivated by the studies of oxide materials like Fe_3O_4 (see chapter 6) where lattice dynamics on time scales well below 300 fs is found. The role of lattice dynamics for the spin degree of freedom might be furthermore important since from all optical measurements it is known that optical laser pulses can affect the underlying structure by the creation of sound waves [25–27]. The latter, in turn, can affect the magnetic coupling via bond length variation. Also a direct coupling between spin and lattice via magnetostriction may occur. It is essential to better understand the interplay between spin and lattice degrees of freedom, also for the intelligent design of potential functional materials.

In order to reveal the interplay of the different degrees of freedom in a laser-induced AFM phase transition, we investigated the structural and antiferromagnetic response in one and the same experiment on the antiferromagnetic semiconductor EuTe. EuTe crystallizes in the rock salt structure ($a = 6.598$ Å [137]). Here divalent Eu has a spin of $S = {}^7\!/_2$ with vanishing orbital moment. EuTe orders antiferromagnetically below 10 K for the bulk material and below 13 K for a thin film [138, 139]. The Eu spins order ferromagnetically within each (111) plane where adjacent (111) planes are antiferromagnetically ordered, and separated by Te layers. Figure 9.1(a) shows the crystal structure with Eu and Te sites. In reciprocal space this magnetic order leads to a magnetic diffraction peak at (½ ½ ½), whereas the (111) is a purely structural reflection.

The AFM order in EuTe is the result of competing nearest neighbor (nn) and next nearest neighbor (nnn) indirect superexchange coupling and is describable by the following Hamiltonian H [140]:

$$H = -\sum_{nn} J_1 S_0 S_{nn} - \sum_{nnn} J_2 S_0 S_{nnn}, \tag{9.1}$$

with $J_1 > 0$ (FM) and $J_2 < 0$ (AFM). Both J_1 and J_2 depend largely on the distance between two atoms. Since the absolute and relative size of J_1 and J_2 should directly affect the magnetic order we expect a coupling of magnetic and structural degrees of freedom. In the series of europium monochalcogenides (EuX, X following the 16th

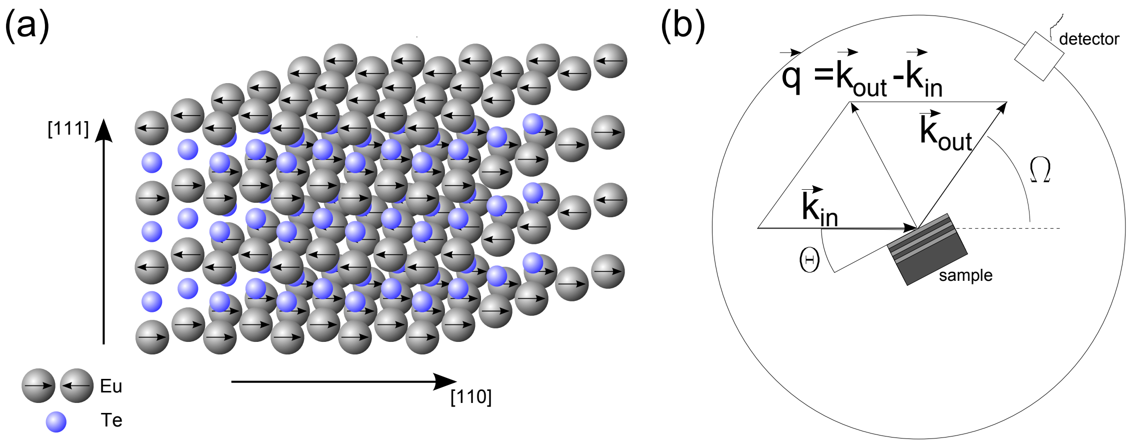

Figure 9.1.: (a) Sketch of the EuTe rocksalt structure with antiparallel aligned FM Eu planes along the body diagonal. The small balls indicates Te-sites. The antiparallel aligned Eu layers are stacked along the [111]-room diagonal direction. (b) Sketch of the scattering plane with in and outgoing momentum transfer.

group in the periodic table from oxygen to tellurium), the lattice constants increase from 5.14 Å for EuO to 6.6 Å for EuTe. This leads to the occurrence of different magnetic structures in this series. In addition, magnetostriction has been reported for EuTe by Rodbell et al. [141]. Furthermore, the size of the Eu ions depends on the oxidation state (Eu^{2+} is bigger than Eu^{3+}). A $4f \rightarrow 5d$ excitation at the Eu site could turn a large magnetic Eu^{2+} ion into a small non-magnetic Eu^{3+} ion with consequence for magnetic coupling and the lattice. Due to the strong interdependence of the magnetic structure and the ion distances a strong coupling of the magnetic and structural degree of freedom may also be expected on the ultrashort timescale during demagnetization upon laser excitation.

In our experiments we used high-quality 40 ML (≈ 153 Å) thin-films of EuTe grown between different substrate and buffer layers. The first sample set was EuTe grown on the isostructural PbTe. The lattice mismatch is only on the order of 2.5 % such that EuTe grows in a compressed pseudomorphic structure. This substrate leads to the structurally best films. The second sample set was EuTe grown on BaF_2. The lattice mismatch of about 6 % leads to a few distorted, imperfect EuTe-layers at the interface before the EuTe-layers relax to their native lattice constant.

Using the above described two different sample morphologies allowed us to study two distinct excitation scenarios. We used 3.1 eV (400 nm) photons for direct excitations in EuTe in a BaF_2 (cap) / EuTe / BaF_2 (buffer) sample, as BaF_2 has a band gap of about 10 eV [143] and thus does not absorb the laser, whereby EuTe has a band gap of about 2.3 eV and can directly be excited by the laser photons (see a scheme of energy level in Fig. 9.2) [142, 144]. We used 1.55 eV (800 nm) photons for indirect

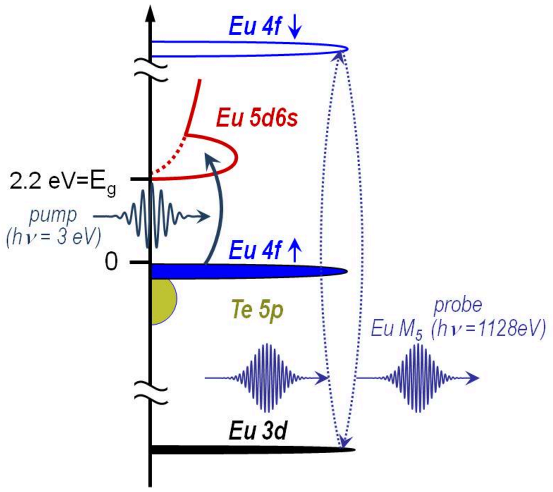

Figure 9.2.: Sketch of the relevant energy levels of EuTe. It illustrates that optical photons with energies of 3 eV can directly excite Eu $4f$ electrons over the band gap into the empty Eu $5d6s$ bands. The x-ray probe is tuned to the M_5 resonance (Eu $3d \rightarrow$ Eu $4f$), modified from [142].

excitations in the PbTe in the PbTe (cap) / EuTe / PbTe / BaF_2(buffer) sample, as PbTe has a band gap of about 0.3 eV [54] and can directly be excited while EuTe is now transparent for the 800 nm photons. In addition we pumped a sample system, BaF_2 (cap) / EuTe / PbTe / BaF_2 (buffer) with 3.1 eV (400 nm) photons which combines the direct excitation in the EuTe through the transparent capping layer of BaF_2 and high quality EuTe on the PbTe substrate, while we also expects effects from the strong absorption in PbTe that indirectly excites the probed EuTe. The used samples are listed in the following Tab. 9.1. All our samples were checked statically and characterized in terms of scattering strength and correlation lengths. Magnetic scattering was done at the Eu-M_5-resonance at 1128 eV. At the BESSY slicing source, we could only address the magnetic properties of the sample due to intensity restrictions of the beamline. We tried to answer the question of how the magnetic profile of the EuTe thin film evolves in real space after laser excitation. This idea was guided by the thermal equilibrium studies done by E. Schierle [138]. He showed from an analysis of the magnetic peak profile how the magnetization profile in

Sample composition	Excitation scenario	Excitation parameter
BaF_2 / EuTe / BaF_2	direct	3.1 eV (400nm)
PbTe / EuTe / PbTe / BaF_2	indirect	1.55 eV (800nm)
BaF_2 / EuTe / PbTe / BaF_2	dir. + indir.	3.1 eV (400nm)

Table 9.1.: List of investigated EuTe samples and excitation parameter.

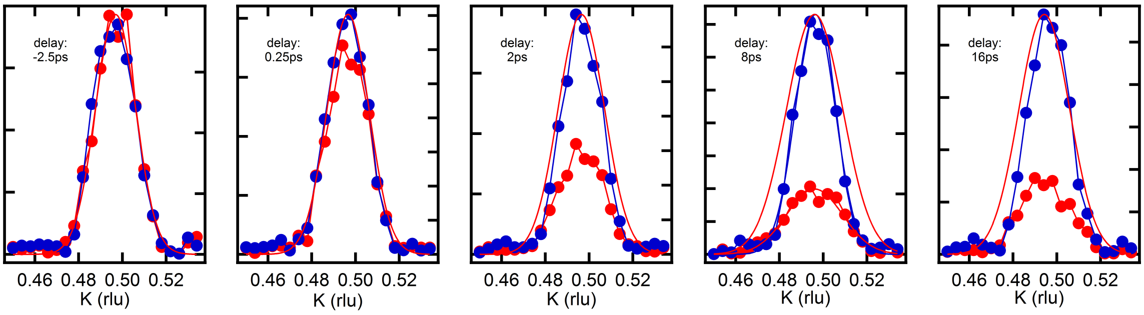

Figure 9.3.: Reciprocal space scan through the magnetic diffraction peak for different pump probe delays in the indirectly excited sample PbTe / EuTe / PbTe / BaF_2. The blue dots represent the unpumped data, the red dots represent the pumped data; the red solid lines are fits to the pumped data set, scaled to the unpumped maximum.

thin films of different thickness changes with temperature. Due to the finite width of the EuTe thin films (some tens of nm) the magnetic Bragg peak shows a so-called Laue-pattern including side maxima and minima. The intensity of these side maxima is decreasing rapidly going away from the main diffraction maximum, down by two or three orders of magnitude. With the 10^5 photons per second on the sample available in fs-slicing experiments we were basically able to record in a fs time-resolved and momentum resolved experiment the main maximum and first side maximum for a sample grown between PbTe. Some example raw data can be seen in Fig. 9.3. Upon pumping the peak intensity decreases and the width of the main peak grows.

Furthermore we measured both sample types (direct and indirect excitation) on rather long pump probe delays up to ten microseconds and with a time resolution of about 70 ps in single-bunch mode. From this data set we wanted to reconstruct the real space magnetization profile at each time delay. It turned out that the data were inconsistent with changes in the magnetization only. Additional structural distortions (compression or decompression of the lattice) had to be assumed. Since we were not able to measure purely structural information at the slicing beamline, we also conducted an experiment at LCLS where at energies of about 1880 eV enough photons are produced to measure the (111) structural reflection with fs resolution.

Figure 9.4 shows the measured reciprocal space scans through the ($^1/_2$ $^1/_2$ $^1/_2$) magnetic peak (left) and the structural (111) peak (right) for different pump probe delays in the direct and indirect excited BaF_2 / EuTe / PbTe / BaF_2 sample. The top scan presents the unpumped case and acts therefore as a reference in each plot. The subsequent lines were recorded at later delays and one can follow changes in the positions and widths of the main peaks. The slope in the structural data at the high q-side belongs to the onset of the (111)-reflection from the PbTe buffer layers. For the (111) peak the dynamic changes are more clearly visible compared to the magnetic

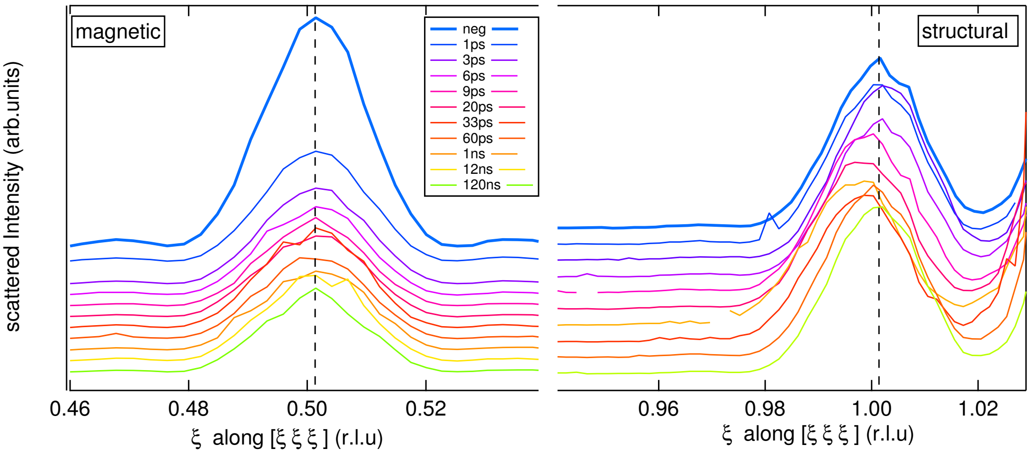

Figure 9.4.: Reciprocal space scans through the magnetic peak for different pump probe delays (unpumped top curve to later times in the bottom) are shown in the left part. The right part shows the same scans for the structural Bragg reflection. (measured at LCLS)

peak. In particular for intermediate delays (around 30 ps) the structural peak shifts are more pronounced than the magnetic order reflection. The magnetic reflection intensity is pumped down by roughly 40 % compare to the unpumped intensity while the structural intensities are almost not influenced by the pump pulses.

In Fig. 9.5(a) the intensities (top panel), the amount of the peak shift (middle panel) and the peak width (bottom panel) as a function of the delay is presented. As obvious from the scans, there is a loss of magnetic order which is visible in a decrease of intensity by approximately 40 %, while the intensity of the structural reflection is almost not affected. Directly after time zero the correlation of the magnetic order and of the lattice begins to decrease, cf. the large width in reciprocal space. Peak positions react simultaneously on the pump pulse reaching a maximum distortion at about 50-1000 ps. We find, however, an almost 10 times larger shift of the lattice reflection compared to the magnetic reflection.

Figure 9.5(b) shows delay scans on both reflections in the first 20 ps. As the structural intensity does not change much as a function of delay, we measured the structural response on the left rising slope of the peak (marked with an arrow) to be more sensitive to the shift of the peak position. The change in width contributes only mildly. Higher (lower) intensities in the delay scan reflect mainly a shift towards lower (higher) values in reciprocal space units or higher (lower) real space lattice constants. We find a rapid drop of intensity for the antiferromagnetic reflection to about 60 %. Fitting the magnetic curve with a biexponential decay and with an experimental time resolution of about 300 fs, the data show a fast timescale of about (430 ± 90) fs

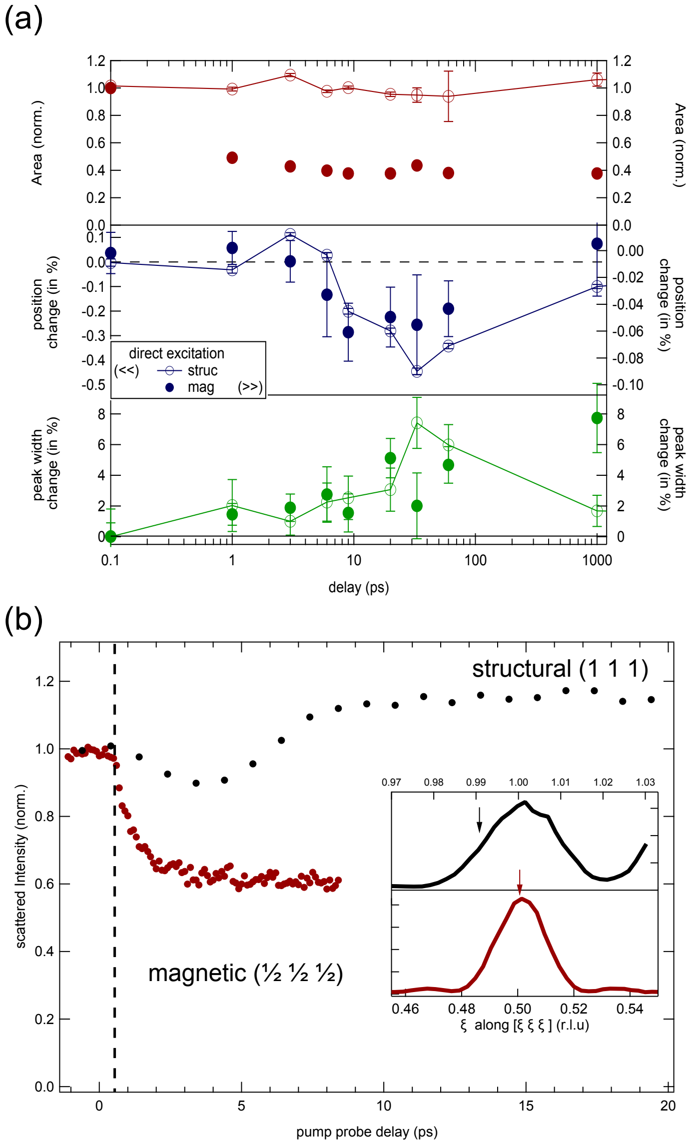

Figure 9.5.: Results from the BaF_2 / EuTe / PbTe sample. (a) Properties of the main peaks versus delay. Top panel displays the intensity, the middle panel the position (shift) and the bottom curves present the peak width, each as a function of the pump probe delay. Note that the scales for the shifts are different for the two reflections. The points at a delay of 0.1 ps are the unpumped data due to the logarithmic delay scale. (b) Pump-probe delay dependent scattered intensity for both AFM (red) and structural (black) reflection. In the inset the corresponding unpumped longitudinal scans are shown. The arrows indicate where the respective delay scan was measured. The dashed line is a guide to the eye.

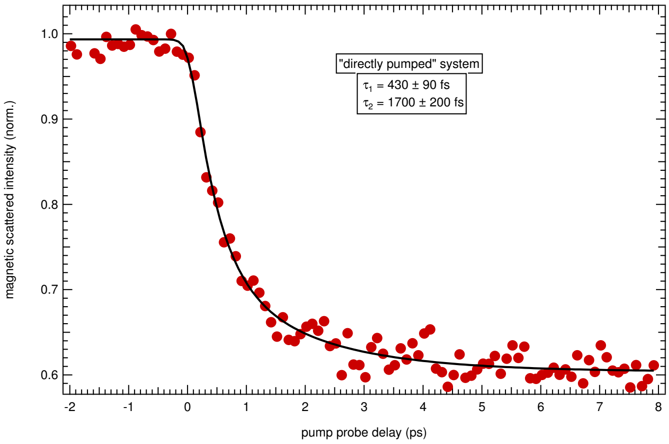

Figure 9.6.: Pump probe delay scan of the magnetic reflection in the direct excitation scenario. The solid line is the double exponential fit to the experimental data (symbols).

and a second time constant of about (1700 ± 200) fs. The fitted delay scan can be seen in Fig. 9.6. In contrast the structural response seen in Fig. 9.5 is much slower. Only in the time region where the second magnetic timescale is dominant we see a compression of the structure (change of the average lattice constant). After around 7 ps the structure changes from a compressed to an expanded state. The latter one levels off at a maximum after around 15 ps. Subsequently it is followed by shock wave or phonon modes which will be discussed later [145–147].

In the sample discussed so far, the pump laser excites the EuTe layer directly, but also a large amount of energy is deposited in the PbTe substrate. Heating of the substrate will launch a shock wave in the EuTe layer, along with potential spin transport processes. Eschenlohr et al. [16] presented an ultrafast very effective spin transport demagnetization mechanism in Au/Ni that leads to a rapid demagnetization of Ni even though the pump laser photons are absorbed in the Au layer. To address which role such indirect pumping processes play in EuTe, we used the discussed EuTe film that was grown between PbTe. Since 800 nm photons are within the band gap of EuTe but are strongly absorbed in PbTe, the pump laser photons *exclusively* excite the cap and buffer layer (see Figs. 9.10 and 9.11 for the excitation profile details.)

Figure 9.7 shows the corresponding curves and analyzes as done for the previous sample, except for a detailed analysis of longitudinal structural scans. Due to limited beamtime we lack this information. Instead a detailed analysis of the magnetic peak measured at BESSY II for identical excitation conditions is shown. A cross-check at LCLS leads to the same key features of the three parameters.

We find very similar dynamics in the indirect pumping scenario as before. Interestingly the observed effects on the magnetic peak intensity, position and width are larger with indirect pumping. For the magnetic dynamics we find a fast timescale of about

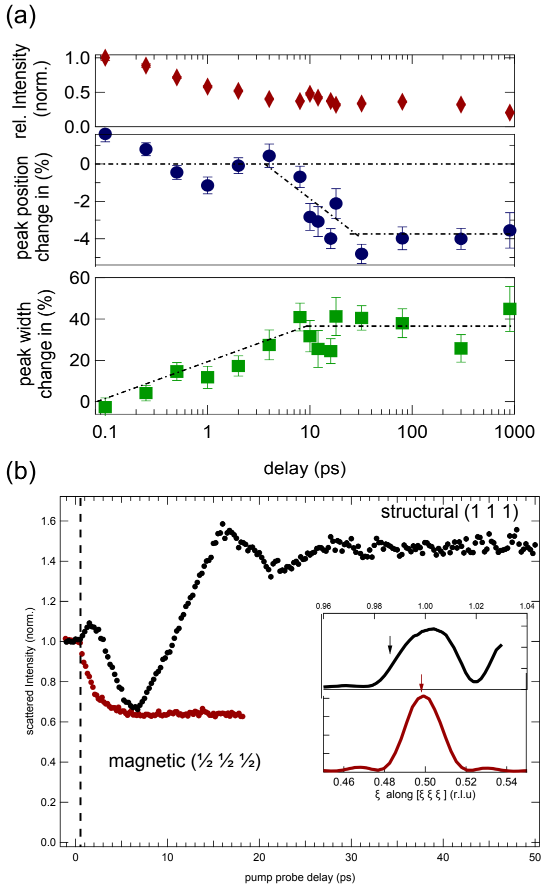

Figure 9.7.: Results from the PbTe / EuTe / PbTe sample. (a) Analyzed results from the magnetic peak of each reciprocal space scan per delay. Top panel contains the intensity, the middle panel the position (shift) and the bottom curves present the reciprocal width change (broadening), each as a function of the pump probe delay. The points at the delay of 0.1 ps are the unpumped data due to the logarithmic delay scale. The dashed lines are guide to the eyes. (b) Pump-probe delay dependent scattered intensity for both AFM and structural reflection. Black curves represent the structural response whereas the red curves the magnetic response. In the inset the corresponding unpumped reciprocal space scans are shown. The arrows indicate where the respective delay scan was measured. The dashed line is a guide to the eye.

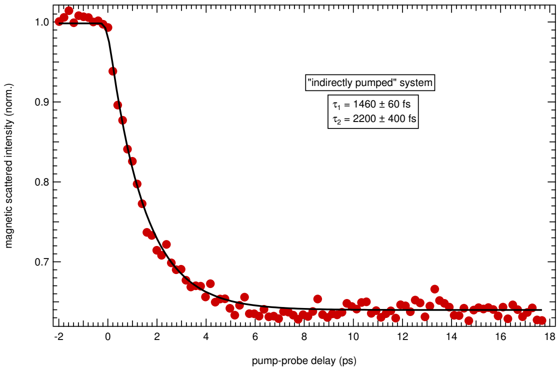

Figure 9.8.: Pump probe delay scan of the magnetic reflection in the indirect excitation scenario. The solid line is the double exponential fit to the experimental data (symbols).

(1460 ± 60) fs and a slower time constant of (2200 ± 400) fs (fits shown in Fig. 9.8). Both time scales are slower compared to the direct pump scenario but surprisingly fast considering that the energy needs to be transferred out of the neighboring layers. Even though laser photons cannot directly excite EuTe, the electrons that are created in PbTe can have enough energy to travel ballistically into EuTe and occupy empty conduction band states (for band structures of PbTe see [148–150] and for EuTe see [150–152]). When both Fermi-energies are assumed to be centered in the band gaps of each material [153], the height of the energetic barrier for valence electrons in PbTe is only about 1.25 eV. This value is calculated from the distance of the valence band maximum in PbTe (half the band gap , i.e. 0.15 eV below the Fermi energy) and the conduction band minimum in EuTe (half the bandgap, i.e. 1.1 eV above the Fermi energy). Therefore laser excited electrons in PbTe can reach the conduction band of EuTe. Ballistic electrons move with speeds of around $5 \cdot 10^5\ {}^{\mathrm{m}}\!/_{\mathrm{s}} = 5 \cdot 10^2\ {}^{\mathrm{nm}}\!/_{\mathrm{ps}}$ [16] and are therefore fast enough to cause the observed loss of magnetic order in the EuTe layers. The fact that the demagnetization time is considerably faster for direct pumping shows the high efficiency of the direct ($4f \to 5d$) excitation.

The structural response for the indirect pumping scenario shows the contraction around 7 ps and the maximal expansion around 15 ps as well as subsequent oscillations. Both are more pronounced than in the direct pumped case as visible in Fig. 9.9. An interesting feature that prominently shows up for the indirect pumping case is the expansion that occurs during the fast decay of magnetic order leading to the peak at around 1-2 ps. We assign this ultrafast expansion of the EuTe-film to an ultrafast release of magnetostriction [141]. Magnetostriction release is also reflected on the magnetic response for both pumping scenarios. For the magnetic peak positions we find a shift to lower values in reciprocal space (Figs. 9.7(a) and 9.5(a)) on the relevant timescale between 0 ps and 10 ps. The overall observation that the peak shifts affect both, the magnetic and the structural reflection, but have much larger amplitudes for

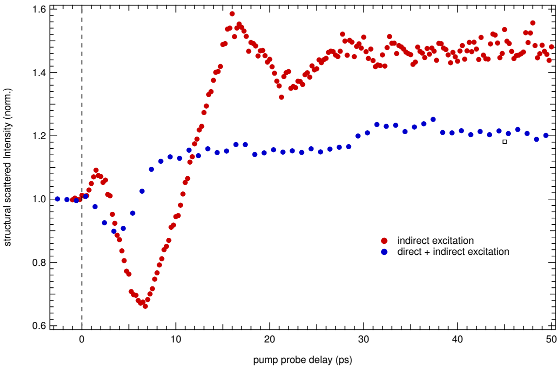

Figure 9.9.: Direct comparison of both structural responses of direct+indirect excitation (blue symbols) and indirect excitations (red symbols).

the structural peaks shows the character of the involved phonon modes. Simulation of a magnetic and the structural reflection from a 40 ML thick film taking changes of positions of Eu and Te sites into account, lead to fairly good agreements with the experimental data when we assume that Eu sites move relative to the Te site, like a longitudinal optical phonon would do. For the magnetic signal, where only the Eu sites are probed, this results in a much smaller response as in the structural signal, where Eu and Te sites contribute.

Colleagues from the group of Prof. Bargheer, University of Potsdam, especially Dr. Daniel Schick, have simulated the structural strain wave dynamics which propagate through our samples using a model of masses and springs (see Ref. [27]). Figure 9.10 shows the results of these simulations for the direct pumped scenario. The top left panel shows the initial temperature rise as a function of sample depth under the assumption that all the laser power goes directly into heat. One sees, that only negligible amounts are absorbed in the capping layer. A large fraction is directly absorbed by the EuTe layer. Finally, the largest fraction is absorbed by the PbTe substrate. This initial excitation profile can then be followed in the time domain resulting in strain waves starting at the interfaces as it is depicted in the left bottom panel of Fig. 9.10. From this temporal evolution one can calculate an average strain in the whole EuTe layer. This can be seen in the same figure in the right bottom panel, and can be directly translated into a shift of the Bragg peak. In the top right the experimental structural delay scan can be compared to the simulation. All important features match. From these findings we conclude, that in the direct pumped scenario all observed structural changes are due to strain waves.

The results for the indirectly pumped, PbTe/EuTe/PbTe-scenario are shown in Fig. 9.11. Here, the agreement with the experiment is worse. Deviations between experiment and simulation results are: 1) The lattice expansion directly after time zero which is not reproduced by the model and 2) the additional kink at around 8 ps in the simulation which is not experimentally observed. As illustrated in the left

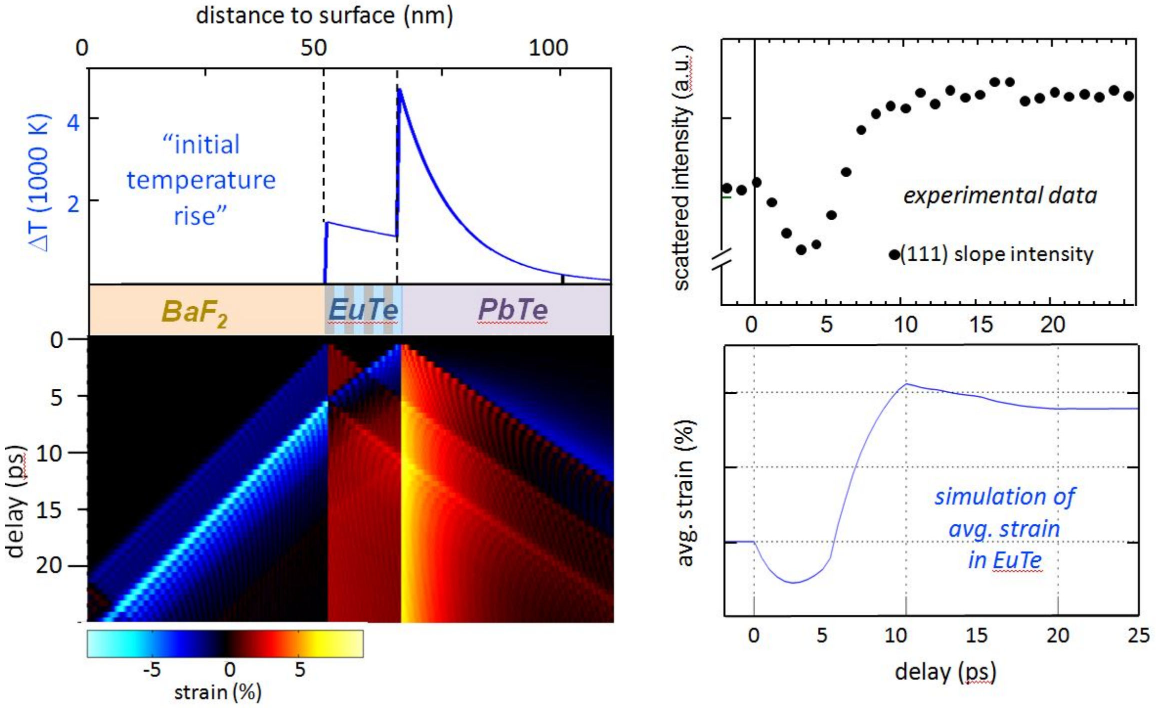

Figure 9.10.: Initial temperature rise profile in the BaF_2/EuTe/PbTe-direct-pump-scenario under the assumption that all the laser power is instantly transferred into heat (left top). No energy is absorbed in the capping layer, some in the EuTe layer (important for the magnetic dynamics) and the main part is absorbed in the substrate. This initial excitation profile leads to strain waves which were calculated for several delays after time zero (left bottom). The average strain in the EuTe per delay can be seen in the bottom right panel. For comparison the measured structural delay scan in the top right.

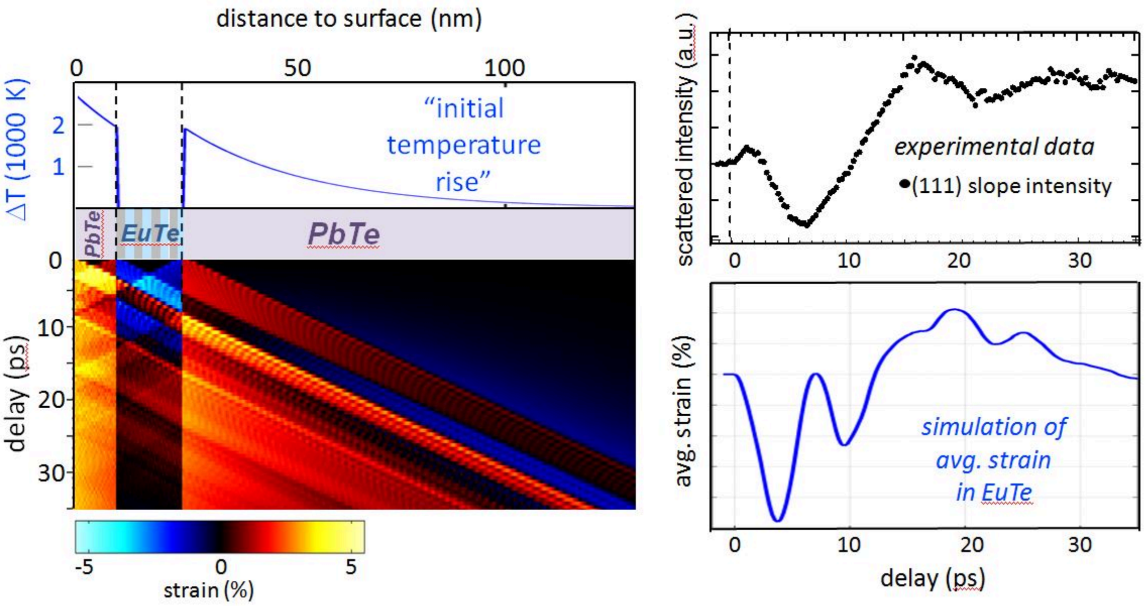

Figure 9.11.: Initial temperature rise profile in the PbTe/EuTe/PbTe-direct-pump-scenario under the assumption that all the laser power goes directly into heat (left top). One can see that the energy is either absorbed in the capping layer or in the substrate, and nothing in the EuTe layer. This initial excitation profile leads to strain waves which could be calculated for several delays after time zero (left bottom). The average strain in the EuTe per delay can be seen in the bottom right panel. For comparison the measured structural delay scan in the top right.

bottom graph, the strain waves generated at time zero at the interfaces travel through the EuTe film and are reflected and partially transmitted at the interfaces. Thus there are times when these two waves interfere within the EuTe. At around 8 ps we have the situation that half of the film is expanded whereas the other is compressed. In the simulation of the strain this leads to zero average strain. Nevertheless, in the experimental data this kink is absent. We assume that imperfect interfaces due to variation of capping layer thickness smearing out the interference. For the ultrafast expansion our original interpretation in terms of magnetostriction release is supported, because this effect is not included in the simulation.

In conclusion, we found in the direct excitation scenario an ultrafast timescale for the disordering of 450 fs. In addition we found that the ultrafast loss of magnetic order induces an ultrafast reaction of the structure hinting to ultrafast magnetostriction release. Our results also show that an indirect pumping excitation [16] can be very fast and effective also in semiconductors. Both pumping mechanisms initiate shock waves which are long lived up to μs before the sample is back in an equilibrated state. Looking on magnetic and structural responses we found effectively decoupled dynamics on short timescales with additional magnetically induced lattice dynamics.

Chapter 10.

Summary

Functional materials for information processing and storage shall allow for faster switching, higher data densities and shall be more energy efficient. New concepts of material designs and functionality are required. In the last years ultrafast non-equilibrium experiments yielded to a couple of such new concepts potentially be suited for applications. One of the investigated new systems is the class of materials involving antiferromagnetic (AFM) coupling. Since AFM order can be manipulated without transfer of angular momentum out of the spin system it has been predicted that AFM dynamics should be faster than that of FM materials. Also transition metal oxides (TMOs) are discussed as a class of materials for functionality. Especially the coupling of different degrees of freedom and resulting low energy excitations which often result in spectacular changes of macroscopic properties make these material attractive.

For this thesis I investigated the ultrafast laser-induced dynamics of three representatives of these new concepts. The applied technique was time-resolved resonant soft x-ray diffraction in a pump-probe scheme. Part of the work was the design and setup of suited soft x-ray diffraction instrumentation.

The first material that I studied was magnetite ($\mathrm{Fe_3O_4}$). It served as a prototype for functional TMOs and shows a metal-to-insulator-transition (MIT). Probing the charge and orbital order as well as the structure we found that after an optical excitation the electronic order and the structural distortion, that characterize the insulating phase in thermal equilibrium, are destroyed within the experimental resolution of 300 fs. The MIT itself only follows the ultrafast laser induced trimeron hole creation. On a (1.5 ± 0.2) ps timescale phase segregation occurs into regions that are like the low-temperature phase insulating and electronically ordered. Other regions are metallic and disordered like the high-temperature phase. The switching of conductivity in such an archetypal complex oxide at the picosecond timescale clocks these systems faster than switching processes in semiconductors developed to date. The temporal resolution of the present experiments (300 fs) could not clarify whether the lattice dynamics and the electronic dynamics are intimately linked to each other or not. Here even improved experimental schemes are needed to reveal the intrinsically short coupling times. One approach would be to apply a split-and-delay line to use the same FEL pulse for pumping and probing in order to improve the temporal resolution down to the FEL pulse length of a few fs.

Besides this transition-metal-oxide, I also investigated two antiferromagnetic $4f$ systems. In Holmium, a metallic lanthanide, a helical AFM structure forms at low temperatures. The goal of the study was to compare the magnetic dynamics of AFM with that known from FM of else similar structure. We studied the time and fluence dependence of the AFM demagnetization dynamics by probing the magnetic superstructure reflection. The prediction that AFM materials can be faster demagnetized than FM materials could be confirmed. Beyond that, however, our investigated Ho thin film could be much more efficiently pumped compare to ferromagnetic films. We found a ten times larger pump efficiency. We suggest an intra-atomic spin scattering channel which is not effective in FM systems to be responsible for the high speed as well as higher efficiency. My studies on ultrafast antiferromagnetic dynamics showed that not only the size of the magnetic moment defines ultrafast magnetic dynamics in terms of speed and energy efficiency, but also very prominently the type of coupling. A possible route towards further optimization could be the use of artificially grown heterogeneous systems like alloys, or multilayers.

In EuTe, an antiferromagnetic semiconductor, a strong interrelation of the magnetic structure and the lattice is present in thermal equilibrium. In our time-resolved studies, probing the magnetic and structural degree of freedom in one single experiment by using soft x-ray diffraction, however, we find that the dynamics of both subsystems basically evolve independently of each other. Interestingly, however, there is one exception: In case of indirect pumping we found an ultrafast magnetostriction effect, meaning that the loss of magnetic order leads the structure to relax on ps time scales.

An essential part of my thesis was also to further develop an experimental technique, where ultrafast dynamics are pumped by an optical laser, while the soft x-rays reflectivity of the sample is probed. Reflectivity measurements allow to measure time resolved XAS and XMCD effects of samples, which are not measurable in transmission. It opens the field for new kind of samples like crystalline bulk samples, epitaxial grown films and complex layered systems for time-resolved spectroscopic studies. First measurements showed that these ultrafast reflection measurements work successfully and lead to a number of future experiments.

Chapter 11.

Publications

Parts of the results of this thesis have been published in

- Speed limit of the insulator-to-metal transition in magnetite
  S. de Jong, R. Kukreja, **C. Trabant**, N. Pontius, C. F. Chang, T. Kachel, M. Beye, F. Sorgenfrei, C.H. Back, B. Bräuer, W. Schlotter, J. Turner, O. Krupin, M. Döhler, D. Zhu, S. Hossain, A.O. Scherz, W.S. Lee, Y.D. Chuang, D.H. Lu, R.G. Moore, M. Yi, M. Trigo, P. Kirchmann, L. Pathey, A. Yaresko, I. Leonov, M. Buchholz, P. Metcalf, W. Wurth, A. Föhlisch, C. Schüßler-Langeheine, and H.A. Dürr
  Nature Materials **12**, 882-886 (2013) (10.1038/NMAT3718).

- Time and momentum resolved resonant magnetic x-ray diffraction on EuTe
  C. Trabant, N. Pontius, E. Schierle, E. Weschke, T. Kachel, G. Springholz, K. Holldack, A. Föhlisch and C. Schüßler-Langeheine
  EPJ Web of Conferences, **41**, 03014 (2013).

Further publications, but not topic of this thesis:

- Stimulated X-ray Emission for Materials Science
  M. Beye, S. Schreck, F. Sorgenfrei, **C. Trabant**, N. Pontius, C. Schüßler-Langeheine, W. Wurth and A. Föhlisch
  Nature **501**, 191-194 (2013) (10.1038/nature12449).

- Analysis of Charge and Orbital Order in Fe_3O_4 by Fe $L_{2,3}$ Resonant X-Ray Diffraction
  A. Tanaka, C. F. Chang, M. Buchholz, **C. Trabant**, E. Schierle, J. Schlappa, D. Schmitz, H. Ott, P. Metcalf, L. H. Tjeng, and C. Schüßler-Langeheine
  Physical Review **B 88**, 195110 (2013)

- Charge stripe order near the surface of 12-percent doped $La_{2-x}Sr_xCuO_4$
  H.-H. Wu, M. Buchholz, **C. Trabant**, C. F. Chang, A. C. Komarek, F. Heigl, M. v. Zimmermann, M. Cwik, F. Nakamura, M. Braden and C. Schüßler-Langeheine
  Nature Communications **3**, 1023 (2012).

- Symmetry of orbital order in Fe_3O_4 studied by Fe-$L_{2,3}$ resonant x-ray diffraction
  A. Tanaka, C.F. Chang, M. Buchholz, **C. Trabant**, E. Schierle, J. Schlappa, D. Schmitz, H. Ott, P. Metcalf, L.H. Tjeng and C. Schüßler-Langeheine
  Physical Review Letters **108**, 227203 (2012), Erratum Physical Review Letters 109, 119901 (2012).

- The confocal plane grating spectrometer at BESSY II
  R. Könnecke, R. Follath, N. Pontius, J. Schlappa, F. Eggenstein, T. Zeschke, P. Bischoff, J.-S. Schmidt, T. Noll, **C. Trabant**, S. Schreck, Ph. Wernet, S. Eisebitt, F. Senf, C. Schüßler-Langeheine, A. Erko and A. Föhlisch
  Journal of Electron Spectroscopy and Related Phenomena **188**, 133-139 (2012).

- FemtoSpeX - A versatile optical pump - soft x-ray probe facility with 100 fs x-ray pulses of variable polarization
  K. Holldack, J. Bahrdt, A. Balzer, U. Bovensiepen, M. Brzhezinskaya, A. Erko, A. Eschenlohr, R. Follath, A. Firsov, W. Frentrup, L. Le Guyader, T. Kachel, P. Kuske, R. Mitzner, R. Müller, N. Pontius, T. Quast, I. Radu, J.-S. Schmidt, C. Schüßler-Langeheine, M. Sperling, C. Stamm, **C. Trabant** and A. Föhlisch
  submitted on 27/01/2014 to Journal of Synchrotron Radiation

Chapter 12.

Acknowledgements

- My first thank goes to Prof. Dr. Alexander Föhlisch (HZB) and Prof. Dr. Markus Braden (Cologne University). Both made it possible that I as an employee in Cologne could work at HZB and was supervised in Berlin/Potsdam. Alexander, thanks for all the discussions in the last years.
- Thanks to Prof. Dr. Matias Bargheer and Prof. Dr. Paul van Loosdrecht for co-refereeing the thesis.
- A heartly and warmly thanks goes to Christian (Schüßler-Langeheine), you were again my daily tutor. It makes a lot of fun to work with a boss like you. Thanks for all the fun during the really uncountable beamtimes in these 3-4 years. I really enjoyed the time.
- A not less warmly thanks goes to Niko (Pontius). We had so many beamtimes together and every of these made a lot of fun. Thanks for all the knowledge you taught to me.
- Marcel, without you it had not been possible to set up the chamber in our BMBF project. Thanks for all the beamtimes at BESSY, PETRA, ALS, ESRF and the nice social evenings. Thank you also for the support you did for me for all the bureaucratic issues I had to settle.
- Martin, not only your code to access the FEL-data was an essential element during my years at HZB. Also our huge amount of time we spent together on our roadbikes helped to think about physics but also to relax, laugh and have simply fun. Thanks, thanks, thanks.
- A huge thank to Christian, Niko, Martin and Annette for reading through this thesis and providing fruitful feedback.
- Thanks for the cologne guys Jonas, Fabio, Thomas, Marcel and the secretaries Andrea, Beate, and Carmen for all the bureaucratic help I got in these years.
- My Berlin room mates Peter, Kristjan, Nele, Simon (I will not name all of my 16 colleagues I had in the old library, sorry for that...) and my colleagues Andrea, Marko, Flo, Hardy, Justina, Annette, Ilie, Torsten, Karsten, Enrico, René: Thanks for the nice atmosphere and a lot of fun during the work.
- Christian, Martin, Flo and sometimes (many) more: Thanks for joining the daily summer-'Eiskaffee' and the winter-'Kaffee Moccha'.

- All the uncountable beamtimes I joined in the last 3-4 year were not possible without the help of the beamline crews and machine physicists/engineers of ESRF, FLASH (PG2, BL2), PETRA (P04 and P10) LCLS, ALS and BESSY. Especially the thanks goes to Rolf Treusch (FLASH), Jens, Leif, Frank and Jörn (P04) and Michael, Sergeij, Fabian, Alessandro (catchword: Ramazotti ;)), Alexey and Christian Gutt (P10), Bill (thanks for four nice beamtimes), Georgi (organizing my last beamtime in March13), Tom (for the shipments) and Ralph (excellent lunch/dinner-support)(SXR,LCLS)
- All coherent beamtimes were not possible without (of course also Marcel and Christian) the colleagues from Amsterdam, Jeroen, Bo and Hans.
- A huge thank goes to the mechanical workshops in Cologne, Berlin and Hamburg. Especially the Berlin colleagues Torsten and Andreas gave me a deep insight in 3D-CAD drawings and had a lot of work but also fun with my sometimes urgent sometimes tricky and often challenging tasks.
- All the beamtimes were not possible without high quality samples. Thanks to P. Metcalf, G. Springholz, H. Zabel, Roger and Nele.
- Sorry for all people I didn't mentioned, it was certainly not made intentionally.
- Thanks to all friends and a big sorry for all the missed events/parties due to numerous beamtimes and conferences.
- The last, but not less warmly thank goes to my parents. They gave me the private support also over the distance.

Kapitel 13.

Selbständigkeitserklärung

Hiermit erkläre ich, dass ich die vorliegende Dissertation selbstständig erarbeitet und verfasst habe und alle Hilfsmittel und Hilfen angegeben habe. Ich erkläre, dass ich mich nicht für einen Doktorgrad anderorts beworben habe und auch einen dementsprechenden Doktorgrad nicht besitze. Desweiteren erkläre ich, dass ich von der zugrunde liegenden Promotionsordnung Kenntnis genommen habe.

Christoph Trabant   Berlin, den 4. Februar 2014

Appendix A.

Appendix

A.1. Further instrumentation

A.1.1. Polarization analyzer

Though not used for the experiments reported here, part of my work was the design of a polarization analyzing detector. The purpose of this detector is to characterize the polarization state of the scattered x-ray beam in the existing two circle diffractometer. With this additional information it is possible to reconstruct the scattering tensor elements and gain information about the character of charge, orbital, or magnetic order phenomena (see e.g. Ref. [154]). The working principle is the following: For polarization analysis the x-ray beam intensity is detected after specular reflection from a multilayer at an incidence angle of 45° (Brewster angle). The reflection is then recorded as a function of the angle of rotation around the axis given by the x-ray beam incident on the detector (in the range 0° - 90°). A typical multilayer for this purpose is designed such that for linear polarized light the reflection varies between 4 % for sigma-polarization and three to four orders of magnitude less for pi-polarization. Details for a first test of multilayer characterization can be found in [155].

The mechanical design is shown in Fig. A.1. The central parts are the multilayer structures. We need one multilayer structure per absorption edge region in order to achieve the highest possible reflectivity for a given energy region. In order to cover different absorption edges, a set of multilayers (symbolized in the figure as green bars) are mounted on an in-situ movable translation stage with piezo-driven actuators.

The detector is fixed at the scattering angle of 90°. Two rotation stages allow for tuning the reflection angle around the specular reflection (rocking motor) and a second one for turning the multilayers around the axis given by the incident x-ray beam (in the range 0° - 90°)(deflection angle). Via a long tube (orange/bronze) the device is mounted to an external vertical translation on one of the CF100 flanges on the top rotatable CF500 flange. The top CF100 flange contains the electrical feedthroughs for the in-vacuum motors and for the signal from the diode.

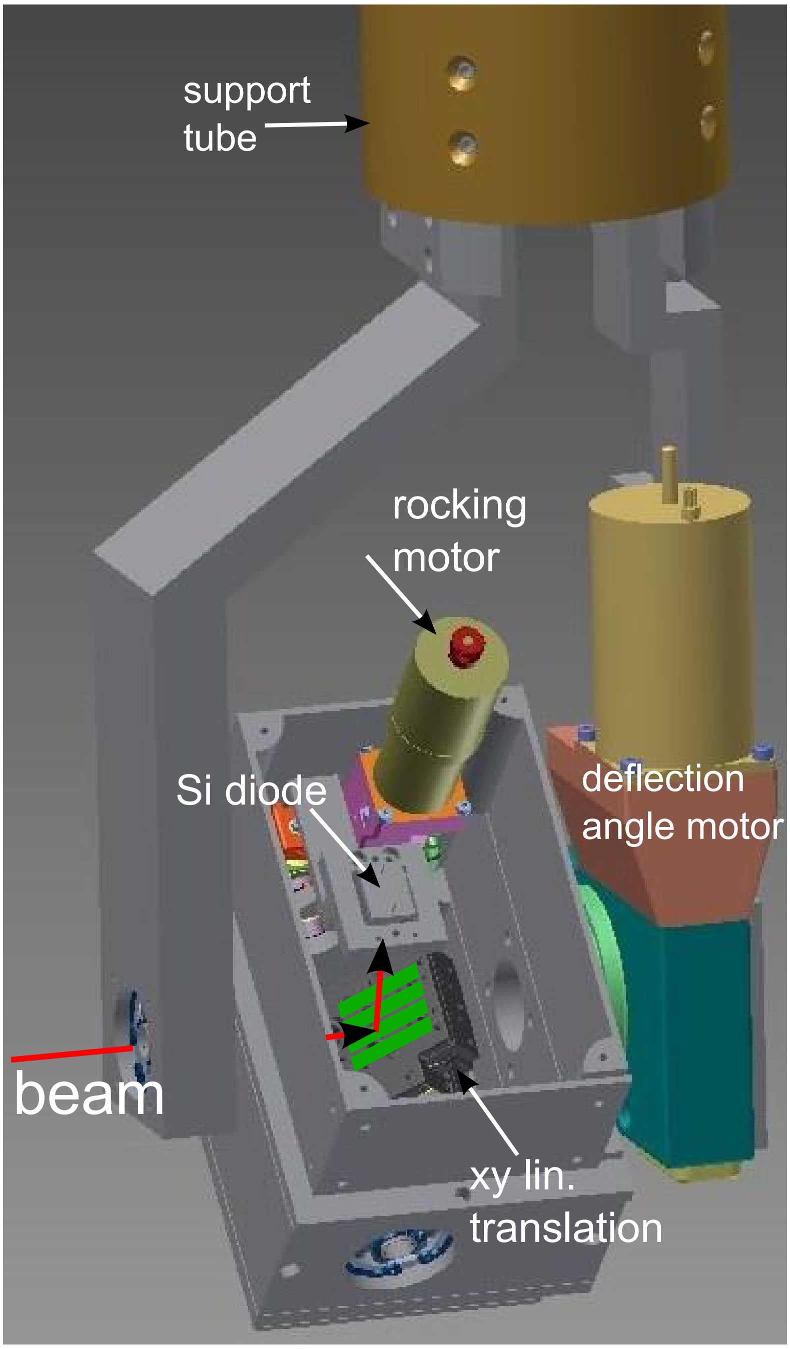

Figure A.1.: Design for the in-vacuum polarization analyzer. Four of five degrees of freedom around the center are shown: Two linear translation stages for the multilayers in the center. One for tuning the reflection angle around the specular reflection and the fourth one for turning the multilayers (symbolized as green bars) around the axis given by the incident x-ray beam (red arrows) (in the range 0° - 90°).

A.1.2. Data acquisition

For data acquisition and control of the experiment we used the software SPEC [85]. As part of my work I implemented in SPEC the control of various BESSY II beamlines and other equipment like magnet power supplies.

At FLASH data acquisition (DAQ) and beamline control are provided by the facility [156]. However, since data acquisition is realized by digitizing the detector trace at 2 GHz sample rate, a huge amount of data accrues (100 MB/s). Moreover, the acquired data are only accessible after some delay and processing. This has the drawback that the data are not available for immediate judgment of the experimental situation, which is a particular problem for aligning the chamber or searching a diffraction peak. Therefore I implemented into SPEC a quick online data acquisition (ODA) for preliminary but immediate data access. The detected signals were read out with a WAVEPRO oscilloscope which carried out the integration and synchronization and different arithmetic of the measured signal. Our software SPEC was modified such that it could control and read out the scope. Thus it was possible to align the sample/detector without using the FLASH-DAQ. In order to communicate different settings like motor positions to the FLASH-DAQ to be able to correlate measured intensities at special events in the DAQ to their corresponding motor positions. I coded motor positions in voltages which are then put into analogue to digital converter (ADC). These ADC's were then implemented as DAQ channels and saved for each pulse.

Bibliography

[1] Y. D. Chuang, W. S. Lee, Y. F. Kung, A. P. Sorini, B. Moritz, R. G. Moore, L. Patthey, M. Trigo, D. H. Lu, P. S. Kirchmann, M. Yi, O. Krupin, M. Langner, Y. Zhu, S. Y. Zhou, D. A. Reis, N. Huse, J. S. Robinson, R. A. Kaindl, R. W. Schoenlein, S. L. Johnson, M. Först, D. Doering, P. Denes, W. F. Schlotter, J. J. Turner, T. Sasagawa, Z. Hussain, Z. X. Shen, and T. P. Devereaux: Real-Time Manifestation of Strongly Coupled Spin and Charge Order Parameters in Stripe-Ordered $La_{1.75}Sr_{0.25}NiO_4$ Nickelate Crystals Using Time-Resolved Resonant X-Ray Diffraction. *Physical Review Letters* **110**, 127404 (2013).

[2] W. S. Lee, Y. D. Chuang, R. G. Moore, Y. Zhu, L. Patthey, M. Trigo, D. H. Lu, P. S. Kirchmann, O. Krupin, M. Yi, M. Langner, N. Huse, J. S. Robinson, Y. Chen, S. Y. Zhou, G. Coslovich, B. Huber, D. A. Reis, R. A. Kaindl, R. W. Schönlein, D. Doering, P. Denes, W. F. Schlotter, J. J. Turner, S. L. Johnson, M. Först, T. Sasagawa, Y. F. Kung, A. P. Sorini, A. F. Kemper, B. Moritz, T. P. Devereaux, D.-H. Lee, Z. X. Shen, and Z. Hussain: Phase Fluctuations and the Absence of Topological Defects in a Photo-excited Charge-ordered Nickelate. *Nature Communications* **3**, 838 (2012).

[3] M. Först, R. I. Tobey, S. Wall, H. Bromberger, V. Khanna, A. L. Cavalieri, Y. D. Chuang, W. S. Lee, R. Moore, W. F. Schlotter, J. J. Turner, O. Krupin, M. Trigo, H. Zheng, J. F. Mitchell, S. S. Dhesi, J. P. Hill, and A. Cavalleri: Driving Magnetic Order in a Manganite by Ultrafast Lattice Excitation. *Physical Review B* **84**, 241104 (2011).

[4] M. Först, C. Manzoni, S. Kaiser, Y. Tomioka, Y. Tokura, R. Merlin, and A. Cavalleri: Nonlinear phononics as an ultrafast route to lattice control. *Nature Physics* **7**, 854 (2011).

[5] A. Caviezel, S. O. Mariager, S. L. Johnson, E. Möhr-Vorobeva, S. W. Huang, G. Ingold, U. Staub, C. J. Milne, S.-W. Cheong, and P. Beaud: Identification of coherent lattice modulations coupled to charge and orbital order in a manganite. *Physical Review B* **87**, 205104 (2013).

[6] R. I. Tobey, S. Wall, M. Först, H. Bromberger, V. Khanna, J. J. Turner, W. Schlotter, M. Trigo, O. Krupin, W. S. Lee, Y.-D. Chuang, R. Moore, A. L. Cavalieri, S. B. Wilkins, H. Zheng, J. F. Mitchell, S. S. Dhesi, A. Cavalleri, and

J. P. Hill: Evolution of three-dimensional correlations during the photoinduced melting of antiferromagnetic order in $La_{0.5}Sr_{1.5}MnO_4$. *Physical Review B* **86**, 064425 (2012).

[7] P. Beaud, S. L. Johnson, E. Vorobeva, U. Staub, R. A. D. Souza, C. J. Milne, Q. X. Jia, and G. Ingold: Ultrafast Structural Phase Transition Driven by Photoinduced Melting of Charge and Orbital Order. *Physical Review Letters* **103**, 155702 (2009).

[8] A. D. Caviglia, M. Först, R. Scherwitzl, V. Khanna, H. Bromberger, R. Mankowsky, R. Singla, Y. D. Chuang, W. S. Lee, O. Krupin, W. F. Schlotter, J. J. Turner, G. L. Dakovski, M. P. Minitti, J. Robinson, V. Scagnoli, S. B. Wilkins, S. A. Cavill, M. Gibert, S. Gariglio, P. Zubko, J. M. Triscone, J. P. Hill, S. S. Dhesi, and A. Cavalleri: Photoinduced melting of magnetic order in the correlated electron insulator $NdNiO_3$. *Physical Review B* **88**, 220401 (2013).

[9] E. Beaurepaire, J. Merle, A. Daunois, and J. Bigot: Ultrafast spin dynamics in ferromagnetic nickel. *Physical Review Letters* **76**, 4250 (1996).

[10] C. D. Stanciu, F. Hansteen, A. V. Kimel, A. Kirilyuk, A. Tsukamoto, A. Itoh, and T. Rasing: All-optical magnetic recording with circularly polarized light. *Physical Review Letters* **99**, 047601 (2007).

[11] C. Stamm, T. Kachel, N. Pontius, R. Mitzner, T. Quast, K. Holldack, S. Khan, C. Lupulescu, E. F. Aziz, M. Wietstruk, H. A. Dürr, and W. Eberhardt: Femtosecond modification of electron localization and transfer of angular momentum in nickel. *Nature Materials* **6**, 740 (2007).

[12] C. Boeglin, E. Beaurepaire, V. Halte, V. Lopez-Flores, C. Stamm, N. Pontius, H. A. Dürr, and J. Y. Bigot: Distinguishing the ultrafast dynamics of spin and orbital moments in solids. *Nature* **465**, 458 (2010).

[13] B. Koopmans, G. Malinowski, F. Dalla Longa, D. Steiauf, M. Faehnle, T. Roth, M. Cinchetti, and M. Aeschlimann: Explaining the paradoxical diversity of ultrafast laser-induced demagnetization. *Nature Materials* **9**, 259 (2010).

[14] M. Wietstruk, A. Melnikov, C. Stamm, T. Kachel, N. Pontius, M. Sultan, C. Gahl, M. Weinelt, H. A. Dürr, and U. Bovensiepen: Hot-Electron-Driven Enhancement of Spin-Lattice Coupling in Gd and Tb 4f Ferromagnets Observed by Femtosecond X-Ray Magnetic Circular Dichroism. *Physical Review Letters* **106**, 127401 (2011).

[15] V. Lopez-Flores, J. Arabski, C. Stamm, V. Halte, N. Pontius, E. Beaurepaire, and C. Boeglin: Time-resolved x-ray magnetic circular dichroism study of

ultrafast demagnetization in a CoPd ferromagnetic film excited by circularly polarized laser pulse. *Physical Review B* **86**, 014424 (2012).

[16] A. Eschenlohr, M. Battiato, R. Maldonado, N. Pontius, T. Kachel, K. Holldack, R. Mitzner, A. Föhlisch, P. M. Oppeneer, and C. Stamm: Ultrafast spin transport as key to femtosecond demagnetization. *Nature Materials* **12**, 332 (2013).

[17] G. Zhang and W. Hubner: Laser-induced ultrafast demagnetization in ferromagnetic metals. *Physical Review Letters* **85**, 3025 (2000).

[18] A. Kimel, A. Kirilyuk, A. Tsvetkov, R. Pisarev, and T. Rasing: Laser-induced ultrafast spin reorientation in the antiferromagnet $\mathrm{TmFeO_3}$. *Nature* **429**, 850 (2004).

[19] J. H. Mentink, J. Hellsvik, D. V. Afanasiev, B. A. Ivanov, A. Kirilyuk, A. V. Kimel, O. Eriksson, M. I. Katsnelson, and T. Rasing: Ultrafast Spin Dynamics in Multisublattice Magnets. *Physical Review Letters* **108**, 057202 (2012).

[20] M. Fiebig, N. P. Duong, T. Satoh, B. B. Van Aken, K. Miyano, Y. Tomioka, and Y. Tokura: Ultrafast magnetization dynamics of antiferromagnetic compounds. *Journal of Physics D - Applied Physics* **41**, 164005 (2008).

[21] T. Kampfrath, A. Sell, G. Klatt, A. Pashkin, S. Maehrlein, T. Dekorsy, M. Wolf, M. Fiebig, A. Leitenstorfer, and R. Huber: Coherent terahertz control of antiferromagnetic spin waves. *Nature Photonics* **5**, 31 (2011).

[22] N. Kanda, T. Higuchi, H. Shimizu, K. Konishi, K. Yoshioka, and M. Kuwata-Gonokami: The vectorial control of magnetization by light. *Nature Communications* **2**, 362 (2011).

[23] S. L. Johnson, R. A. de Souza, U. Staub, P. Beaud, E. Moehr-Vorobeva, G. Ingold, A. Caviezel, V. Scagnoli, W. F. Schlotter, J. J. Turner, O. Krupin, W. S. Lee, Y. D. Chuang, L. Patthey, R. G. Moore, D. Lu, M. Yi, P. S. Kirchmann, M. Trigo, P. Denes, D. Doering, Z. Hussain, Z. X. Shen, D. Prabhakaran, and A. T. Boothroyd: Femtosecond Dynamics of the Collinear-to-Spiral Antiferromagnetic Phase Transition in CuO. *Physical Review Letters* **108**, 037203 (2012).

[24] I. Radu, K. Vahaplar, C. Stamm, T. Kachel, N. Pontius, H. A. Dürr, T. A. Ostler, J. Barker, R. F. L. Evans, R. W. Chantrell, A. Tsukamoto, A. Itoh, A. Kirilyuk, T. Rasing, and A. V. Kimel: Transient ferromagnetic-like state mediating ultrafast reversal of antiferromagnetically coupled spins. *Nature* **472**, 205 (2011).

[25] M. Herzog, W. Leitenberger, R. Shayduk, R. M. van der Veen, C. J. Milne, S. L. Johnson, I. Vrejoiu, M. Alexe, D. Hesse, and M. Bargheer: Ultrafast

manipulation of hard x-rays by efficient Bragg switches. *Applied Physics Letters* **96**, 161906 (2010).

[26] D. Schick, A. Bojahr, M. Herzog, P. Gaal, I. Vrejoiu, and M. Bargheer: Following Strain-Induced Mosaicity Changes of Ferroelectric Thin Films by Ultrafast Reciprocal Space Mapping. *Physical Review Letters* **110**, 095502 (2013).

[27] D. Schick, A. Bojahr, M. Herzog, R. Shayduk, C. von Korff Schmising, and M. Bargheer: udkm1Dsim - A simulation toolkit for 1D ultrafast dynamics in condensed matter. *Computer Physics Communications* **185**, 651 (2014).

[28] M. Battiato, K. Carva, and P. M. Oppeneer: Superdiffusive Spin Transport as a Mechanism of Ultrafast Demagnetization. *Physical Review Letters* **105**, 027203 (2010).

[29] M. Battiato, K. Carva, and P. M. Oppeneer: Theory of laser-induced ultrafast superdiffusive spin transport in layered heterostructures. *Physical Review B* **86**, 024404 (2012).

[30] D. Gibbs, D. Harshman, E. Isaacs, D. McWhan, D. Mills, and C. Vettier: Polarization and Resonance Properties of Magnetic-X-Ray Scattering in Holmium. *Physical Review Letters* **61**, 1241 (1988).

[31] J. P. Hannon, G. T. Trammell, M. Blume, and D. Gibbs: X-Ray Resonance Exchange Scattering. *Physical Review Letters* **61**, 1245 (1988).

[32] C. Vettier: Neutrons and X-Rays - 2 Probes for Magnetism. *Physica B - Condensed Matter* **192**, 1 (1993).

[33] Z. Qiu and S. Bader: Surface magneto-optic Kerr effect. *Review of Scientific Instruments* **71**, 1243 (2000).

[34] J. Stöhr and H. C. Siegmann: *Magnetism: From Fundamentals to Nanoscale Dynamics*, vol. 152 of *Springer Series in Solid-State Physics*. Berlin: Springer (2006).

[35] W. L. Bragg: The Diffraction of Short Electromagnetic Waves by a Crystal. *Proceedings of the Cambridge Philosophical Society* **17**, 43 (1913).

[36] B. Warren: *X-Ray Diffraction*. Addison-Wesley (1969).

[37] J. Cowley: *Diffraction Physics*. Elsevier (1995).

[38] J. Als-Nielsen and D. McMorrow: *Elements of Modern X Ray Physics*. Wiley, New York (2000/2001).

[39] M. Gell-Mann and M. L. Goldberger: Scattering of Low-Energy Photons by Particles of Spin ½. *Physical Review* **96**, 1433 (1954).

[40] P. M. Platzman and N. Tzoar: Magnetic Scattering of X Rays from Electrons in Molecules and Solids. *Physical Review B* **2**, 3556 (1970).

[41] S. W. Lovesey and S. P. Collins: *X-Ray Scattering and Absorption by Magnetic Materials*. Oxford University Press (1996).

[42] M. Blume and D. Gibbs: Polarization Dependence of Magnetic X-ray Scattering. *Physical Review B* **37**, 1779 (1988).

[43] M. Blume: Magnetic Scattering of X-rays (invited). *Journal of Applied Physics* **57**, 3615 (1985).

[44] H. Ott, C. Schüßler-Langeheine, E. Schierle, A. Y. Grigoriev, V. Leiner, H. Zabel, G. Kaindl, and E. Weschke: Magnetic x-ray scattering at the M-5 absorption edge of Ho. *Physical Review B* **74**, 094412 (2006).

[45] J. Schlappa, C. F. Chang, Z. Hu, E. Schierle, H. Ott, E. Weschke, G. Kaindl, M. Huijben, G. Rijnders, D. H. A. Blank, L. H. Tjeng, and C. Schüßler-Langeheine: Resonant soft x-ray scattering from stepped surfaces of $SrTiO_3$. *Journal of Physics - Condensed Matter* **24**, 035501 (2012).

[46] E. Benckiser, M. W. Haverkort, S. Brück, E. Göring, S. Macke, A. Frano, X. Yang, O. K. Andersen, G. Cristiani, H.-U. Habermeier, A. V. Boris, I. Zegkinoglou, P. Wochner, H.-J. Kim, V. Hinkov, and B. Keimer: Orbital reflectometry of oxide heterostructures. *Nature Materials* **10**, 189 (2011).

[47] J. D. Jackson: *Klassische Elektrodynamik*. Berlin, New York: De Gruyter (2002).

[48] A. Beer: Bestimmung der Absorption des roten Lichts in farbigen Flüssigkeiten. *Annalen der Physik* **162**, 77 (1852).

[49] B. Henke, E. Gullikson, and J. Davis: X-Ray Interactions - Photoabsorption, Scattering Transmission, and Reflection at E=50-30,000 eV, Z=1-92. *Atomic Data and Nuclear Data Tables* **54**, 181 (1993).

[50] J. P. Pétrakian: New investigation of the optical absorption of rare-earth thin films. *Thin Solid Films* **13**, 269 (1972).

[51] G. Güntherodt, P. Wachter, and D. Imboden: Energy Level Scheme and Effect of Magnetic Order on Optical Transitions in Europium Chalcogenides. *Physik der kondensierten Materie* **12**, 292 (1971).

[52] N. Singh, S. M. Saini, T. Nautiyal, and S. Auluck: Theoretical investigation of the optical and magneto-optical properties of EuX (X = S, Se, and Te). *Physica B - Condensed Matter* **388**, 99 (2007).

[53] Springer: Landolt-Börnstein database. http://www.springermaterials.com (26/04/2011).

[54] S. Kohn, P. Yu, Y. Petroff, Y. Shen, Y. Tsang, and M. Cohen: Electronic Band-Structure and Optical Properties of PbTe, PbSe, and PbS. *Physical Review B* **8**, 1477 (1973).

[55] G. Martinez, M. Schluter, and M. Cohen: Electronic-structure of PbSe and PbTe .2. Optical-Properties. *Physical Review B* **11**, 660 (1975).

[56] W. Y. Ching, F. Gan, and M.-Z. Huang: Band theory of linear and nonlinear susceptibilities of some binary ionic insulators. *Physical Review B* **52**, 1596 (1995).

[57] M. Beye, S. Schreck, F. Sorgenfrei, C. Trabant, N. Pontius, C. Schüßler-Langeheine, W. Wurth, and A. Föhlisch: Stimulated X-ray emission for materials science. *Nature* **501**, 191+ (2013).

[58] M. Ferray, A. Lhuillier, X. Li, L. Lompre, G. Mainfray, and C. Manus: Multiple-harmonic Conversion of 1064-nm Radiation in Rare-Gases. *Journal of Physics - Atomic Molecular and Optical Physics* **21**, L31 (1988).

[59] X. Li, A. Lhuillier, M. Ferray, L. Lompre, and G. Mainfray: Multiple-Harmonic Generation in Rare-Gases at High Laser Intensity. *Physical Review A* **39**, 5751 (1989).

[60] F. Krausz and M. Ivanov: Attosecond physics. *Reviews of Modern Physics* **81**, 163 (2009).

[61] M. M. Murnane, H. C. Kapteyn, and R. W. Falcone: High-Density Plasmas Produced by Ultrafast Laser Pulses. *Physical Review Letters* **62**, 155 (1989).

[62] F. Zamponi, Z. Ansari, C. V. K. Schmising, P. Rothhardt, N. Zhavoronkov, M. Wörner, T. Elsässer, M. Bargheer, T. Trobitzsch-Ryll, and M. Haschke: Femtosecond hard X-ray plasma sources with a kilohertz repetition rate. *Applied Physics A - Materials Science & Processing* **96**, 51 (2009).

[63] N. Zhavoronkov, Y. Gritsai, M. Bargheer, M. Wörner, and T. Elsässer: Generation of ultrashort K-alpha radiation from quasipoint interaction area of femtosecond pulses with thin foils. *Applied Physics Letters* **86**, 244107 (2005).

[64] R. Schoenlein, S. Chattopadhyay, H. Chong, T. Glover, P. Heimann, C. Shank, A. Zholents, and M. Zolotorev: Generation of femtosecond pulses of synchrotron radiation. *Science* **287**, 2237 (2000).

[65] A. A. Zholents and M. S. Zolotorev: Femtosecond X-Ray Pulses of Synchrotron Radiation. *Physical Review Letters* **76**, 912 (1996).

[66] K. Holldack, T. Kachel, S. Khan, R. Mitzner, and T. Quast: Characterization of laser-electron interaction at the BESSY II femtoslicing source. *Physical Review Special Topics - Accelerators and Beams* **8**, 040704 (2005).

[67] K. Holldack, S. Khan, R. Mitzner, and T. Quast: Femtosecond terahertz radiation from femtoslicing at BESSY. *Physical Review Letters* **96**, 054801 (2006).

[68] S. Khan, K. Holldack, T. Kachel, R. Mitzner, and T. Quast: Femtosecond undulator radiation from sliced electron bunches. *Physical Review Letters* **97**, 074801 (2006).

[69] P. Beaud, S. L. Johnson, A. Streun, R. Abela, D. Abramsohn, D. Grolimund, F. Krasniqi, T. Schmidt, V. Schlott, and G. Ingold: Spatiotemporal Stability of a Femtosecond Hard X-Ray Undulator Source Studied by Control of Coherent Optical Phonons. *Physical Review Letters* **99**, 174801 (2007).

[70] W. Ackermann, G. Asova, V. Ayvazyan, A. Azima, N. Baboi, J. Baehr, V. Balandin, B. Beutner, A. Brandt, A. Bolzmann, R. Brinkmann, O. I. Brovko, M. Castellano, P. Castro, L. Catani, E. Chiadroni, S. Choroba, A. Cianchi, J. T. Costello, D. Cubaynes, J. Dardis, W. Decking, H. Delsim-Hashemi, A. Delserieys, G. Di Pirro, M. Dohlus, S. Düsterer, A. Eckhardt, H. T. Edwards, B. Faatz, J. Feldhaus, K. Flöttmann, J. Frisch, L. Fröhlich, T. Garvey, U. Gensch, C. Gerth, M. Görler, N. Golubeva, H.-J. Grabosch, M. Grecki, O. Grimm, K. Hacker, U. Hahn, J. H. Han, K. Honkavaara, T. Hott, M. Huening, Y. Ivanisenko, E. Jaeschke, W. Jalmuzna, T. Jezynski, R. Kammering, V. Katalev, K. Kavanagh, E. T. Kennedy, S. Khodyachykh, K. Klose, V. Kocharyan, M. Körfer, M. Kollewe, W. Koprek, S. Korepanov, D. Kostin, M. Krassilnikov, G. Kube, M. Kuhlmann, C. L. S. Lewis, L. Lilje, T. Limberg, D. Lipka, F. Löhl, H. Luna, M. Luong, M. Martins, M. Meyer, P. Michelato, V. Miltchev, W. D. Möller, L. Monaco, W. F. O. Müller, A. Napieralski, O. Napoly, P. Nicolosi, D. Noelle, T. Nunez, A. Oppelt, C. Pagani, R. Paparella, N. Pchalek, J. Pedregosa-Gutierrez, B. Petersen, B. Petrosyan, G. Petrosyan, L. Petrosyan, J. Pflueger, E. Ploenjes, L. Poletto, K. Pozniak, E. Prat, D. Proch, P. Pucyk, P. Radcliffe, H. Redlin, K. Rehlich, M. Richter, M. Roehrs, J. Roensch, R. Romaniuk, M. Ross, J. Rossbach, V. Rybnikov, M. Sachwitz, E. L. Saldin, W. Sandner, H. Schlarb, B. Schmidt, M. Schmitz, P. Schmüser, J. R. Schneider, E. A. Schneidmiller,

S. Schnepp, S. Schreiber, M. Seidel, D. Sertore, A. V. Shabunov, C. Simon, S. Simrock, E. Sombrowski, A. A. Sorokin, P. Spanknebel, R. Spesyvtsev, L. Staykov, B. Steffen, F. Stephan, F. Stulle, H. Thom, K. Tiedtke, M. Tischer, S. Toleikis, R. Treusch, D. Trines, I. Tsakov, E. Vogel, T. Weiland, H. Weise, M. Wellhöffer, M. Wendt, I. Will, A. Winter, K. Wittenburg, W. Wurth, P. Yeates, M. V. Yurkov, I. Zagorodnov, and K. Zapfe: Operation of a free-electron laser from the extreme ultraviolet to the water window. *Nature Photonics* **1**, 336 (2007).

[71] Y. Ding, A. Brachmann, F. J. Decker, D. Dowell, P. Emma, J. Frisch, S. Gilevich, G. Hays, P. Hering, Z. Huang, R. Iverson, H. Loos, A. Miahnahri, H. D. Nuhn, D. Ratner, J. Turner, J. Welch, W. White, and J. Wu: Measurements and Simulations of Ultralow Emittance and Ultrashort Electron Beams in the Linac Coherent Light Source. *Physical Review Letters* **102**, 254801 (2009).

[72] T. Shintake, H. Tanaka, T. Hara, T. Tanaka, K. Togawa, M. Yabashi, Y. Otake, Y. Asano, T. Fukui, T. Hasegawa, A. Higashiya, N. Hosoda, T. Inagaki, S. Inoue, Y. Kim, M. Kitamura, N. Kumagai, H. Maesaka, S. Matsui, M. Nagasono, T. Ohshima, T. Sakurai, K. Tamasaku, Y. Tanaka, T. Tanikawa, T. Togashi, S. Wu, H. Kitamura, T. Ishikawa, T. Asaka, T. Bizen, S. Goto, T. Hirono, M. Ishii, H. Kimura, T. Kobayashi, T. Masuda, T. Matsushita, X. Marechal, H. Ohashi, T. Ohata, K. Shirasawa, T. Takagi, S. Takahashi, M. Takeuchi, R. Tanaka, A. Yamashita, K. Yanagida, and C. Zhang: Stable Operation of a Self-Amplified Spontaneous-Emission Free-Electron Laser in the Extremely Ultraviolet Region. *Physical Review Special Topics - Accelerators and Beams* **12**, 070701 (2009).

[73] D. Attwood: *Soft X-rays and extreme ultraviolet radiation.* Cambridge University Press (1999).

[74] K. Wille: Synchrotron Radiation Sources. *Reports on Progress in Physics* **54**, 1005 (1991).

[75] H. Wiedmann: *Synchrotron Radiation.* Springer (2003).

[76] Helmholtz-Zentrum Berlin.

[77] E. Saldin, E. Schneidmiller, and M. Yurkov: The Physics of Free-Electron Lasers - An Introduction. *Physics Reports - Review Section of Physics Letters* **260**, 187 (1995).

[78] R. Bonifacio, C. Pellegrini, and L. M. Narducci: Collective Instabilities and High-Gain Regime in a Free-Electron Laser. *Optics Communications* **50**, 373 (1984).

[79] V. Ayvazyan, N. Baboi, I. Bohnet, R. Brinkmann, M. Castellano, P. Castro, L. Catani, S. Choroba, A. Cianchi, M. Dohlus, H. Edwards, B. Faatz, A. Fateev, J. Feldhaus, K. Flöttmann, A. Gamp, T. Garvey, H. Genz, C. Gerth, V. Gretchko, B. Grigoryan, U. Hahn, C. Hessler, K. Honkavaara, M. Hüning, R. Ischebeck, M. Jablonka, T. Kamps, M. Körfer, M. Krassilnikov, J. Krzywinski, M. Liepe, A. Liero, T. Limberg, H. Loos, M. Luong, C. Magne, J. Menzel, P. Michelato, M. Minty, U.-C. Müller, D. Noelle, A. Novokhatski, C. Pagani, F. Peters, J. Pflüger, P. Piot, L. Plucinski, K. Rehlich, I. Reyzl, A. Richter, J. Rossbach, E. Saldin, W. Sandner, H. Schlarb, G. Schmidt, P. Schmüser, J. Schneider, E. Schneidmiller, H.-J. Schreiber, S. Schreiber, D. Sertore, S. Setzer, S. Simrock, R. Sobierajski, B. Sonntag, B. Steeg, F. Stephan, K. Sytchev, K. Tiedtke, M. Tonutti, R. Treusch, D. Trines, D. Tuerke, V. Verzilov, R. Wanzenberg, T. Weiland, H. Weise, M. Wendt, T. Wilhein, I. Will, K. Wittenburg, S. Wolff, M. Yurkov, and K. Zapfe: A new powerful source for coherent VUV radiation: Demonstration of exponential growth and saturation at the TTF free-electron laser. *The European Physical Journal D - Atomic, Molecular, Optical and Plasma Physics* **20**, 149 (2002).

[80] I. Robinson, G. Grübel, and S. Mochrie: X-ray beams with high coherence. *New Journal of Physics* **12**, 035002 (2010).

[81] J. Feldhaus, J. Arthur, and J. Hastings: X-ray free-electron lasers. *Journal of Physics B - Atomic Molecular and Optical Physics* **38**, S799 (2005).

[82] W. F. Schlotter, F. Sorgenfrei, T. Beeck, M. Beye, S. Gieschen, H. Meyer, M. Nagasono, A. Föhlisch, and W. Wurth: Longitudinal coherence measurements of an extreme-ultraviolet free-electron laser. *Optics Letters* **35**, 372 (2010).

[83] M. Beye, O. Krupin, G. Hays, A. H. Reid, D. Rupp, S. de Jong, S. Lee, W. S. Lee, Y. D. Chuang, R. Coffee, J. P. Cryan, J. M. Glownia, A. Föhlisch, M. R. Holmes, A. R. Fry, W. E. White, C. Bostedt, A. O. Scherz, H. A. Dürr, and W. F. Schlotter: X-ray pulse preserving single-shot optical cross-correlation method for improved experimental temporal resolution. *Applied Physics Letters* **100**, 121108 (2012).

[84] O. Krupin, M. Trigo, W. F. Schlotter, M. Beye, F. Sorgenfrei, J. J. Turner, D. A. Reis, N. Gerken, S. Lee, W. S. Lee, G. Hays, Y. Acremann, B. Abbey, R. Coffee, M. Messerschmidt, S. P. Hau-Riege, G. Lapertot, J. Lüning, P. Heimann, R. Soufli, M. Fernandez-Perea, M. Rowen, M. Holmes, S. L. Molodtsov, A. Föhlisch, and W. Wurth: Temporal cross-correlation of x-ray free electron and optical lasers using soft x-ray pulse induced transient reflectivity. *Optics Express* **20**, 11396 (2012).

[85] Certified-Scientific-Software: `www.certif.com`.

[86] D. Doering, Y. D. Chuang, N. Andresen, K. Chow, D. Contarato, C. Cummings, E. Domning, J. Joseph, J. S. Pepper, B. Smith, G. Zizka, C. Ford, W. S. Lee, M. Weaver, L. Patthey, J. Weizeorick, Z. Hussain, and P. Denes: Development of a compact fast CCD camera and resonant soft x-ray scattering endstation for time-resolved pump-probe experiments. *Review of Scientific Instruments* **82**, 073303 (2011).

[87] N. Pontius, T. Kachel, C. Schüßler-Langeheine, W. F. Schlotter, M. Beye, F. Sorgenfrei, C. F. Chang, A. Föhlisch, W. Wurth, P. Metcalf, I. Leonov, A. Yaresko, N. Stojanovic, M. Berglund, N. Guerassimova, S. Düsterer, H. Redlin, and H. A. Dürr: Time-resolved resonant soft x-ray diffraction with free-electron lasers: Femtosecond dynamics across the Verwey transition in magnetite. *Applied Physics Letters* **98**, 182504 (2011).

[88] N. Pontius: FEMTOSPEX-Scattering station. `http://www.helmholtz-berlin.de/pubbin/igama_output?modus=einzel&sprache=en&gid=1886&typoid=42414` (14/02/2013).

[89] R. Könnecke, R. Follath, N. Pontius, J. Schlappa, F. Eggenstein, T. Zeschke, P. Bischoff, J. S. Schmidt, T. Noll, C. Trabant, S. Schreck, P. Wernet, S. Eisebitt, F. Senf, C. Schüßler-Langeheine, A. Erko, and A. Föhlisch: The confocal plane grating spectrometer at BESSY II. *Journal of Electron Spectroscopy and Related Phenomena* **188**, 133 (2013).

[90] C. Gahl, A. Azima, M. Beye, M. Deppe, K. Döbrich, U. Hasslinger, F. Hennies, A. Melnikov, M. Nagasono, A. Pietzsch, M. Wolf, W. Wurth, and A. F"ohlisch: A femtosecond X-ray/optical cross-correlator. *Nature Photonics* **2**, 165 (2008).

[91] E. J. W. Verwey: Electronic Conduction of Magnetite (Fe_3O_4) and its Transition Point at Low Temperatures. *Nature* **144**, 327 (1939).

[92] F. Walz: The Verwey transition - a topical review. *Journal of Physics-Condensed Matter* **14**, R285 (2002).

[93] E. Nazarenko, J. E. Lorenzo, Y. Joly, J. L. Hodeau, D. Mannix, and C. Marin: Resonant X-Ray Diffraction Studies on the Charge Ordering in Magnetite. *Physical Review Letters* **97**, 056403 (2006).

[94] J. E. Lorenzo, C. Mazzoli, N. Jaouen, C. Detlefs, D. Mannix, S. Grenier, Y. Joly, and C. Marin: Charge and Orbital Correlations at and above the Verwey Phase Transition in Magnetite. *Physical Review Letters* **101**, 226401 (2008).

[95] J. Garcia, G. Subias, J. Herrero-Martin, J. Blasco, V. Cuartero, M. C. Sanchez, C. Mazzoli, and F. Yakhou: Reexamination of the Temperature Dependences

of Resonant Reflections in Highly Stoichiometric Magnetite. *Physical Review Letters* **102**, 176405 (2009).

[96] P. Piekarz, K. Parlinski, and A. M. Oleś: Origin of the Verwey transition in magnetite: Group theory, electronic structure, and lattice dynamics study. *Physical Review B* **76**, 165124 (2007).

[97] H. Uzu and A. Tanaka: Complex-orbital order in Fe_3O_4 and mechanism of the Verwey transition. *Journal of the Physical Society of Japan* **77**, 074711 (2008).

[98] J. Garcia and G. Subias: The Verwey transition - a new perspective. *Journal of Physics-Condensed Matter* **16**, R145 (2004).

[99] S.-C. Weng, Y.-R. Lee, C.-G. Chen, C.-H. Chu, Y.-L. Soo, and S.-L. Chang: Direct Observation of Charge Ordering in Magnetite Using Resonant Multiwave X-Ray Diffraction. *Physical Review Letters* **108**, 146404 (2012).

[100] M. S. Senn, J. P. Wright, and J. P. Attfield: Charge order and three-site distortions in the Verwey structure of magnetite. *Nature* **481**, 173 (2012).

[101] M. S. Senn, I. Loa, J. P. Wright, and J. P. Attfield: Electronic orders in the Verwey structure of magnetite. *Physical Review B* **85**, 125119 (2012).

[102] J. Schlappa, C. Schüßler-Langeheine, C. F. Chang, H. Ott, A. Tanaka, Z. Hu, M. W. Haverkort, E. Schierle, E. Weschke, G. Kaindl, and L. H. Tjeng: Direct observation of t_{2g} orbital ordering in magnetite. *Physical Review Letters* **100**, 026406 (2008).

[103] I. Leonov, A. Yaresko, V. Antonov, M. Korotin, and V. Anisimov: Charge and Orbital Order in Fe_3O_4. *Physical Review Letters* **93**, 146404 (2004).

[104] A. Tanaka, C. F. Chang, M. Buchholz, C. Trabant, E. Schierle, J. Schlappa, D. Schmitz, H. Ott, P. Metcalf, L. H. Tjeng, and C. Schüßler-Langeheine: Symmetry of Orbital Order in Fe_3O_4 Studied by Fe L_2,L_3 Resonant X-Ray Diffraction. *Physical Review Letters* **108**, 227203 (2012).

[105] A. Tanaka, C. F. Chang, M. Buchholz, C. Trabant, E. Schierle, J. Schlappa, D. Schmitz, H. Ott, P. Metcalf, L. H. Tjeng, and C. Schüßler-Langeheine: Symmetry of Orbital Order in Fe_3O_4 Studied by Fe L_2,L_3 Resonant X-Ray Diffraction (vol 108, 227203, 2012). *Physical Review Letters* **109**, 119901 (2012).

[106] S. K. Park, T. Ishikawa, and Y. Tokura: Charge-gap formation upon the Verwey transition in Fe_3O_4. *Physical Review B* **58**, 3717 (1998).

[107] F. Novelli, D. Fausti, J. Reul, F. Cilento, P. H. M. van Loosdrecht, A. A. Nugroho, T. T. M. Palstra, M. Grüninger, and F. Parmigiani: Ultrafast optical spectroscopy of the lowest energy excitations in the Mott insulator compound YVO_3: Evidence for Hubbard-type excitons. *Physical Review B* **86**, 165135 (2012).

[108] Z. Yang, C. Ko, and S. Ramanathan: Oxide Electronics Utilizing Ultrafast Metal-Insulator Transitions. *Annual Review of Materials Research* **41**, 337 (2011).

[109] F. Weber, N. Aliouane, H. Zheng, J. F. Mitchell, D. N. Argyriou, and D. Reznik: Signature of checkerboard fluctuations in the phonon spectra of a possible polaronic metal $La_{1.2}Sr_{1.8}Mn_2O_7$. *Nature Materials* **8**, 798 (2009).

[110] M. Imada, A. Fujimori, and Y. Tokura: Metal-Insulator Transitions. *Review of Modern Physics* **70**, 1039 (1998).

[111] M. Uehara, S. Mori, C. Chen, and S. Cheong: Percolative phase separation underlies colossal magnetoresistance in mixed-valent manganites. *Nature* **399**, 560 (1999).

[112] K. Lai, M. Nakamura, W. Kundhikanjana, M. Kawasaki, Y. Tokura, M. A. Kelly, and Z.-X. Shen: Mesoscopic Percolating Resistance Network in a Strained Manganite Thin Film. *Science* **329**, 190 (2010).

[113] F. Massee, S. de Jong, Y. Huang, W. K. Siu, I. Santoso, A. Mans, A. T. Boothroyd, D. Prabhakaran, R. Follath, A. Varykhalov, L. Patthey, M. Shi, J. B. Goedkoop, and M. S. Golden: Bilayer manganites reveal polarons in the midst of a metallic breakdown. *Nature Physics* **7**, 978 (2011).

[114] C. J. Chang and R. A. Brown: Radial segregation induced by natural convection and melt/solid interface shape in vertical bridgman growth. *Journal of Crystal Growth* **63**, 343 (1983).

[115] R. Aragón, P. M. Gehring, and S. M. Shapiro: Stoichiometry, percolation, and Verwey ordering in magnetite. *Physical Review Letters* **70**, 1635 (1993).

[116] C. F. Chang, J. Schlappa, M. Buchholz, A. Tanaka, E. Schierle, D. Schmitz, H. Ott, R. Sutarto, T. Willers, P. Metcalf, L. H. Tjeng, and C. Schüßler-Langeheine: Intrinsic and Extrinsic X-ray Absorption Effects in Soft X-ray Diffraction from the Superstructure in Magnetite. *Physical Review B* **83**, 073105 (2011).

[117] D. J. Huang, H.-J. Lin, J. Okamoto, K. S. Chao, H.-T. Jeng, G. Y. Guo, C.-H. Hsu, C.-M. Huang, D. C. Ling, W. B. Wu, C. S. Yang, and C. T. Chen: Charge-Orbital Ordering and Verwey Transition in Magnetite Measured by Resonant Soft X-Ray Scattering. *Physical Review Letters* **96**, 096401 (2006).

[118] P. Heimann, O. Krupin, W. F. Schlotter, J. Turner, J. Krzywinski, F. Sorgenfrei, M. Messerschmidt, D. Bernstein, J. Chalupsky, V. Hajkova, S. Hau-Riege, M. Holmes, L. Juha, N. Kelez, J. Lüning, D. Nordlund, M. Fernandez Perea, A. Scherz, R. Soufli, W. Wurth, and M. Rowen: Linac Coherent Light Source soft x-ray materials Science instrument optical design and monochromator commissioning. *Review of Scientific Instruments* **82**, 093104 (2011).

[119] E. F. J. Westrum and F. Grønvold: Magnetite (Fe_3O_4) Heat Capacity and Thermodynamic Properties from 5 to 350 K, Low-Temperature Transition. *The Journal of Chemical Thermodynamics* **1**, 543 (1969).

[120] U. Buchenau and I. Muller: Optical Properties of Magnetite. *Solid State Communications* **11**, 1291 (1972).

[121] A. Schlegel, S. Alvarado, and P. Wachter: Optical-Properties of Magnetite (FE3O4). *Journal of Physics C-Solid State Physics* **12**, 1157 (1979).

[122] M. A. Hossain, I. Zegkinoglou, Y. D. Chuang, J. Geck, B. Bohnenbuck, A. G. C. Gonzalez, H. H. Wu, C. Schüßler-Langeheine, D. G. Hawthorn, J. D. Denlinger, R. Mathieu, Y. Tokura, S. Satow, H. Takagi, Y. Yoshida, Z. Hussain, B. Keimer, G. A. Sawatzky, and A. Damascelli: Electronic Superlattice Revealed by Resonant Scattering from Random Impurities in $Sr_3Ru_2O_7$. *Scientific Reports* **3**, 2299 (2013).

[123] F. Cilento, C. Giannetti, G. Ferrini, S. Dal Conte, T. Sala, G. Coslovich, M. Rini, A. Cavalleri, and F. Parmigiani: Ultrafast insulator-to-metal phase transition as a switch to measure the spectrogram of a supercontinuum light pulse. *Applied Physics Letters* **96**, 021102 (2010).

[124] E. J. Samuelsen and O. Steinsvoll: Low-Energy Phonons in Magnetite. *Physica Status Solidi (b)* **61**, 615 (1974).

[125] S. M. Shapiro, M. Iizumi, and G. Shirane: Neutron scattering study of the diffuse critical scattering associated with the Verwey transition in magnetite (Fe_3O_4). *Physical Review B* **14**, 200 (1976).

[126] Y. Wu, Y.-M. Lin, A. A. Bol, K. A. Jenkins, F. Xia, D. B. Farmer, Y. Zhu, and P. Avouris: High-Frequency, scaled Graphene Transistors on Diamond-like Carbon. *Nature* **472**, 74 (2011).

[127] T. Roth, A. J. Schellekens, S. Alebrand, O. Schmitt, D. Steil, B. Koopmans, M. Cinchetti, and M. Aeschlimann: Temperature Dependence of Laser-Induced Demagnetization in Ni: A Key for Identifying the Underlying Mechanism. *Physical Review X* **2**, 021006 (2012).

[128] A. J. Schellekens and B. Koopmans: Microscopic model for ultrafast magnetization dynamics of multisublattice magnets. *Physical Review B* **87**, 020407 (2013).

[129] S. Essert and H. C. Schneider: Electron-phonon scattering dynamics in ferromagnetic metals and their influence on ultrafast demagnetization processes. *Physical Review B* **84**, 224405 (2011).

[130] M. A. Ruderman and C. Kittel: Indirect Exchange Coupling of Nuclear Magnetic Moments by Conduction Electrons. *Physical Review* **96**, 99 (1954).

[131] T. Kasuya: A Theory of Metallic Ferro- and Antiferromagnetism on Zener's Model. *Progress of Theoretical Physics* **16**, 45 (1956).

[132] K. Yosida: Magnetic Properties of Cu-Mn Alloys. *Physical Review* **106**, 893 (1957).

[133] W. C. Koehler, J. W. Cable, M. K. Wilkinson, and E. O. Wollan: Magnetic Structures of Holmium. I. The Virgin State. *Physical Review* **151**, 414 (1966).

[134] K. Holldack, N. Pontius, E. Schierle, T. Kachel, V. Soltwisch, R. Mitzner, T. Quast, G. Springholz, and E. Weschke: Ultrafast dynamics of antiferromagnetic order studied by femtosecond resonant soft x-ray diffraction. *Applied Physics Letters* **97**, 062502 (2010).

[135] P. Gaal, D. Schick, M. Herzog, A. Bojahr, R. Shayduk, J. Goldshteyn, H. A. Navirian, W. Leitenberger, I. Vrejoiu, D. Khakhulin, M. Wulff, and M. Bargheer: Time-domain sampling of x-ray pulses using an ultrafast sample response. *Applied Physics Letters* **101**, 243106 (2012).

[136] A. Einstein and W. J. de Haas: Experimenteller Nachweis der Ampereschen Molekularströme. *Verhandlungen der deutschen physikalischen Gesellschaft* **17**, 152 (1915).

[137] G. Springholz and G. Bauer: Strain Relaxation by Coherent 3-Dimensional Islanding in Molecular-Beam Epitaxy of EuTe on PbTe(111). *Physical Review B* **48**, 10998 (1993).

[138] E. Schierle: Antiferromagnetism in Thin Films Studied by Resonant Magnetic Soft X-Ray Scattering. Ph.D. thesis, FU Berlin (2007).

[139] U. Köbler, I. Apfelstedt, K. Fischer, W. Zinn, E. Scheer, J. Wosnitza, T. Brückel, and H. VonLöhneysen: Biquadratic exchange and critical-bavahior in the diluted antiferromagnet $\mathrm{Eu}_x\mathrm{Sr}_{1-x}\mathrm{Te}$. *Zeitschrift fur Physik B-Condensed Matter* **92**, 475 (1993).

[140] P. Wachter: Europium Chalcogenides. In *Handbook on the Physics and Chemistry of Rare Earths (edited by K. A. Gschneidner, Jr. and L. Eyring), vol. 2.*. North-Holland Publishing Company (1979).

[141] D. Rodbell, L. Osika, and P. Lawrence: Low-temperature lattice distortions in MnO and EuTe. *Journal of Applied Physics* **36**, 666 (1965).

[142] G. Busch, G. Güntherodt, and P. Wachter: Optical Transitions and the Energy Level Scheme of the Europium Chalcogenides. *Journal de Physique* **32 (C1)**, C1 928 (1971).

[143] J. Burnett, R. Gupta, and U. Griesmann: Absolute refractive indices and thermal coefficients of CaF_2, SrF_2, BaF_2, and LiF near 157 nm. *Applied Optics* **41**, 2508 (2002).

[144] W. Heiss, R. Kirchschlager, G. Springholz, Z. Chen, M. Debnath, and Y. Oka: Magnetic polaron induced near-band-gap luminescence in epitaxial EuTe. *Physical Review B* **70**, 035209 (2004).

[145] Y. Shapira and T. Reed: EuTe .3. Ultrasonic behavior. *Physical Review B - Solid State* **5**, 2657 (1972).

[146] Z. Tian, J. Garg, K. Esfarjani, T. Shiga, J. Shiomi, and G. Chen: Phonon conduction in PbSe, PbTe, and $\mathrm{PbTe}_{1-x}\mathrm{Se}_x$ from first-principles calculations. *Physical Review B* **85**, 184303 (2012).

[147] R. Zeyher and W. Kress: Spin-disorder-induced Raman scattering from phonons in europium chalcogenides. II. Theory. *Physical Review B* **20**, 2850 (1979).

[148] H. Kim and M. Kaviany: Effect of thermal disorder on high figure of merit in PbTe. *Physical Review B* **86**, 045213 (2012).

[149] C. E. Ekuma, D. J. Singh, J. Moreno, and M. Jarrell: Optical properties of PbTe and PbSe. *Physical Review B* **85**, 085205 (2012).

[150] J. Blinowski and P. Kacman: Interlayer exchange coupling mediated by valence-band electrons. *Physical Review B* **64**, 045302 (2001).

[151] S. M. Jaya and W. Nolting: Quasiparticle bandstructure of antiferromagnetic EuTe. *Journal of Physics: Condensed Matter* **9**, 10439 (1997).

[152] S. Q. Shi, C. Y. Ouyang, Q. Fang, J. Q. Shen, W. H. Tang, and C. R. Li: Electronic structure and magnetism of EuX (X = O, S, Se and Te): A first-principles investigation. *Europhysics Letters* **83**, 69001 (2008).

[153] D. Khokhlov: *Lead Chalcogenides: Physics and Applications.* CRC Press (2002).

[154] A. M. Mulders, S. M. Lawrence, A. J. Princep, U. Staub, Y. Bodenthin, M. Garcia-Fernandez, M. Garganourakis, J. Hester, R. Macquart, and C. D. Ling: Circularly polarized soft x-ray diffraction study of helical magnetism in hexaferrite. *Physical Review B* **81**, 092405 (2010).

[155] M. Buchholz: Local Symmetry and Domain Patterns: Ordering Phenomena in Transition-Metal Oxides . Ph.D. thesis, University of Cologne (2013).

[156] HASYLAB: The Data Acquisition and Control Systems. `http://photon-science.desy.de/facilities/flash/facility_information/daq_and_control_systems/index_eng.html` (22/01/2014).